Measuring Atomic Properties with an Atom Interferometer

by

Tony David Roberts

Submitted to the Department of Physics
in partial fulfillment of the requirements for the degree of

Doctor of Philosophy

at the

MASSACHUSETTS INSTITUTE OF TECHNOLOGY

September 2002

Author .....
Department of Physics
June 10, 2002

Certified by .....
David E. Pritchard
Professor of Physics
Thesis Supervisor

Accepted by .....
Thomas J. Greytak
Professor, Associate Department Head for Education

Measuring Atomic Properties with an Atom Interferometer

by

Tony David Roberts

Submitted to the Department of Physics
on June 10, 2002, in partial fulfillment of the
requirements for the degree of
Doctor of Philosophy

Abstract

Two experiments are presented which measure atomic properties using an atom interferometer. The interferometer splits the sodium de Broglie wave into two paths, one of which travels through an interaction region. The paths are recombined, and the interference pattern exhibits a phase shift depending on the strength of the interaction.

In the first experiment, the interaction involves a gas. De Broglie waves traveling through the gas experience a phase shift represented by an index of refraction. By measuring the index of refraction at various wavelengths, the predicted phenomenon of glory oscillations in the phase shift has been observed for the first time. The index of refraction has been measured for sodium atoms in gases of argon, krypton, xenon, and nitrogen over a wide range of wavelength. These measurements offer detailed insight into the interatomic potential between sodium atoms and the gases. Theoretical predictions of the interatomic potentials are challenged by these results, which should encourage a renewed effort to better understand these potentials.

The second experiment measures atomic polarizability with an atom interferometer. Here, the interaction is with an electric field; the atom experiences a phase shift proportional to its energy inside the field. Previously, this method was used to perform the most accurate ($< 1\%$) measurement of sodium polarizability. The precision was limited, however, by the spread of velocities in the atomic beam—the phase shift is different depending on velocity, and the interference pattern is washed out. This thesis presents a new technique to "rephase" the interference pattern at large applied fields, and demonstrates a measurement that is free of this limitation. In addition, most of the systematic errors that plagued the previous polarizability measurement are eliminated by the new technique, and an order of magnitude improvement in precision now appears quite feasible. The remaining systematic errors can be eliminated by measuring the ratio of polarizabilities between two different atoms, a comparison whose precision is better by another order of magnitude.

Thesis Supervisor: David E. Pritchard
Title: Professor of Physics

To

Karen

Motion being eternal, the first mover will be eternal also.

— Aristotle, *Physics*

Contents

Chapter 1

Theory and Operation of an Atom Interferometer

1.1 Introduction

The design, construction, and operation of the MIT atom interferometer, as well as incremental improvements, have been described in detail in many sources over the past decade, most notably in the dissertations of past doctoral students [53, 33, 18, 47, 88, 80, 56] as well as other publications [54, 8]. The most recent innovations are outlined in [56] and [57].

We will briefly recap the layout of the interferometer, including a record of its current operating parameters and capabilities. These specifics may be important in relation to the experiments discussed in later chapters.

The subsequent part of this chapter will address the most important consideration for successful operation of the interferometer—prevention of the many processes that can degrade the interference pattern. It will begin with an analysis of alignment requirements for a three-grating interferometer, and continue with a look at external influences that can introduce decoherence, such as vibration, gravity, magnetic fields, and atomic collisions.

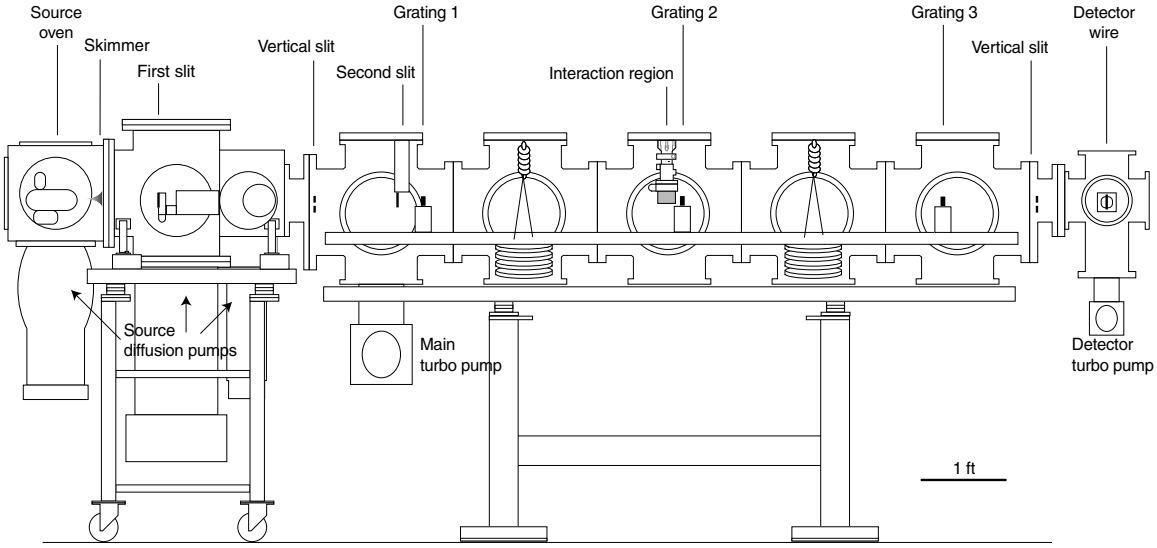

Figure 1-1: A schematic of the MIT atom interferometer, drawn to scale.

1.2 Experimental Setup

The interferometer (Fig. 1-1) consists of the source, which creates the atomic beam, the interferometer itself, which splits the beam into two paths and then recombines them into a single path, and the detector, which counts each atom to observe constructive or destructive interference in the recombined beam.

A supersonic expansion in the source creates a beam with a very narrow range of velocities, with a typical rms velocity of 3–7% of the mean. The mean velocity can be adjusted to any value between 700–3000 m/s depending on the mixture of the carrier gas (we use a mixture of rare gases—various Ar-He mixtures can cover the 1000–3000 m/s range) used to pressurize the source (20 psi above atmosphere). Heaters warm melted sodium in the source to a temperature of up to 600°C. Sodium atoms mix with the carrier gas and expand isotropically (and adiabatically) from the pressurized oven with a temperature of up to 800°C through a hotter nozzle (70 μm diameter). The skimmer (500 μm diameter) extracts the core of the supersonic expansion to form the atomic beam.

The beam is collimated by two slits spaced 90 cm apart. The first slit is 18 cm from the skimmer. The second slit is 248 cm from the detector. The slits are adjustable

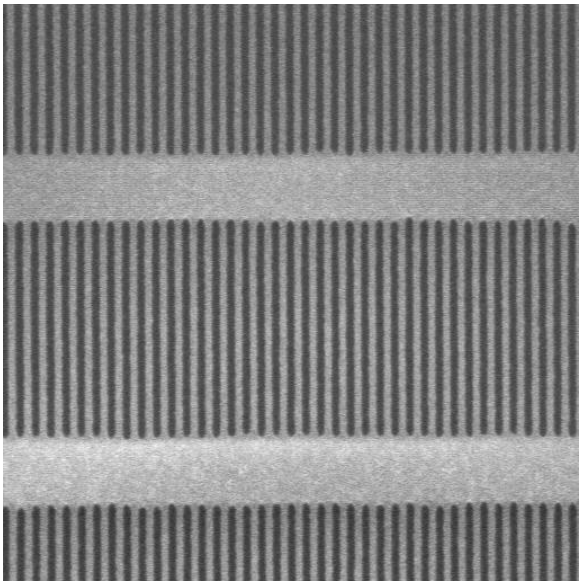

Figure 1-2: A magnified view of one of interferometer's microfabricated diffraction gratings, imaged with a scanning electron microscope. The black slots are etched gaps that allow atoms to pass through. The grating period is 100 nm.

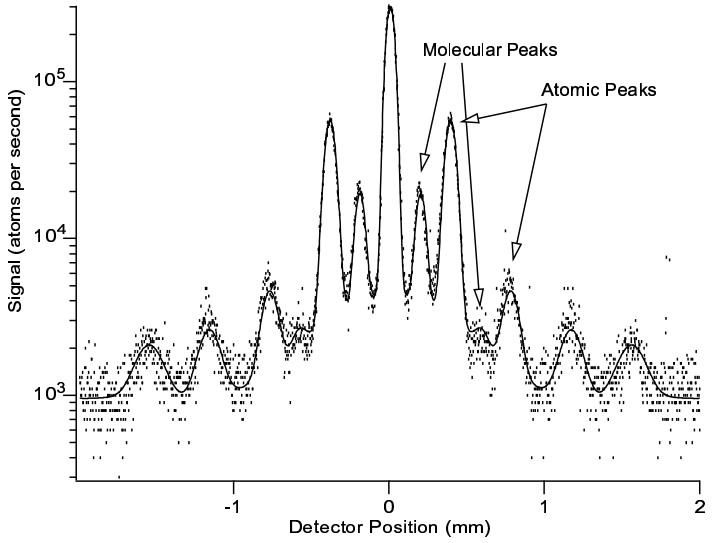

Figure 1-3: A typical diffraction pattern from a 100 nm grating.

among five widths of approximately 15, 25, 35, 45, and 55 μm. The smallest slits (used almost exclusively) are known more precisely to have widths of 11.5 μm and 16 μm for the upstream and downstream slits respectively. The beam can also be collimated vertically by continuously adjustable slits, which we leave open for improved flux. For the experiments in this thesis, the height of the beam was exactly 1 mm tall.

The detector consists of a 50 μm diameter rhenium wire, heated with a current of 140 mA (it is oxidized with pure O_2 at 10^{-4} Torr at 200 mA for 2 min prior to use for improved efficiency and noise). Sodium ionizes on the surface of the hot wire and charged screens on either side direct the ions into a channel electron multiplier to be counted individually. The detection efficiency varies in the vertical direction along the wire and depends somewhat unpredictably on the voltages of the charged screens.

The interferometer consists of three microfabricated diffraction gratings (Fig.1-2), the first works as a beam splitter, the second diffracts two of the orders back together, and the third recombines the paths into a single beam once again (Fig.1-5). We can switch between two sets of gratings in situ to use either a 100 nm or 200 nm period grating. The microfabricated chips with the 200 nm gratings have up to six windows with a grating in each window. The windows are 50–200 μm wide by 1 mm tall. The 100 nm grating chips each have two or three windows that are 1 mm wide by 5 mm tall.

The gratings are exactly 36 in. apart. The first grating is about 4 in. from the second slit, and the third grating is 21 in. from the detector wire. With the 100 nm gratings and a 1 km/s beam, the paths of the interferometer separate by 160 μm at the second grating. The interaction region separates the paths with a thin wall approximately 40 μm in thickness, allowing an interaction (for example, a gaseous medium or electric field) to be applied to just one path, creating a measurable phase shift in the interference pattern.

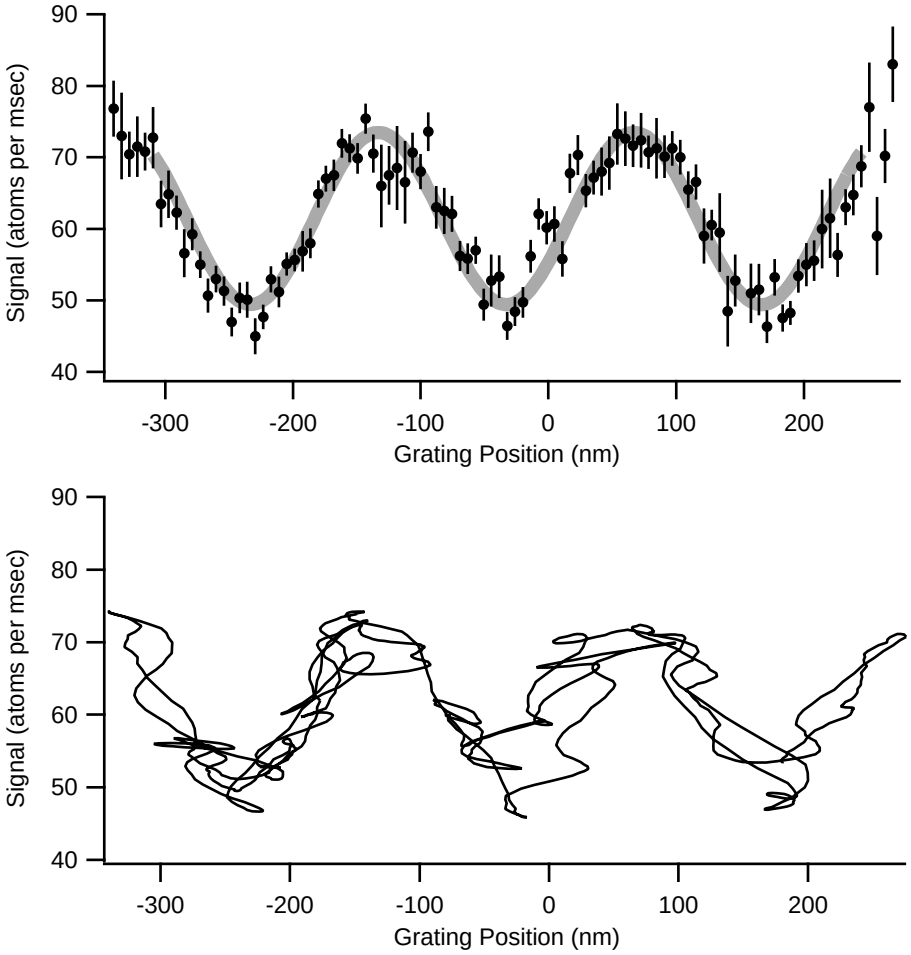

Figure 1-4: A typical interference pattern, collected in a one second interval. The detector monitors the combined signal of the two interferometer paths. Moving a grating changes the interference fringe from constructive to destructive interference. Top: the data are fit with a sine wave to determine the contrast and phase of the fringe. Bottom: the same signal is shown as a parametric plot evolving in time; the phase fluctuates due to imperfect cancellation of the mechanical vibration of the gratings. The phase is determined by monitoring the motion of the gratings with a laser interferometer.

1.3 Interferometer Alignment Requirements

To achieve interference, the three gratings that make up the interferometer must be properly aligned. If the length of the two paths in the interferometer differs by more than the coherence length, no interference will occur. If the atomic beam was a monochromatic plane wave, the two paths would interfere no matter how bad the misalignment. Our beam, however, can be represented by a mixture of plane waves, each of a different wavelength and propagation direction. If the interferometer is misaligned and the spread in wavelength and direction is too large, then the interference pattern from each wave will be out of phase with the rest, and the interference fringes will be washed out.

In this section, we will derive the alignment requirements for an atom interferometer by calculating the phase of the fringe formed by a pure plane wave in a misaligned interferometer. To account for all the possible errors in the interferometer geometry, we consider the angle of the beam, Gratings 1, and Grating 3 with respect to Grating 2, and the two inter-grating distances—from Grating 1 to 2 and from 2 to 3. All the misalignments of the interferometer can be represented as an offset or spread in these five variables (for example, if the grating is tilted about the axis of the grating wavevector, this can be represented as a spread in inter-grating distances, i.e. the gratings will be closer at the top of the atomic beam and farther apart at the bottom). We are, however, neglecting grating rotations about the beam axis in this treatment—that has been covered in detail in other sources [53, 33].

As will be shown, this analysis reveals analytic expressions for five phase errors that can destroy contrast if their spread is too large. This is a great simplification compared to earlier models of interferometer contrast—modeling the interference pattern used to involve large amounts of computation time on a Cray supercomputer [53, 101]. The following derivation, together with the theory describing the profile of the interfering orders developed in Chapter 2, gives a complete prediction for the detected interference.

The reason we can replace the computationally intensive methods, which involved

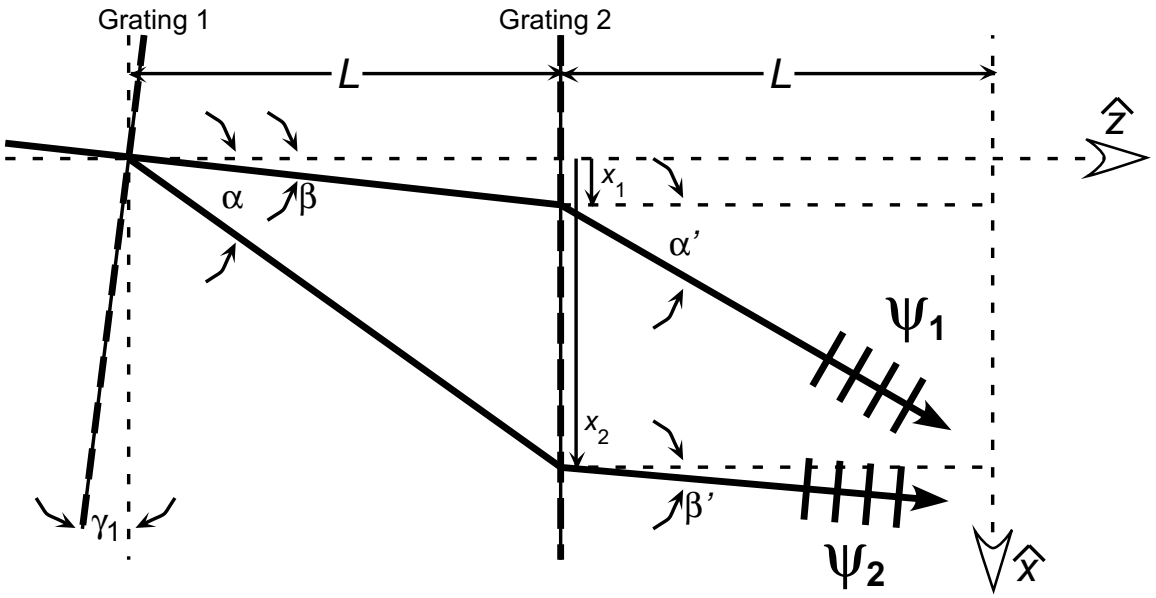

Figure 1-5: Propagation of atom plane waves in the interferometer in the presence of errors in the geometry of the gratings.

fast-fourier-transform algorithms to calculate the propagation of the diffracted wavefronts, is because we can make two approximations: first, that the distances from one grating to the next is large enough to be in the far field, and second, that there is not any significant diffraction of the profile of the beam while it propagates to the detector (i.e. the beam is wide enough so the detector is in the near field of the collimation slit diffraction). Both these conditions are easily satisfied in the MIT interferometer.

Consider the two converging paths of the interferometer in the vicinity of the third grating. We will solve for these plane waves, ψ_1 and ψ_2, under various misalignments of the first and second grating (see Fig. 1-5). We define the coordinate axis parallel to Grating 2, so we must consider error in the angle of the beam (β) and the angle of Grating 1 (γ_1) with respect to Grating 2.

The angles of propagation for ψ_1 and ψ_2 near Grating 3 are α' and β'. We can

solve for these angles using the grating equation:

$$\begin{aligned}
&\text{Grating equation at Grating 1:} && \frac{\lambda}{d} = \frac{k_g}{k} = \sin(\alpha - \gamma_1) - \sin(\beta - \gamma_1) \\
&\text{Grating equation at Grating 2:} && \frac{\lambda}{d} = \sin\alpha' - \sin\beta \quad \text{for } \psi_1 \\
& && \frac{\lambda}{d} = \sin\alpha - \sin\beta' \quad \text{for } \psi_2
\end{aligned} \tag{1.1}$$

$\lambda = 2\pi/k$ is the de Broglie wavelength and $d = 2\pi/k_g$ is the grating period.

Each plane wave is a function of the total accumulated phase:

$$\begin{aligned}
\psi \propto \exp i\big[&\text{ phase accumulated between Grating 1 and 2} \\
&+ \text{ phase due to diffraction by Grating 2} \\
&+ \text{ phase from Grating 2 to the point (x,z) } \big]
\end{aligned} \tag{1.2}$$

(We choose the transverse position of Grating 1 such that there is no phase due to its diffraction.) For each plane wave we have:

$$\begin{aligned}
\psi_1 &\propto \exp i\big[kL/\cos\beta + k_g x_1 + k(L+z)\cos\alpha' + k(x - x_1)\sin\alpha'\big] \\
\psi_2 &\propto \exp i\big[kL/\cos\alpha - k_g x_2 + k(L+z)\cos\beta' + k(x - x_2)\sin\beta'\big]
\end{aligned} \tag{1.3}$$

where $x_1 = L\tan\beta$ and $x_2 = L\tan\alpha$. Now we can find the total wavefunction in the vicinity of Grating 3 as a function of x and z. Using the fact that

$$\begin{aligned}
k_g(x_1 + x_2) &= kL\tan\beta(\sin\alpha' - \sin\beta) + kL\tan\alpha(\sin\alpha - \sin\beta') \\
&= kL(\cos\beta - \sec\beta - \cos\alpha + \sec\alpha + \sin\alpha'\tan\beta - \sin\beta'\tan\alpha)
\end{aligned} \tag{1.4}$$

due to Eq. 1.1, the result simplifies to:

$$|\psi_1 + \psi_2|^2 = 1 + \cos\big[kx(\sin\alpha' - \sin\beta') + kz(\cos\alpha' - \cos\beta') + kL(\cos\alpha' - \cos\beta' - \cos\alpha + \cos\beta)\big] \tag{1.5}$$

If the interferometer is perfectly aligned, then $\gamma_1 = 0$, $\alpha = \alpha'$, $\beta = \beta'$, $\sin\alpha -$

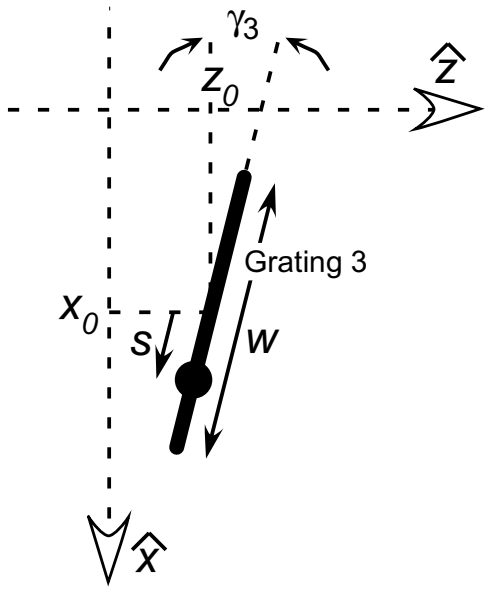

Figure 1-6: Grating 3 acts as a combined mask and detector, detecting any intensity of the wavefunction $|\psi_1 + \psi_2|^2$ that has periodicity d.

$\sin\beta = \lambda/d$, then we get the expected interference pattern:

$$|\psi_1 + \psi_2|^2 = 1 + \cos\left[2\pi\frac{x}{d} - 2\pi\frac{z}{d}\tan(\frac{\alpha+\beta}{2})\right] \tag{1.6}$$

We will now consider Grating 3 acting as a mask and detector (Fig. 1-6), with width w (the width of the detector wire), angle γ_3, and centered at position (x_0,z_0). We now have enough parameters to account for any possible misalignment in the interferometer. Consider the intensity along Grating 3 as a function of s, the distance along the grating, where $z = z_0 - s\sin\gamma_3$ and $x = x_0 + s\cos\gamma_3$, and defining $\alpha_0 \equiv \lambda/d$:

$$\begin{aligned}|\psi_1 + \psi_2|^2 = 1 + \cos\Big[&2\pi\frac{z_0}{d}[\cos\alpha' - \cos\beta']/\alpha_0 + 2\pi\frac{x_0}{d}[\sin\alpha' - \sin\beta']/\alpha_0 \\ &+2\pi\frac{L}{d}[\cos\alpha' - \cos\beta' - \cos\alpha + \cos\beta]/\alpha_0 \\ &+2\pi\frac{s}{d}[\cos\gamma_3(\sin\alpha' - \sin\beta')/\alpha_0 - \sin\gamma_3(\cos\alpha' - \cos\beta')]\Big]\end{aligned} \tag{1.7}$$

Now simplify by solving the three grating equations (Eq. 1.1) for α, α', and β' in

terms of α_0, β, and γ_1 in the limit of small angles:

$$\begin{aligned}
(\sin\alpha' - \sin\beta')/\alpha_0 &= 1 - \frac{1}{2}\gamma_1^2 + \gamma_1(\frac{1}{2}\alpha_0 + \beta) + \mathcal{O}[3] \\
(\cos\alpha' - \cos\beta')/\alpha_0 &= -(\frac{1}{2}\alpha_0 + \beta) + \mathcal{O}[3] \\
(\cos\alpha' - \cos\beta' - \cos\alpha + \cos\beta)/\alpha_0 &= \gamma_1^2(\frac{1}{2}\alpha_0 + \beta) - 2\gamma_1(\frac{1}{2}\alpha_0 + \beta)^2 + \mathcal{O}[4]
\end{aligned} \tag{1.8}$$

This leads to the following for the intensity along Grating 3:

$$\begin{aligned}
I(s) = |\psi_1 + \psi_2|^2 = 1 + \cos\Big(&2\pi\frac{x_0}{d} \\
&+2\pi\frac{x_0 - 2L(\frac{1}{2}\alpha_0 + \beta)}{d}\big[\gamma_1(\frac{1}{2}\alpha_0 + \beta) - \frac{1}{2}\gamma_1^2\big] \\
&-2\pi\frac{z_0}{d}(\frac{1}{2}\alpha_0 + \beta) \\
&+2\pi\frac{s}{d}\big[1 - \frac{1}{2}\gamma_1^2 - \frac{1}{2}\gamma_3^2 + (\gamma_1 + \gamma_3)(\frac{1}{2}\alpha_0 + \beta)\big]\Big)
\end{aligned} \tag{1.9}$$

If there is perfect alignment we get $I(s) = 1+\cos[2\pi(x_0+s)/d]$ as expected. If not, then the other parameters may have significant spread, and the interference pattern will wash out. We use the previous equation to define five sources of phase spread:

$$|\psi_1 + \psi_2|^2 = 1 + \cos\big[\phi_0 + \Delta\phi_1 + \Delta\phi_2 + \Delta\phi_3 + \Delta\phi_4 + \Delta\phi_5\big] \tag{1.10}$$

where

$$\begin{aligned}
\Delta\phi_1 =& 2\pi\frac{\Delta L}{d}\big[\gamma_1^2(\frac{1}{2}\alpha_0 + \beta) - 2\gamma_1(\frac{1}{2}\alpha_0 + \beta)^2\big] \\
\Delta\phi_2 =& 2\pi\frac{L}{d}(\frac{1}{2}\Delta\alpha_0 + \Delta\beta)\big[\gamma_1^2 - 4\gamma_1(\frac{1}{2}\alpha_0 + \beta)\big] \\
\Delta\phi_3 =& 2\pi\frac{\Delta z_0}{d}(\frac{1}{2}\alpha_0 + \beta) \\
\Delta\phi_4 =& 2\pi\frac{z_0}{d}(\frac{1}{2}\Delta\alpha_0 + \Delta\beta) \\
\Delta\phi_5 =& 2\pi\frac{w/2}{d}\big[1 - \frac{1}{2}\gamma_1^2 - \frac{1}{2}\gamma_3^2 + (\gamma_1 + \gamma_3)(\frac{1}{2}\alpha_0 + \beta)\big].
\end{aligned} \tag{1.11}$$

$\Delta\phi_2$ was calculated by assuming the detector position x_0 is centered on the interfering order, $x_0 = 2L(\frac{1}{2}\bar{\alpha}_0 + \bar{\beta})$. $\Delta\phi_5$ is the phase mismatch from $s = -w/2$ to $s = w/2$ due

to the period of the fringes along s being different than the period of Grating 3.

If the phase spread takes the form of a Gaussian distribution (such as for the velocity spread of the beam giving rise to $\Delta\alpha_0$), we have

$$\int_{-\infty}^{\infty} d\phi \, \frac{e^{-\phi^2/2\Delta\phi^2}}{\sqrt{2\pi\Delta\phi^2}} \cos[\phi_0 + \phi] = e^{-\Delta\phi^2/2} \cos\phi_0, \tag{1.12}$$

resulting in a relative contrast of $C = e^{-\Delta\phi^2/2}$ with respect to the original, where $\Delta\phi$ is the rms width of the distribution.

For a distribution of $\Delta\phi$ varying equally between $-\Delta\phi$ and $+\Delta\phi$ (such as for the detector width w),

$$\int_{-\infty}^{\infty} d\phi \, \frac{1}{2\Delta\phi} \cos[\phi_0 + \phi] = \frac{\sin\Delta\phi}{\Delta\phi} \cos\phi_0, \tag{1.13}$$

leading to a relative contrast of $C = |\frac{\sin\Delta\phi}{\Delta\phi}|$ where the full-width of the distribution is $2\Delta\phi$.

For our interferometer, typical values of the misalignment parameters and their spreads are shown in Table 1.1. Using these parameters, we have the following contributions to contrast loss:

$$\begin{aligned}
\Delta\phi_1 &\approx 2\pi\frac{\Delta L}{d}[2\gamma^3] \approx 0.002 \text{ rad} \\
\Delta\phi_2 &\approx 2\pi\frac{L}{d}[2\Delta\beta\gamma^2] \approx 0.1 \text{ rad} \\
\Delta\phi_3 &\approx 2\pi\frac{\Delta z_0}{d}\gamma \approx 16 \text{ rad} \\
\Delta\phi_4 &\approx 2\pi\frac{z_0}{d}\Delta\beta \approx 0.6 \text{ rad} \\
\Delta\phi_5 &\approx \pi\frac{w}{d}[2\gamma^2] \approx 0.3 \text{ rad}
\end{aligned} \tag{1.14}$$

The value of $\Delta\phi_3$ suggests the contrast would be almost nonexistent ($C_3 \approx 0.02$), but in fact we correct for this error by tilting the gratings about the beam axis by an angle $\theta = \gamma\delta \approx 0.5$ mrad. $\Delta\phi_3$ doesn't contribute to contrast loss, but it should be taken into account when performing the contrast search by scanning θ_1 and θ_3.

Assuming 100% initial contrast, the relative contrast as a result of errors in inter-

$\gamma = \gamma_{1,2,3} \approx 10^{-2}$	Angle of gratings about axis $\perp$ to plane of interferometer
$\beta \approx 10^{-2}$	Angle of beam with respect to Grating 2
$\Delta\beta \approx \frac{1}{2}(\frac{\text{detector wire diameter}}{\text{wire-to-collimation-slit distance}}) \approx \frac{1}{2}(\frac{50\ \mu\text{m}}{2.5\ \text{m}}) \approx 10^{-5}$	Angular spread of atomic beam
$w = 50\ \mu$m	Width of detector wire
$L = 0.75$ m	Distance between Gratings 1 and 2
$\lambda = 0.174$ Å	De Broglie wavelength for a 1 km/s sodium beam
$d = 100$ nm	Period of gratings
$\alpha_0 \equiv \lambda/d = 1.74 \times 10^{-4}$	Diffraction angle
$\Delta\alpha_0 = 5\% \times \alpha_0 = 8.7 \times 10^{-6}$	Diffraction spread due to a 5% rms velocity width of beam
$z_0 \approx 1$ mm	Difference between L and the Grating 2–3 distance
$\delta = \delta_{1,2,3} \approx 5 \times 10^{-2}$	Angle of gratings about transverse axis
$h \equiv 0.5$ mm	Height of atomic beam
$\Delta z = \Delta z_{1,2,3} \approx \frac{1}{2}\delta h \approx 12.5\ \mu$m	Spread in the longitudinal position of the gratings due to the angle of misalignment δ
$\Delta L = \Delta(z_2 - z_1) \approx \Delta z \approx 12.5\ \mu$m	Spread in Grating 1–2 distance
$\Delta z_0 = \Delta(z_3 - 2z_2 + z_1) \approx 2\Delta z \approx 25\ \mu$m	Spread in the difference of inter-grating distances

Table 1.1: Typical values and errors in the alignment of the atom interferometer.

ferometer geometry is

$$\begin{aligned} C &= C_1 \times C_2 \times C_4 \times C_5 \\ &= \left|\frac{\sin\Delta\phi_1}{\Delta\phi_1}\right| \times \left|\frac{\sin\Delta\phi_2}{\Delta\phi_2}\right| \times \left|\frac{\sin\Delta\phi_4}{\Delta\phi_4}\right| \times \left|\frac{\sin\Delta\phi_5}{\Delta\phi_5}\right| \\ &= (1 - 6\times10^{-7}) \times (0.998) \times (0.94) \times (0.985) = \ 93\% \text{ contrast} \end{aligned} \tag{1.15}$$

The size of these effects have motivated us to take more care in grating alignment when using 100 nm gratings. We have been especially careful to combat $\Delta\phi_4$ by finely adjusting the inter-grating distances using a longitudinal translation stage for Grating 2.

The alignment is much more critical for 100 nm gratings than for 200 nm gratings. All of the phase spreads are half the size for a 200 nm grating period. This mean that for a 200 nm interferometer the relative contrast would instead be $C^{1/4}$, or 98% rather than 93%.

1.4 External Decoherence Processes

Even if the interferometer is perfectly aligned, we must deal with several other external sources of possible contrast loss, which we will collectively label as sources of "decoherence." Arguably, some of these effects are not "true" decoherence, since they may just result from measuring a mixture of different interference patterns rather than a quantum process. We will consider what defines "true" decoherence in Appendix B.

1.4.1 Vibration

By far the largest source of decoherence is due to motion of the gratings. The phase of the interference fringe varies with the relative grating positions as $\phi(t) = k[x_1(t) - 2x_2(t) + x_3(t)]$. Any significant motion during the collection time of the interference pattern reduces the fringe amplitude by a factor $\exp[-\phi_{\text{rms}}^2/2]$, where $\phi_{\text{rms}}^2 = \langle\phi^2(t)\rangle_t$.

We fight this in a number of ways. First is with a passive system of vibration isolation, mounting the gratings on an elastically suspended board [56]. Second is an

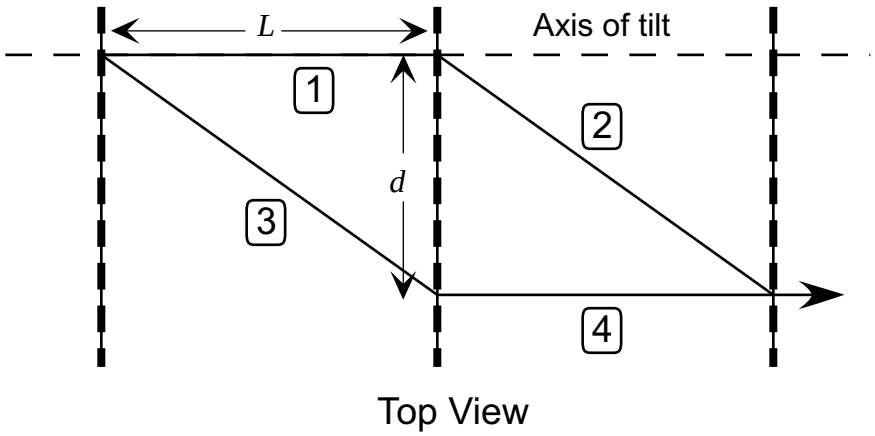

Figure 1-7: An interferometer tilted with respect to gravity experiences a phase shift. The maximum separation between the interferometer paths is $d = \frac{hL}{mv\lambda_g}$

active system of vibration cancellation and monitoring, using a light interferometer arranged with the same geometry as the atom interferometer. The light interferometer measures the quantity $x_1(t) - 2x_2(t) + x_3(t)$. We use feedback to keep this constant on a slow timescale ($\lesssim$ 1 Hz) and otherwise monitor it with the data acquisition system to correct for vibration using software. The third way to fight vibration is by operating the experiment only at night, when the magnitude of mechanical noise (arising primarily from the construction site next door) is greatly reduced.

1.4.2 Gravity

The earth's gravitational field is a source of decoherence if the plane of the interferometer is not perpendicular to vertical. The experiment by Colella, Overhauser, and Werner [23] went to great lengths to accurately observe the phase induced by gravity. We must take steps to minimize this phase or, in conjunction with the velocity spread of the beam, it will reduce fringe contrast.

Consider the interferometer tilted about the beam axis at an angle θ with respect to horizontal (Fig. 1-7). The phase induced by gravity can be calculated two different ways.

1. Atom in a potential

The atom experiences a potential $\Delta U(z) = mg\,\Delta z$. Path $\boxed{1}$ is defined as being at $z = 0$. Paths $\boxed{2}$ and $\boxed{3}$ experience a varying potential but the accumulated phases are identical and cancel out. Path $\boxed{4}$ is lower than path $\boxed{1}$ by a distance $\Delta z = d\sin\theta = \frac{hL}{mv\lambda_g}\sin\theta$.

The total phase difference between the paths is

$$\Delta\phi = \omega t = \frac{\Delta U}{\hbar} \times (\frac{\text{path length}}{\text{beam velocity}}) = \frac{mgd\sin\theta}{\hbar} \times \frac{L}{v} = 2\pi\frac{gL^2}{\lambda_g v^2}\sin\theta \quad (1.16)$$

2. Acceleration of interferometer

   Alternately, we can assume the gratings are uniformly accelerating in the z direction at a rate g. Using $\Delta\phi = 2\pi(x_1 - 2x_2 + x_3)/\lambda_g$ where $x_{1,2,3}$ are the transverse grating positions, then $x_{1,2,3} = \frac{1}{2}gt^2\sin\theta$ are the positions given a transverse acceleration $g\sin\theta$. Take $t = 0$ to be when the atom enters the interferometer. Then $x_1 = 0$, $x_2 = \frac{1}{2}g(\frac{L}{v})^2\sin\theta$, $x_3 = \frac{1}{2}g(\frac{2L}{v})^2\sin\theta$ resulting in a total phase

$$\Delta\phi = 2\pi\frac{gL^2}{\lambda_g v^2}\sin\theta \quad (1.17)$$

For typical parameters $g = 9.807$ m/s^2, $L = 1$ m, $v = 1$ km/s, $\lambda_g = 100$ nm, the phase is $\Delta\phi = (616\text{ rad})\sin\theta$. For a phase with velocity dependence $\phi \sim 1/v^2$, contrast loss is $C \sim \exp\left[\frac{1}{2}(2\phi\sigma_v/v)^2\right]$. For a 5% rms velocity distribution, we have over 40% loss in contrast for $\theta = 1^\circ$.

It is important to take this phase into account when aligning the interferometer. The best procedure is to align Grating 2 perpendicular to the optical breadboard with as much precision as possible (Gratings 1 and 3 are adjusted relative to Grating 2 using motors), measuring the angle of tilt using laser diffraction from the grating support structure. Then the board is made perpendicular to gravity using a level when it is mounted in the vacuum chamber. If at a later date new components are mounted to the board, the weight distribution may shift the angle of the interferometer, which must be corrected for by again leveling the board. We succeeded fairly well in minimizing the gravity phase—from Fig. 3-11 in Chapter 3 it can be inferred that

the contrast of our interferometer was at least 98% of what it could be with perfect alignment.

1.4.3 Magnetic Fields

A difference in magnetic field across the two paths of the interferometer will cause a phase shift in the interference pattern. The phase will be different depending on the hyperfine state of the atom and, consequently, if it is large enough it will cause a loss in fringe contrast.

Almost all of the components we use in the interferometer are moved into the beam and precisely aligned using motorized actuators. The motors are a huge convenience, having 1 μm resolution with up to 2" travel under computer control. We play a dangerous game by using them, however, because they emanate magnetic fields of several Gauss. Installation of new motor-controlled components near the paths of the interferometer should always include the use of a Hall probe to check the size of the fields produced.

We will estimate the size of the fields needed to cause contrast loss. A sodium atom in a small magnetic field ($|\vec{B}| \lesssim 10$ Gauss) experiences a potential $U = (0.77 \text{ MHz/Gauss}) \times m_F \, h \, |\vec{B}|$, where m_F is the Zeeman number of the hyperfine state. Sodium has hyperfine states $F = 1$ and $F = 2$, so the intensity of the beam is divided between $\frac{1}{4}$ of the atoms in each of $m_F = -1, 0, +1$ and $\frac{1}{8}$ in each of $m_F = -2, +2$.

Contrast will decay if there are unequal phase shifts among these states, because the fringes produced by each state won't line up with each other. If $\Delta\phi_1$ is the phase shift of the $m_F = 1$ atoms, the total interference pattern will change from $I = N + A\cos\phi_0$ to:

$$\begin{aligned} I =& N + A\frac{1}{8}\sum_{F,m_F} \cos(\phi_0 + m_F\Delta\phi_1) \\ =& N + A\Big(\frac{\cos\Delta\phi_1 + \cos^2\Delta\phi_1}{2}\Big)\cos\phi_0 \end{aligned} \tag{1.18}$$

The phase shift $\Delta\phi_1$ is the difference in the phases of each path, which is propor-

tional to the change in magnetic field in the transverse direction:

$$\begin{aligned}\Delta\phi_1 &\approx \frac{2\pi}{h}\left(\frac{dU}{dx}\right) \times (\text{separation between paths}) \times \left(\frac{\text{length of magnetic field region}}{\text{beam velocity}}\right) \\ &= 2\pi\ (0.77\ \text{MHz/G})\ \left(\frac{d}{dx}|\vec{B}|\right)\ \left(\frac{hL}{mv\lambda_g}\right)\ (\ell/v)\end{aligned} \tag{1.19}$$

As a rough estimate, a magnetic object will produce a field "bubble" of approximate length ℓ along the beam if it is a distance ℓ away from the beam. Since the field varies on the scale ℓ, we can estimate $\frac{d}{dx}|\vec{B}| \approx B/\ell$. For 100 nm gratings 1 m apart and a 1 km/s beam we have:

$$\Delta\phi_1 = (0.84\ \text{radians/Gauss}) \times B \tag{1.20}$$

A 1 Gauss field would reduce fringe contrast by a factor $(\cos\Delta\phi_1 + \cos^2\Delta\phi_1)/2 = 40\%$. For comparison, the field near a motor is about 1 Gauss at a distance of $\sim \frac{1}{2}$", but can be as high as 10 Gauss on the motor itself. Some translation stages create fields as high as 10 Gauss as well. From experience, we have found it is necessary to use μ-metal shielding and measure $\frac{dB}{dx}$ with a Hall probe whenever a motor or stage is inserted near the separated paths.

1.4.4 Background Gas

When photons are scattered in an atom interferometer, the scattered atoms are still detected (the deflection angle is only $\sim 10^{-5}$) but due to the phase shift they no longer contribute to the interference fringe, thereby causing decoherence. When atoms are scattered from a background gas, the collision removes the atom from the detected beam with near certainty. The scattering centers can be considered much like small hard spheres—the only atoms that reach the detector are ones that haven't been scattered. The scattering reduces the intensity of the fringe, but if the number of scattering events is the same in each path, the contrast of the interference fringe

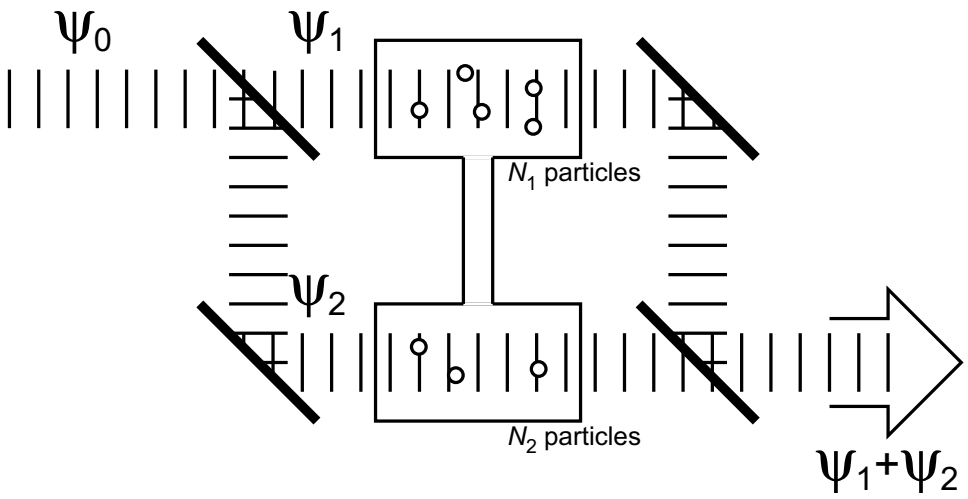

Figure 1-8: Interferometer paths exposed to the same pressure gas can experience different densities of particles due to thermal fluctuations. Unequal attenuations and phase shifts due to these fluctuations cause decoherence.

remains unchanged.[1]

However, if the number of scattering events is *not* the same in each path, decoherence *can* occur [95, 96]. This can happen due to statistical fluctuations in the gas density. Consider a region of the interferometer in which the paths are exposed to a different number of gas atoms, N_1 and N_2 (Fig. 1-8). If we know the complex index of refraction of the gas, we can predict the attenuation and phase shift of each path. We can write the wavefunction of each path as

$$\begin{aligned} \psi_1 &= \frac{\psi_0}{\sqrt{2}}\, e^{-\frac{1}{2}N_1/N_0}\, e^{i\frac{1}{2}\rho N_1/N_0}\, e^{i\phi} \\ \psi_2 &= \frac{\psi_0}{\sqrt{2}}\, e^{-\frac{1}{2}N_2/N_0}\, e^{i\frac{1}{2}\rho N_2/N_0} \end{aligned} \tag{1.21}$$

where N_0 is defined as the coherent cross-sectional area of the wavefunction divided by the total scattering cross-section. N_0 is the number of atoms required to reduce

[1]To be more precise, about half of the scattered flux in a collision goes into the forward diffracted peak, which has an angle of a few mrad (on the order of the de Broglie wavelength divided by the range of the potential). The collimation of the interferometer is of order 50 μrad, so only $\sim 1\%$ of the scattered atoms are detected, approximating zero contrast loss.

the intensity by $1/e$. ρ is the ratio of real to imaginary index of refraction, or $\rho \equiv \frac{\mathrm{Re}f}{\mathrm{Im}f}$ in terms of the scattering amplitude. ϕ is the phase difference between the two paths.

The interference of the two waves produces the following intensity

$$|\psi_1+\psi_2|^2 = \psi_0^2\Big[\frac{1}{2}e^{-N_1/N_0}+\frac{1}{2}e^{-N_2/N_0}+e^{-\frac{1}{2}(N_1+N_2)/N_0}\cos[\phi+\frac{\rho}{2}(N_1-N_2)/N_0]\Big]. \quad (1.22)$$

N_1 and N_2 come from a Poisson distribution with mean value N:

$$\big\langle|\psi_1+\psi_2|^2\big\rangle/\psi_0^2 = \sum_{N_1,N_2=0}^{\infty} P_{N_1}P_{N_2}\Big[\frac{1}{2}e^{-N_1/N_0}+\frac{1}{2}e^{-N_2/N_0}+e^{-\frac{1}{2}(N_1+N_2)/N_0}\cos[\phi+\frac{\rho}{2}(N_1-N_2)/N_0]\Big] \quad (1.23)$$

where the probability distribution is $P_{N_i} = e^{-N}N^{N_i}/N_i$. Using the fact that $\sum P_{N_1}\exp[-N_1/N_0] = \exp[-N+Ne^{-1/N_0}]$, the interference pattern is:

$$\big\langle|\psi_1+\psi_2|^2\big\rangle/\psi_0^2 = \exp[-N+Ne^{-1/N_0}]+\exp\Big[-2N+2Ne^{-1/2N_0}\cos(\frac{\rho}{2N_0})\Big]\cos\phi \quad (1.24)$$

And the contrast of the interference pattern is:

$$\exp\Big[N-Ne^{-1/N_0}-2N+2Ne^{-1/2N_0}\cos(\frac{\rho}{2N_0})\Big] \quad (1.25)$$

In the limit of large N_0 (assuming $N_0 \to \infty$, $N \lesssim N_0$, $\rho \sim 1$):

$$\begin{aligned}&\text{Contrast} \approx 1-\frac{N(1+\rho^2)}{4N_0^2}+\mathcal{O}[N^2/N_0^4]\\ &\text{Intensity} \approx e^{-N/N_0}\end{aligned} \quad (1.26)$$

Now we must estimate, N_0, the number of atoms required to attenuate the coherent area by $1/e$. The coherent cross-sectional area is determined by the width of the single slit diffraction due to the collimating slits, which is as large as $s_1 = 50$ μm horizontally and $s_2 = 500$ μm vertically. If the background gas is $L = 0.75$ m down-

stream of the slits, the coherent area is $A = L^2\lambda_{dB}^2/s_1 s_2 = 800$ nm^2 assuming a 3 km/s (0.06 Å wavelength) beam. A typical scattering cross-section for sodium with another gas is 10 nm^2, so $N_0 \approx 80$. Unfortunately, this is too large a value to observe the unique decoherence effect discussed here in our atom interferometer. To produce a 1% reduction in contrast, the intensity would already be down to 4% of its original value—leaving far too little signal-to-noise to see such a small difference.

Chapter 2

Measuring Glory Oscillations with an Atom Interferometer

2.1 Introduction

An atom interferometer is used to measure the index of refraction for sodium matter waves passing through gases of argon (Ar), krypton (Kr), xenon (Xe), and nitrogen (N_2) as a function of the sodium beam velocity. We have observed for the first time glory oscillations in the phase shift (as opposed to the attenuation) induced by the index of refraction. Our measurements are quite sensitive to the long and mid-range interatomic potential between the sodium and gas atoms, and they are inconsistent with calculations based on all of the published predictions for these potentials.

A description of the experiment and its results has been submitted for publication in Physical Review Letters. A preprint of that paper is included in Appendix A.

2.2 What Is Glory Scattering?

Glory scattering is a phenomenon in both quantum and classical systems in which the scattering of waves or particles is enhanced in the forward or backward direction. A common example of this occurs in the scattering of light from water droplets, where glory scattering can be observed with the naked eye if atmospheric conditions are

perfect—just like a rainbow, a closely related phenomenon. The easiest way to see it is from an airplane. When the shadow of the airplane passes over a cloud below, a bright region can be seen surrounding the shadow, which is caused by light scattering backward toward the sun by the spherical water droplets in the cloud. This effect can also be observed on the ground under rarer conditions. With the sun low in the sky and dew on the grass, you can sometimes see a faint halo circling the shadow of your head. This occurrence caused the Italian sculptor Benvenuto Cellini to infer that the glory of God had descended upon him, resulting in the name we give this effect today.

Even in a seemingly simple system such as this—an electromagnetic wave scattering from a dielectric sphere—the glory effect is quite complicated [11, 12, 55, 72, 73] and studies still continue to the present [21, 64]. Glory scattering is important in a wide range of other optical and acoustical systems as well: black holes [67, 40], acoustical scattering in the sun's corona [26], lidar systems [92, 93], even radar scattering that has detected buried craters on Jupiter's moons [35].

Quantum systems also exhibit glory scattering. This was first observed in atom-atom de Broglie wave scattering in the Li-Xe and K-Xe systems by E. W. Rothe *et al.* in 1962 [79]. Subsequent experiments have measured glory scattering in dozens of combinations of atom-atom and atom-molecule systems in an effort to better understand their interactions. Glory scattering has even been observed in nuclear scattering in both the backward [97, 25] and forward [75, 74] directions, though in the latter case there are reservations as to whether the evidence is conclusive [102].

2.3 Classical Glory Scattering

In classical mechanics, scattering from a spherical potential is fully described in terms of the differential cross section, $\frac{d\sigma}{d\Omega}$. This can be determined from the deflection function, $\theta(b)$ (the angular deflection for a trajectory with impact parameter b), which

can in turn be calculated from the scattering potential $V(r)$:

$$\theta(b) = \pi - 2b \int_{r_0}^{\infty} \frac{dr}{r^2 \sqrt{1 - \frac{b^2}{r^2} - \frac{V(r)}{E}}} \tag{2.1}$$

where E is the kinetic energy of the particle and r_0 is the turning point, satisfying the equation

$$1 - \frac{b^2}{r_0^2} - \frac{V(r_0)}{E} = 0. \tag{2.2}$$

The differential scattering cross section is

$$\frac{d\sigma}{d\Omega} = \frac{b}{\sin\theta} \left| \frac{d\theta}{db} \right|^{-1}. \tag{2.3}$$

The differential cross section diverges when $\sin\theta$ is zero in this equation (as long as b is non-zero and finite). The result is glory scattering—a large enhancement of the forward ($\theta = 0$) or backward ($\theta = \pi$) scattered flux.

A singularity also occurs when the term $|\frac{d\theta}{db}|^{-1}$ diverges due to an extremum in the deflection function, causing rainbow scattering.

2.4 Quantum Scattering

In a quantum system we still describe scattering in terms of the differential cross section; $\frac{d\sigma}{d\Omega}|_\theta$ is the area of the target that scatters the incident de Broglie wave into angle θ per unit solid angle. What is missing in this assessment, however, is the *phase* of the scattered wave. For a complete description, quantum scattering must be formulated in terms of the *scattering amplitude*, $f(k, \theta)$, as a function of the incident wavevector, k, and the angle of scattering θ. The scattered intensity is found from the scattering amplitude,

$$\frac{d\sigma}{d\Omega} = |f(k, \theta)|^2. \tag{2.4}$$

f represents the complex amplitude of the scattered wave in the asymptotic limit far from the scattering center. In other words, assuming an incident plane of the form

$\psi \sim e^{ikz}$, the scattered wavefunction will have the form:

$$\psi \sim e^{ikz} + \frac{f(k,\theta)}{r}\, e^{ikr} \tag{2.5}$$

This result is valid for any scattering system so long as the scattering is elastic ($k_{\text{initial}} = k_{\text{final}}$) and the scattering potential has a finite range (so that the scattered wave *has* an asymptotic limit).

Making the additional assumption that the potential is spherical, f can be expanded in spherical harmonics

$$f(k,\theta) = \frac{1}{k}\sum_{l=0}^{\infty} (2l+1)\, P_l(\cos\theta)\, e^{i\delta_l} \sin\delta_l \tag{2.6}$$

where δ_l is the phase shift of the l^{th} outgoing spherical harmonic.

δ_l is found by solving the one-dimensional Schrodinger equation for each partial wave with and without the potential $V(r)$:

$$\frac{d^2u_l(r)}{dr^2} + \left[k^2 - \frac{l(l+1)}{r^2} - \frac{2\mu}{\hbar^2}V(r)\right]u_l(r) = 0 \tag{2.7}$$

$$\frac{d^2w_l(r)}{dr^2} + \left[k^2 - \frac{l(l+1)}{r^2}\right]w_l(r) = 0 \tag{2.8}$$

We are performing the calculation in the center-of-mass frame, so μ is the reduced mass and k is the relative wavevector of the system. In the limit of large r, the wavefunctions will take the form:

$$u_l(r) \sim \sin(kr + \phi_l) \tag{2.9}$$

$$w_l(r) \sim \sin(kr + \phi_l') \tag{2.10}$$

δ_l is the difference in phase between the asymptotic wavefunctions:

$$\delta_l = \phi_l - \phi_l' = \phi_l + l\frac{\pi}{2}. \tag{2.11}$$

where we have used the fact that $w_l(r)$ can be solved exactly using spherical Bessel

functions: $\phi_l' = -l\pi/2$.

Using this prescription we can find $f(k,\theta)$ for any potential $V(r)$. For the potentials and wavevectors we are considering in this experiment, Eq. (2.6) would require a sum over hundreds of partial waves, each requiring a numerical solution to a differential equation. Instead, since the de Broglie wavelength is small compared to the range of the potential, we can replace the sum with an integral, identifying $b \equiv (l+\frac{1}{2})/k$ as the classical impact parameter

$$f(k,\theta) = k\int_0^\infty db\; b\; J_0(kb\theta)\; 2\; e^{i\delta(b)}\sin\delta(b) \tag{2.12}$$

where we have used the approximation

$$P_l(\cos\theta) = J_0\Big[\big(l+\frac{1}{2}\big)\theta\Big] \quad \text{for} \quad \theta \ll 1. \tag{2.13}$$

Furthermore, we can also use the Eikonal approximation if we assume that the kinetic energy $\hbar^2k^2/2\mu$ is much greater than the potential energy $V(r)$. In this limit, $\delta(b)$ is the phase accumulated by the wave along a straight-line, constant-speed path at fixed impact parameter b:

$$\delta(b) = \frac{-\mu}{2\hbar^2 k}\int_{-\infty}^{\infty} V\big(\sqrt{b^2+z^2}\big)dz. \tag{2.14}$$

We will use the Eikonal approximation for all of the scattering calculations in this chapter. Over the range of experimental parameters we are using, this approach is valid to 6% in comparison to the exact quantum treatment [36] (and valid to 3% for the larger mass scattering centers Kr and Xe).

If better accuracy is required the WKB approximation (requiring only that the potential change slowly over a wavelength) could be used to solve Eq. (2.7) for the phases [58]: $\delta_l = \int_{r_0}^\infty \left[\sqrt{k^2 - \frac{(l+\frac{1}{2})^2}{r^2} - \frac{2\mu V(r)}{\hbar^2}} - k\right]dr + \frac{\pi}{2}\big(l+\frac{1}{2}\big) - kr_0$. ($r_0$ is the classical turning point.) This equation is different than the incorrect versions given in dissertations [47, 56] in which the integral does not converge.

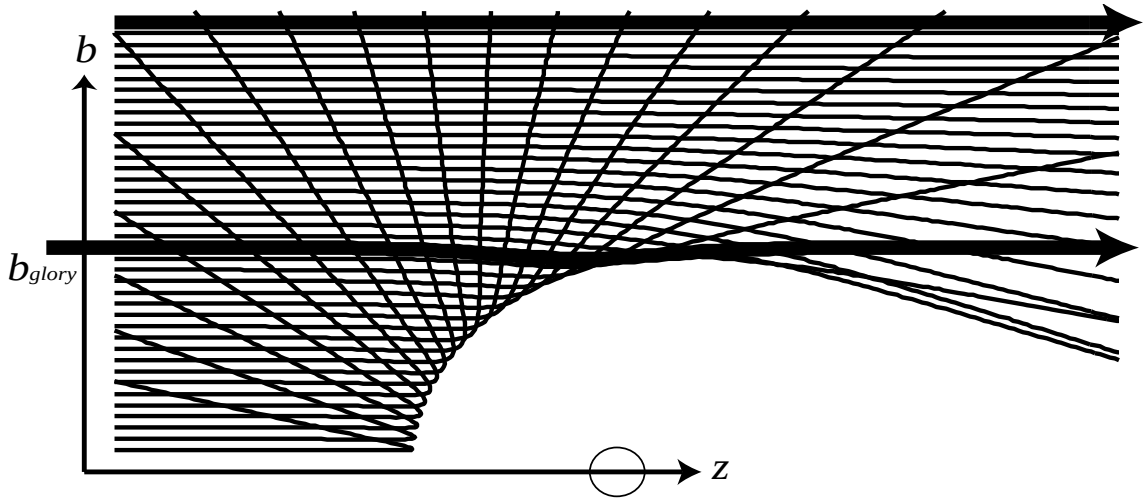

Figure 2-1: The classical trajectories of atom-atom scattering at various impact parameters, b. In quantum scattering, the forward scattered paths (bold) interfere, and their relative phase varies with the incident wavevector, k.

2.5 Atomic Scattering: Glory Oscillations

Glory *oscillations* are a manifestation of quantum glory scattering. They arise in an interatomic system when there is a close-range repulsion and a long-range attraction, forming a minimum in the interatomic potential. The forward glory scattering has contributions from two components, the wave in the long range part of the potential and the wave passing near the minimum of the potential (Fig. 2-1). These waves interfere and their relative phase depends on the de Broglie wavelength. As a function of wavelength, the glory scattering exhibits oscillations.

We will provide an example of how glory oscillations arise. The simplest model for an interatomic potential is the Lennard-Jones potential:

$$V(r) = D_e\Big[\big(\frac{r_e}{r}\big)^{12} - 2\big(\frac{r_e}{r}\big)^{6}\Big]. \tag{2.15}$$

Written in this form, D_e (the dissociation energy) is the depth of the minimum of the potential and r_e (the equilibrium distance) is the location of the minimum. This potential exhibits both the strong repulsive core and the long range r^{-6} attractive

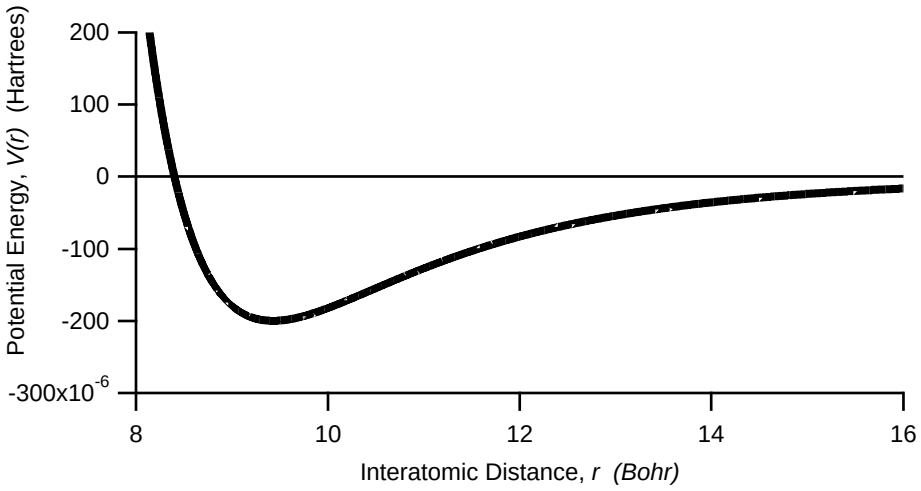

Figure 2-2: The Lennard-Jones 6-12 potential is the simplest model for the interatomic potential between sodium and argon. The depth of the potential is $D_e = 2.0 \times 10^{-4}$ H $= 5.4 \times 10^{-3}$ eV. The minimum occurs at $r_e = 9.4\ a_0 = 5.0$ Å [17].

Van der Waals regime characteristic of atom-atom interactions.

We can explicitly solve for $\delta(b)$ using Eq. 2.14:

$$\delta(b) = -D_e r_e \frac{\mu}{\hbar^2 k}\Big[\frac{63\pi}{1024}\big(\frac{r_e}{b}\big)^{11} - \frac{3\pi}{16}\big(\frac{r_e}{b}\big)^{5}\Big] \tag{2.16}$$

In glory scattering, we are only concerned with the forward scattering amplitude, $f(k) \equiv f(k, 0)$. In the semiclassical approximation the real and imaginary parts of the forward scattering amplitude are

$$f(k) = k\int_0^\infty db\ b\ \sin 2\delta(b) + ik\int_0^\infty db\ b\ \sin^2\delta(b). \tag{2.17}$$

Ref and Imf for our example potential are plotted in Fig. 2-3. Glory oscillations are evident in both the real and imaginary parts of f. Though quite similar in form, measuring Ref and Imf is quite different in practice. The famous optical theorem relates Imf to the total scattering cross section, σ:

$$\sigma = \frac{4\pi}{k}\mathrm{Im}f(k) \tag{2.18}$$

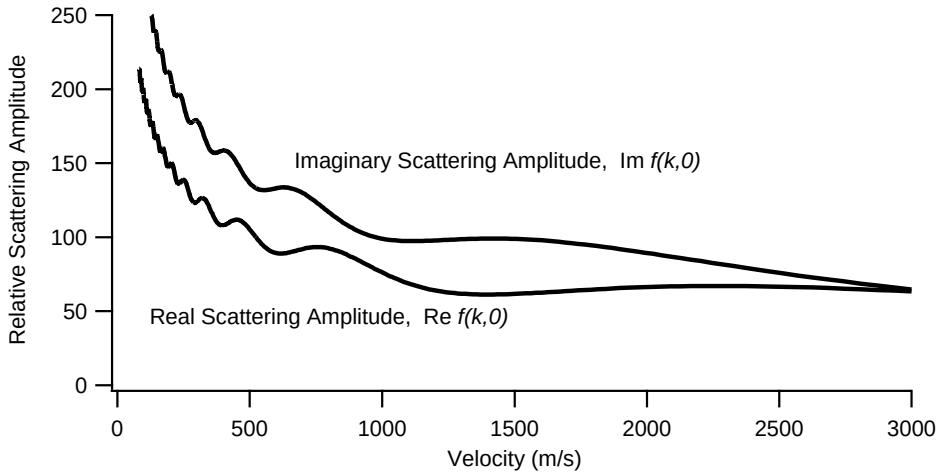

Figure 2-3: Re$f(k)$ and Im$f(k)$ for a sodium-argon Lennard-Jones potential, plotted vs the velocity, $v = \hbar k/m$.

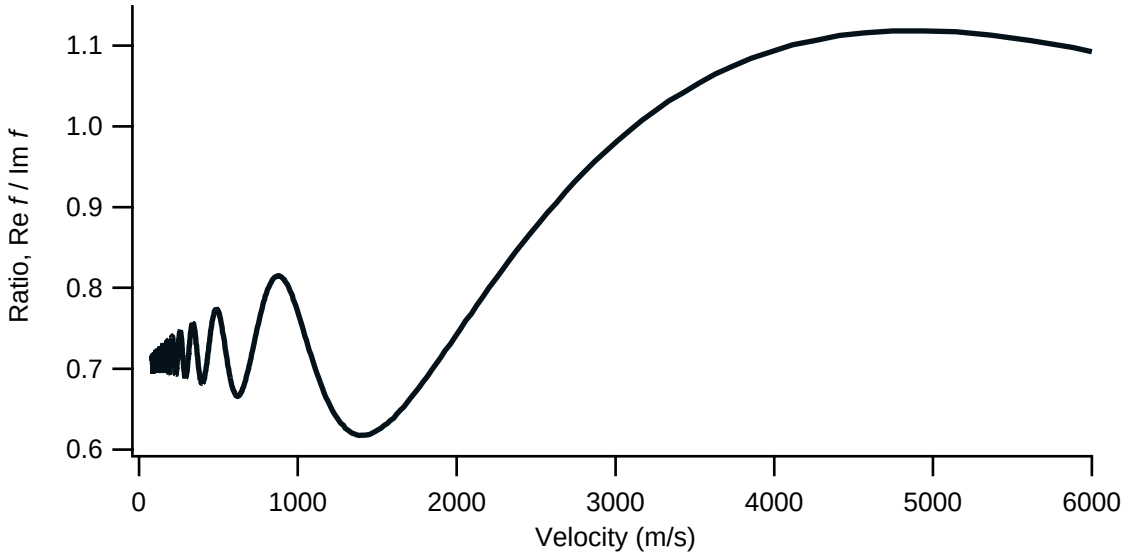

Figure 2-4: The ratio of Re$f(k)$ to Im$f(k)$ for a sodium-argon Lennard-Jones potential. The ratio asymptotes to zero in the limit of high velocity.

The natural way to measure Imf is to observe the attenuation of the beam as a function of wavevector. Ref, on the other hand, requires observing the *phase shift* of the forward scattered wave, a task that was impossible before the invention of the atom interferometer.

Glory oscillations in Imf were first observed by E. W. Rothe *et al.* in 1962 in the Li-Xe and K-Xe systems [79] and subsequently measured in dozens of combinations of atom-atom and atom-molecule systems. There are drawbacks, however, in using just Imf to map out glory oscillations and obtain information on the interatomic potential. The difficulty lies in the fact that the oscillations are not very strong in the imaginary part (from the top curve in Fig. 2-3 it can be seen that the oscillations barely create any periodic minima at all). Moreover, the strong $v^{-2/5}$ velocity dependence of Imf can obscure the small oscillations. Also, a measurement of Imf will be dependent on the gas density, which is hard to determine accurately and which may fluctuate. Fluctuations in the flux of the incident beam causes problems too.

With the atom interferometer we can measure Ref as well as Imf. By simultaneously measuring both, we can determine the ratio, Ref/Imf, which cancels out the biggest sources of error. Measuring this quantity cancels out the strong velocity dependence and completely eliminates variations due to beam flux or pressure fluctuations. Furthermore, the glory oscillations themselves are enhanced, because the oscillations are much stronger in Ref, and oscillations are 90° out of phase in Ref compared to Imf, so by taking the ratio they are even larger. These combined effects can be seen by comparing the glory oscillations in Ref/Imf plotted in Fig. 2-4 with the oscillations in Fig. 2-3.

2.6 Measuring Atomic Scattering: The Index of Refraction

f describes the scattered wavefunction for a single atom scattering from a single scattering center. In practice we cannot measure a single scattered wavefunction—we

must instead measure the scattering of atoms from a gas containing many scattering centers. Measuring the wave scattered into the forward direction by the gas is simply a measure of the index of refraction, n, which is quite closely related to f. The index of refraction is complex, with the real part of n representing the change in phase of the wave and the imaginary part representing the attenuation. Just as in optics, a plane wave inside the medium has the wavefunction

$$\psi(z) \sim e^{i\,n\,k_{\rm lab}\,z} \tag{2.19}$$

so passing through a gas of length L modifies the wavefunction by the factor

$$e^{i\phi}e^{-\eta} \tag{2.20}$$

where

$$\phi = (\mathrm{Re}[n] - 1)\,k_{\rm lab}\,L \tag{2.21}$$

$$\eta = \mathrm{Im}[n]\,k_{\rm lab}\,L \tag{2.22}$$

In the next section we will show how the quantities ϕ and η can be directly measured using the atom interferometer.

By assuming that the range of the potential is smaller than the inter-particle spacing in the gas (i.e. $r_e \ll {n_d}^{-\frac{1}{3}}$), we can use the theory of independent multiple scatterers [61, 71, 85, 17] in which the forward propagating wave is the sum of the incident plane wave plus the scattered spherical waves from each scattering center. n can then be determined from f:

$$n(k_{\rm lab}) = 1 + \frac{2\pi n_d}{k_{\rm lab}}\left\langle \frac{f(k)}{k} \right\rangle \tag{2.23}$$

where n_d is the density of scatterers. The brackets, $\langle ... \rangle$, indicate an average over all relative wavevectors due to the thermal distribution of atoms in the gas. Up to this point, we have assumed the scattering centers are not fixed potentials but rather

interactions with other masses, hence the quantity $f(k)$ is calculated in the center-of-mass frame with reduced wavevector k and reduced mass μ. Once the thermal average over k is computed, n can be found in the lab frame as a function of the lab frame wavevector, $k_{\rm lab}$.

In terms of the particle *velocities* we have:

$$n(v) = 1 + \frac{2\pi n_d \hbar^2}{\mu m v} \left\langle \frac{f(v_{\rm rel})}{v_{\rm rel}} \right\rangle \tag{2.24}$$

where v is the velocity of the beam (or lab velocity) and $v_{\rm rel}$ the relative velocity satisfying the relations

$$v = \frac{\hbar}{m}\, k_{\rm lab} \tag{2.25}$$

$$v_{\rm rel} = \frac{\hbar}{\mu}\, k. \tag{2.26}$$

There are currently two conflicting explanations in the literature on how to perform the thermal averaging. We will use the following, which is explicitly derived in [47] and agrees with that of Dalgarno *et al.* [38]:

$$\left\langle \frac{f(v_{\rm rel})}{v_{\rm rel}} \right\rangle = \int_0^\infty \frac{f(v_{\rm rel})}{v_{\rm rel}} \Big[\frac{2v_{\rm rel}}{\sqrt{\pi}\alpha v}\, e^{-\frac{v^2+v_{\rm rel}^2}{\alpha^2}}\, \sinh\big(\frac{2vv_{\rm rel}}{\alpha^2}\big) \Big] dv_{\rm rel} \tag{2.27}$$

where $\alpha \equiv 2k_B T/m_T$ (m_T is the mass of the target atom). In the limit $T \to 0$ the expression in brackets above reduces to a delta function, $[\dots] \to \delta(v_{\rm rel} - v)$, as expected.

An alternative derivation by Vigue and coworkers [17] expresses the thermal average over a different quantity,

$$n(v) = 1 + \frac{2\pi n_d \hbar^2}{\mu m} \left\langle \frac{f(v_{\rm rel})}{v_{\rm rel}^2} \right\rangle \tag{2.28}$$

with a very different weighting function,

$$\left\langle \frac{f(v_{\rm rel})}{v_{\rm rel}^2} \right\rangle = \int_0^\infty \frac{f(v_{\rm rel})}{v_{\rm rel}^2} \left[\frac{2v_{\rm rel}^2}{\sqrt{\pi}\alpha v^2}\, e^{-\frac{v^2+v_{\rm rel}^2}{\alpha^2}} \left(\cosh\left(\frac{2vv_{\rm rel}}{\alpha^2}\right) - \frac{\alpha^2}{2vv_{\rm rel}} \sinh\left(\frac{2vv_{\rm rel}}{\alpha^2}\right) \right) \right] dv_{\rm rel}. \tag{2.29}$$

The differences between these weighting functions are negligible in this experiment. They differ most at low velocity for small target mass atoms. For the sodium-argon Lennard-Jones potential, the difference is a maximum of 0.3%.

With the atom interferometer we can measure the real and imaginary parts of n. We measure the ratio of real to imaginary components,

$$\rho(v) = \frac{\mathrm{Re}[n(v)-1]}{\mathrm{Im}[n(v)]} \tag{2.30}$$

which is quite similar to the ratio $\mathrm{Re}f/\mathrm{Im}f$. In fact, $\rho(v)$ differs only due to the thermal averaging, and is equal to $\mathrm{Re}f/\mathrm{Im}f$ in the limit of low temperature gas, high beam velocity, or large target mass. We have mentioned the advantages of measuring the ratio of real to imaginary components. Experimentally, the most important of these is that ρ has no dependence on the gas density n_d. The pressure of the gas cannot be measured precisely because of the small size of the gas cell and the small pressures involved. Measuring ρ rather than n removes this experimental uncertainty.

Fig. 2-5 plots ρ for a 6-12 Na-Ar potential with room-temperature thermal averaging (we used a room-temperature gas in all measurements) and without thermal averaging (equivalent to a zero temperature gas). The thermal averaging dramatically damps the glory oscillations at low velocity. The damping also depends strongly on the mass of the scattered particle compared to the scatterer. The damping is less for a heavier gas (Kr and Xe) and greater for a lighter gas (N_2).

2.7 Finding ρ from an Interferometer Measurement

A plane wave undergoes an attenuation and phase shift $\psi \rightarrow e^{-\eta}e^{i\phi}\psi$ after passing through a gas, where $\eta = \mathrm{Im}[n]k_{\rm lab}L$ and $\phi = (\mathrm{Re}[n]-1)k_{\rm lab}L$. Our goal is to measure η and ϕ to find $\rho = \eta/\phi$. To do this we expose one of the interferometer's paths to a

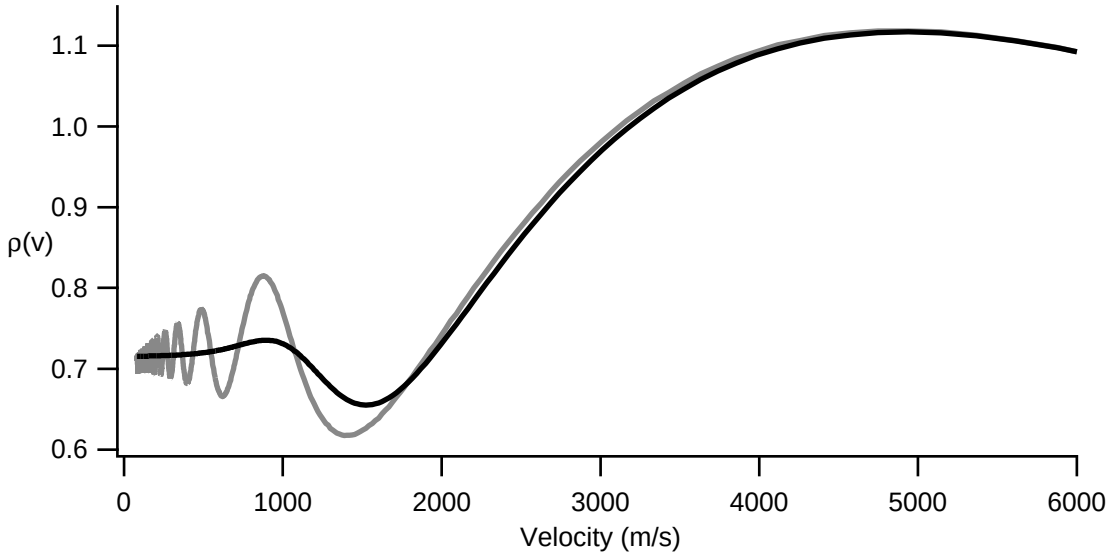

Figure 2-5: A comparison of thermally averaged ratio $\rho(v) = \mathrm{Re}[n(v) - 1]/\mathrm{Im}[n(v)]$ for a sodium-argon 6-12 potential at $T = 0°\mathrm{K}$ (grey), and at $T = 300°\mathrm{K}$ (black). In the limit of zero temperature, ρ is equivalent to $\mathrm{Re}f/\mathrm{Im}f$.

gas, leaving the other to propagate through vacuum.

In the absence of gas, we observe an interference pattern in the detected signal I_0 that depends on the position x of one of the gratings,

$$I_0(x) = |\psi_1 + \psi_2 e^{ik_g x}|^2 = N_0 + A_0 \cos(\phi_0 + k_g x), \tag{2.31}$$

where ψ_1 and ψ_2 are the wavefunctions of the two paths. When the path ψ_2 is exposed to the target gas, the interference pattern becomes

$$I_{gas}(x) = |\psi_1 + e^{-\eta} e^{i\phi} \psi_2 e^{ik_g x}|^2 = N_{gas} + A_{gas} \cos(k_g x + \phi_{gas}) \tag{2.32}$$

By inspection, the amplitude of the new interference pattern is different by the factor $e^{-\eta} = A_{gas}/A_0$. Similarly, the phase of the interference pattern is different by $\phi = \phi_{gas} - \phi_0$.

We fit the measured interference patterns $I_0(x)$ and $I_{gas}(x)$ with a sine function to determine the amplitudes, A_0 and A_{gas}, and the phases, ϕ_0 and ϕ_{gas}. From these

values we can determine ρ:

$$\rho = \frac{\phi_{gas} - \phi_0}{\ln A_{gas} - \ln A_0} \tag{2.33}$$

The alternating measurement of $I_0(x)$ and $I_{gas}(x)$ is repeated for a long duration of time (30–45 min) to improve the statistical precision of the measurement. During that time, we alternate frequently between measurements of $I_0(x)$ and $I_{gas}(x)$ to reduce the error due to thermal drift, which changes the phase of the interference pattern as the relative positions of the gratings drift.

We have mentioned the benefits of measuring the ratio ρ instead of the attenuation or phase shift individually—the measurement is independent of many experimental parameters like the gas pressure and the gas cell length. There are other advantages, too. Typically, we cannot avoid measuring more than just the two paths ψ_1 and ψ_2—some of the extra atoms reach the detector after passing outside the gas cell, some are attenuated by the gas cell, and still others are background counts that don't originate from the atom beam at all. These signals change the predictions for N_0 and N_{gas}, but since they don't contribute to the interference amplitude, they do not influence the measurement of ρ.

There do exist pairs of extra paths that can interfere at the detector, but for the most part these are avoidable. This is the largest source of possible systematic error, however, which we will fully investigate in Section 2.12.

2.8 Experimental Apparatus

The experiment for measuring the index of refraction has received three recent improvements, allowing us to map out glory oscillations in four different systems after many nights of data acquisition:

1. We have hooked up four different gases to the gas cell, Ar, Kr, Xe, and N_2, with the ability to switch quickly from one to the next.

2. A 100 nm grating interferometer has been installed which doubles the range of velocities over which $\rho(v)$ can be measured.

3. The beam velocity is now determined by a set of pre-mixed, certified, mixtures of rare gases, providing a reproducibility to the beam velocity that was not possible with the gas flow controllers used previously.

Other improvements have been made as well since the last published measurement of the index of refraction [83], which are described in detail in [56]. The two most notable improvements are in the gas cell, which has been made with a thinner wall to fit between the interferometer paths, and the gas delivery system, which has a much smaller time constant for filling the gas cell allowing us to take better measurements more quickly. These improvements and the general experimental procedure for making an index of refraction measurement are described in detail in [56]. We will give a brief description here.

The primary new component for measuring the index of refraction is the gas cell. Our gas cell [47, 56] was designed and constructed by Ed Smith in MIT's Microsystems Technology Laboratory. It consists of a 10 μm thin silicon wafer anodically bonded to a borosilicate glass substrate with a matching coefficient of thermal expansion, so that the wafer will not break due to temperature changes. The wall, or septum, of the cell is thin enough to fit between the two paths of the interferometer so that one path can be exposed to gas while the other is unaffected. The effective thickness of the septum is 28 μm due to the fact that the wafer is not perfectly flat. 5 mm wide channels are cut into the glass substrate to create the volume of the cell and to provide thin (200 μm) ports for the entrance and exit of the beam. The glass also has a hole for the gas inlet through which the cell can be filled and emptied of gas by means of a supply line. The gas cell is mounted on a stage with three computer-controlled degrees of freedom—translation to move the septum in and out of the beam, pitch to line up the septum parallel to the beam line, and tilt to line up the septum parallel to the height of the skinny 1 mm tall beam. The gas cell is positioned just upstream of the second grating, where the path separation is greatest (Fig. 2-6).

The supply lines feeding the gas cell have an i.d. of $\frac{3}{16}$". This is much wider than the supply lines used to be, allowing us to cycle the gas into and out of the cell much more quickly. It also allows us to make measurements with a fixed pressure of gas in

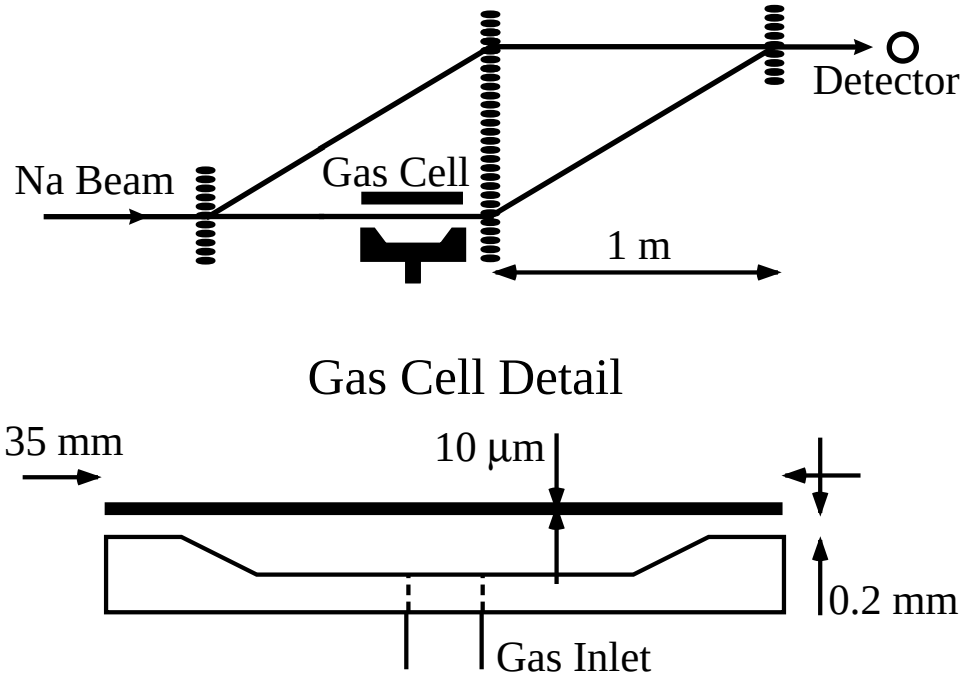

Figure 2-6: A top down view of the interferometer and gas cell.

the cell, rather than with a slowly changing pressure, eliminating a source of possible systematic error. Computer controlled valves located in the gas line can instantly close off the gas supply from the reservoir and open the gas cell inlet to the main chamber vacuum to rapidly empty the cell of gas. The gas line exits the vacuum via a feedthrough and is hooked up to an external reservoir of gas at a pressure of a few mTorr. The pressure is adjusted by the equilibrium between the leak rate of 20 psi gas into the reservoir (set by a needle valve) and the vacuum turbo pump speed (set by a gate valve in front of the pump).

2.9 Experimental Results

We collected measurements of $\rho(v)$ over sodium beam velocities of 1–3 km/s for gases Ar, Kr, Xe, N_2. Figs. 2-7, 2-8, 2-9, and 2-10 show the measurement of ρ vs v for each gas. Data for each gas are plotted twice. In the first, each data point represents an average of 30–45 min of data taken continuously, alternating between a single, fixed

pressure and no pressure. In the second, each data point represents an average of all measurements taken at a particular velocity on a single night (an average of 1–4 measurements at different pressures). The data were taken over a total of 21 nights between Dec 2000 and July 2001, with ρ measured at 2–3 different velocities each night.

The data points are shown in open circles ($\circ$) for data taken with the 100 nm grating interferometer and closed circles ($\bullet$) for the 200 nm data. For comparison, the data points taken with the older interferometer, published in [83], are shown as squares ($\square$) with the published statistical error bars. The curves shown are calculations of ρ derived from various predictions for the interatomic potential.

The data points in the second figure show a both the statistical and systematic error bars. The extent of the statistical error is represented by the length of the error bar inside the cap. The estimated systematic error, discussed in Section 2.12, is added on to the outside of the cap.

2.10 Comparison with Predictions of ρ

The alkali-rare-gas interaction has been studied extensively since the 1960's, with most of the effort focused on the sodium-rare-gas (especially Na-Ar) systems. It is desirable to study these systems for the sake of improving and testing our understanding of these systems and as a step toward understanding more complicated systems. There are practical reasons as well. If our knowledge improves, alkali-rare-gas mixtures hold promise as candidates for future excimer laser designs [86]. The studies could also be useful to build a better light blub; current sodium vapor lamp design evolves from empirical observations of what works rather than from a fundamental understanding of the collision dynamics involved. Other branches of physics would also find improvements in the analysis quite useful. The collision broadening of alkali resonance lines is important in understanding the spectra of such diverse things as flames, laser-induced plasmas, and brown dwarfs [5].

Prior to this experiment, Na-rare-gas potentials were found by *ab initio* calcula-

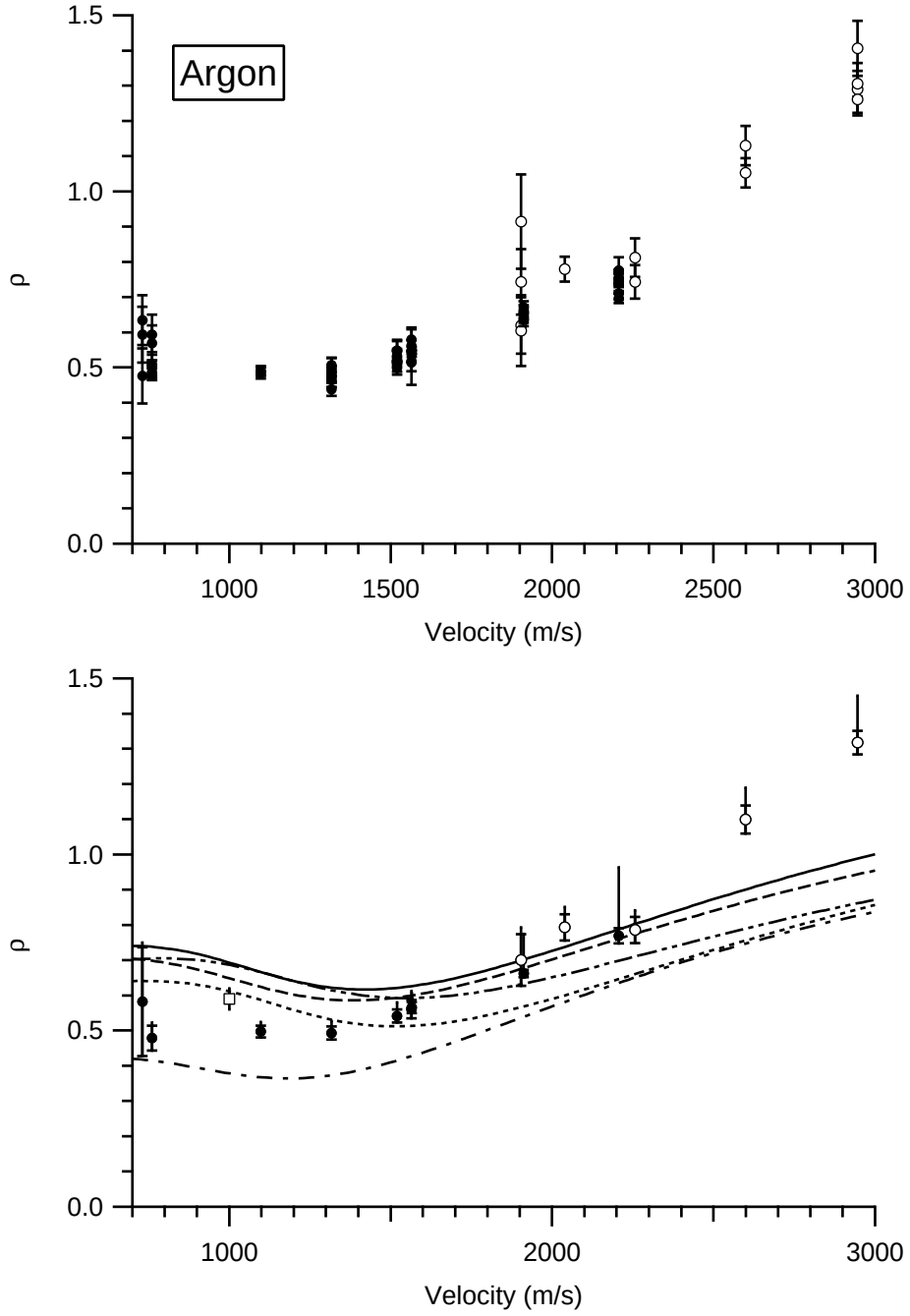

Figure 2-7: The ratio of real to imaginary index of refraction, ρ, for sodium atoms with velocity v in Ar. Top: Each measurement is taken at a different pressure and velocity ($\bullet$ using 200 nm gratings, $\circ$ 100 nm). Bottom: All measurements at a single velocity are averaged and systematic error bars are included. A comparison is made with theoretical predictions, [1](—), [28](− − −), [38](· · ·), [100](· − ·−), [98](· · − · ·−), and an older measurement [83](□).

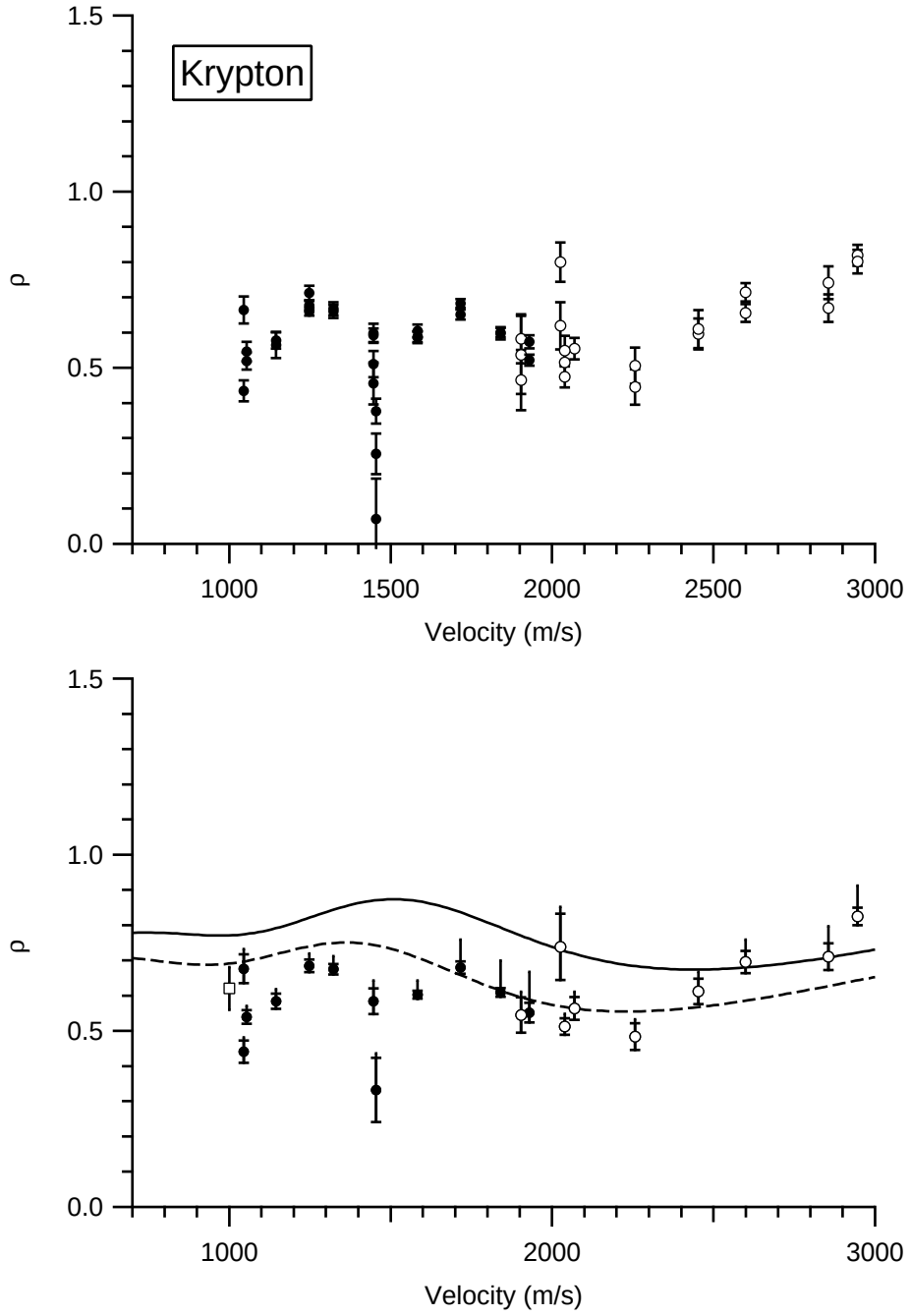

Figure 2-8: The ratio of real to imaginary index of refraction, ρ, for sodium atoms with velocity v in Kr. Top: Each measurement is taken at a different pressure and velocity ($\bullet$ using 200 nm gratings, $\circ$ 100 nm). Bottom: All measurements at a single velocity are averaged and systematic error bars are included. A comparison is made with theoretical predictions, [1](—), [31](− − −), and an older measurement [83](□).

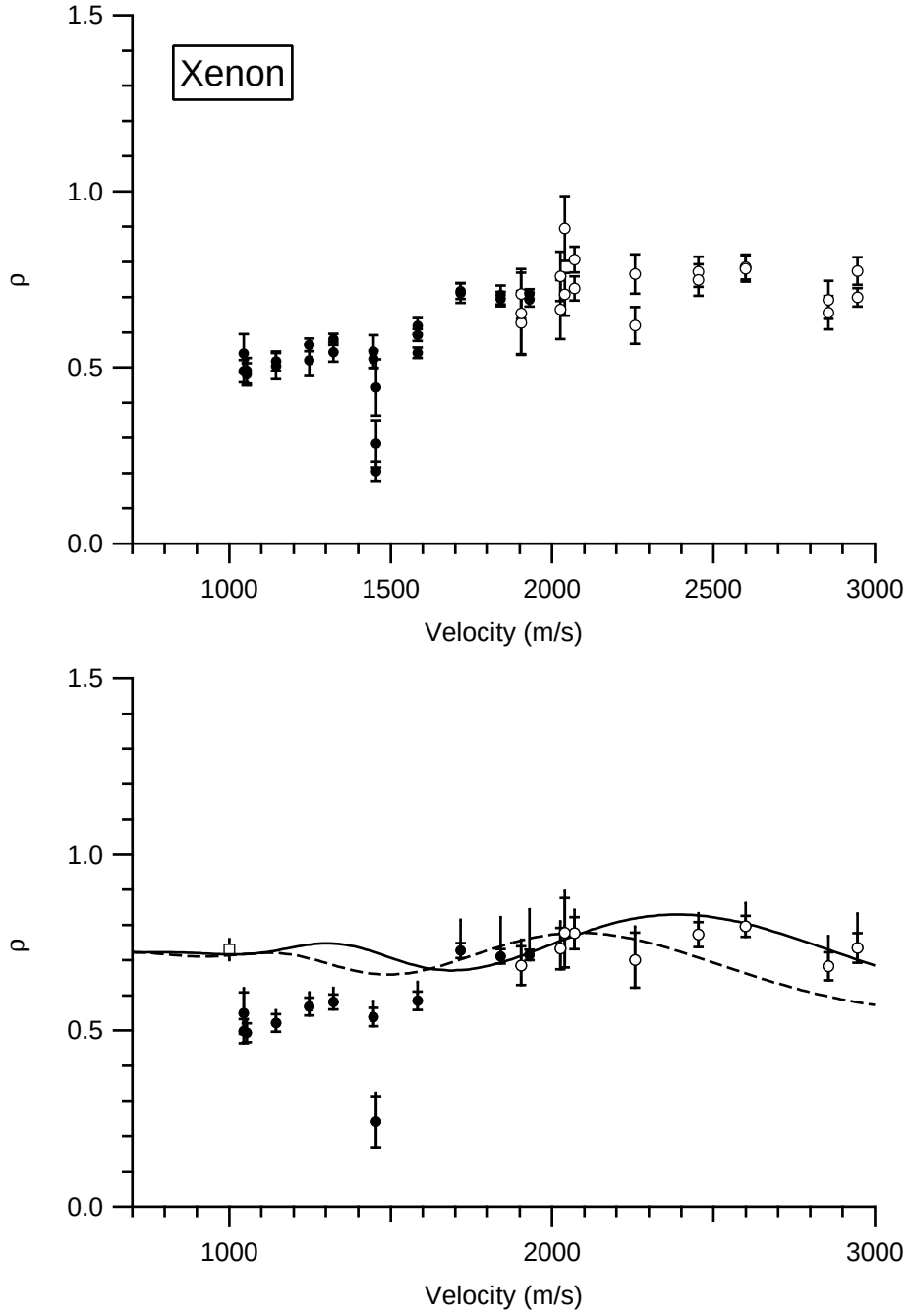

Figure 2-9: The ratio of real to imaginary index of refraction, ρ, for sodium atoms with velocity v in Xe. Top: Each measurement is taken at a different pressure and velocity ($\bullet$ using 200 nm gratings, $\circ$ 100 nm). Bottom: All measurements at a single velocity are averaged and systematic error bars are included. A comparison is made with theoretical predictions, [6](—), [31](− − −), [13](· · ·), and an older measurement [83](□).

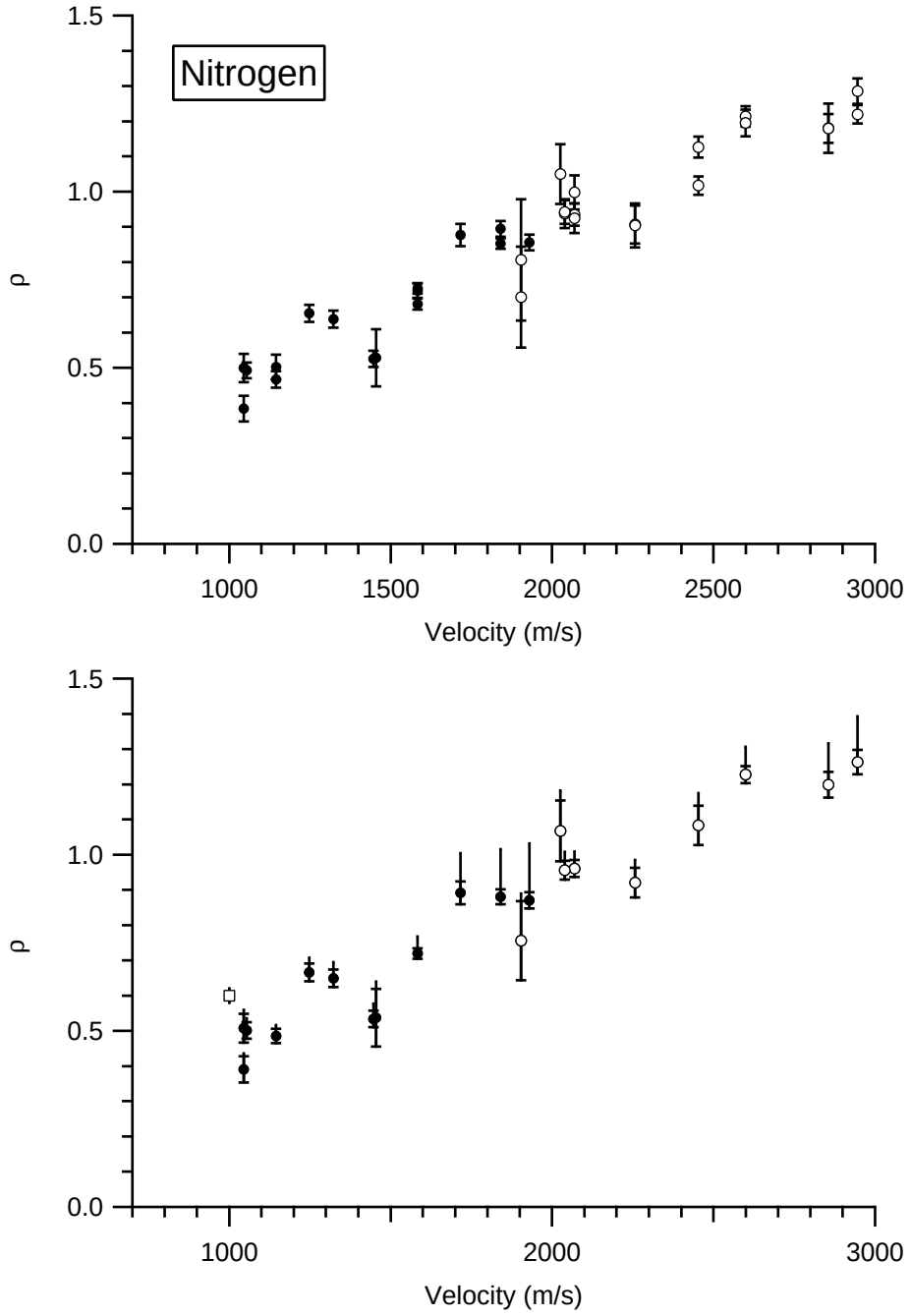

Figure 2-10: The ratio of real to imaginary index of refraction, ρ, for sodium atoms with velocity v in N_2. Top: Each measurement is taken at a different pressure and velocity (• using 200 nm gratings, ∘ 100 nm). Bottom: All measurements at a single velocity are averaged and systematic error bars are included. A comparison is made with an older measurement [83](□).

tions [7, 9, 76, 82, 98, 99, 77, 24, 30, 60] or by either spectroscopic or beam scattering experiments. One method of obtaining spectroscopic data is by measuring the "far wings" of a collision broadened resonance line, also known as the "spectroscopy of the transition state" or the study of "radiative collisions" [106, 51, 50, 104]. Alternately (and providing a more precise determination of the interatomic potential) laser spectroscopy is performed on weakly bound Van der Waals molecules produced in the supersonic expansion of a molecular beam source, including Refs. [87, 41, 100, 2, 107, 108, 10, 6], plus many by Pritchard and coworkers [14, 3, 78, 59, 43]. Beam scattering experiments to determine the potential take the form of either measuring the angular dependence of the differential cross section for crossed molecular beams [14, 29] or the velocity dependence of the total scattering cross section [31, 13, 32, 103, 27].

Prior studies of the Na-N_2 potentials have been limited to a few fairly recent studies involving a theoretical approach or far-wing spectroscopy [46, 52, 69, 70, 42]. The relative lack of understanding in this area can be attributed to the difficulty of constructing the atom-molecule interaction potential. Both known predictions, [69, 70] and [46], model the Na-N_2 ground state with a Lennard-Jones potential, but in each case the C_6 coefficient, representing the long-range Van der Waals attraction, is estimated to be zero, predicting a purely repulsive potential. Our measurements can rule out these predictions immediately (without even knowing the form of the potential) since $\rho(v) < 0$ for all v for a purely repulsive potential, yet we measure $\rho(v) > 0$ for all chosen v.

The predictions of ρ for the sodium-rare-gas systems all show disagreement with the measurements we have taken (as well as disagreement with each other). The disagreement with the data is likely due to how sensitive ρ is to the shape of the potential near the minimum. This is precisely where understanding of the interatomic potential is weakest as it is the transition region between the repulsive core and the long-range Van der Waals attraction.

The Van der Waals potential, for instance, is very hard to predict in this region. At larger distances it is very accurately predicted by a power series expansion of

inverse even powers of the interatomic distance:

$$V_{\mathrm{VdW}}(r) = -\frac{C_6}{r^6} - \frac{C_8}{r^8} - \frac{C_{10}}{r^{10}} \dots \tag{2.34}$$

The coefficients can be deduced experimentally (the best method is high-resolution Feshbach spectroscopy), calculated (if the system is not too complex), or estimated as is done in Refs. [89, 99]:

$$C_{2n+4} = \left(\frac{C_{2n+2}}{C_{2n}}\right)^3 C_{2n-2} \tag{2.35}$$

Unfortunately, the Van der Waals expansion doesn't converge. (This can be demonstrated using Eq. 2.35.) The series works best however if it is cut off at the smallest term (at a particular r, one of the terms C_n/r^n will be smallest), and the error in this expansion will be on the order of the size of that term. To create a smoother approximation, various damping functions have been proposed to gradually turn off the Van der Waals terms at small r, as the error begins to grow and the repulsive part begins to dominate. Models for damping the Van der Waals potential and matching it to the core potential rely on (sometimes *ad hoc* [9]) methods of cutting off the series term-by-term, either sharply [98], or smoothly [99, 38], as it diverges at small distances.

2.11 Exploring Potentials that Fit the Data

We have found no predicted potentials that agree with our measurements of ρ. Unfortunately, the "inverse problem of scattering"—deriving the potential $V(r)$ from knowledge of $f(k)$—is not possible [66, 65, 16]. The difficulty lies in the processes of unwrapping the function $\delta(b)$ from its appearance in the term $\sin\delta(b)$ in the function for $f(k)$. Finding $V(r)$ is additionally complicated by the fact that $V(r)$ is not unique given $f(k)$.

Despite these difficulties, we can still test modifications to various potentials to find ones that do agree with our measurements. This provides insight into where

the theoretical potentials fail. To explore these modifications we will make some simplifications to the process of deriving $f(k)$ from $V(r)$.

Any interatomic potential that has a minimum can be expressed in the form:

$$V(r) = D_e\, g\Big(\frac{r}{r_e}\Big) \tag{2.36}$$

where D_e is the depth (in energy) of the potential well at its minimum and r_e is the location of the minimum. $g(x)$ is a dimensionless function describing the shape of the potential. By definition, $g(1) \equiv -1$. With this substitution we can find a new equation to replace the Eikonal approximation for $\delta(b)$ in Eq. 2.14,

$$\delta'(y) = -\alpha \int_0^\infty dx\; g\big(\sqrt{x^2+y^2}\big) \tag{2.37}$$

where we have defined the quantity

$$\alpha \equiv \frac{D_e r_e \mu}{k\hbar^2} = \frac{D_e r_e}{mv\hbar}. \tag{2.38}$$

Neglecting thermal averaging we have

$$\rho(v) = \frac{\int_0^\infty y \sin 2\delta(y) dy}{\int_0^\infty 2y \sin^2 \delta(y) dy} \tag{2.39}$$

which depends only on two things—the dimensionless parameter α and the dimensionless shape $g(x)$.

One conclusion we can draw immediately is that since ρ depends only on the product $D_e r_e/v$, our measurement of ρ can give *no* information on either the well depth or location individually. This also means that the effect on ρ of changing D_e or r_e is the same as scaling the velocity. We could determine the product $D_e r_e$ this way by scaling the velocity axis of the $\rho(v)$ curve until the glory oscillations fit the predictions.

The max and min of the glory oscillations in ρ match up fairly well with the predictions, however, which suggests that the predicted potentials are accurate in

their knowledge of D_e and r_e, even though the shape $g(x)$ could use improvement. We also know D_e and r_e are accurate to within 10% due to agreement among different methods (for example, see Ref. [17]). Since the disagreement lies in the shapes of the potentials, we have explored various modifications to $V(r)$ without changing D_e and r_e to see what potentials would agree.

Most of the model potentials suggested in the literature consist of functions with many parameters, for example: the distance scale for exponential core repulsion, the energy at $r = 0$, the matching radius between core and Van der Waals regimes, or the strength and distance scale for damping of each of the Van der Waals coefficients. After an exhaustive empirical study of the change in $\rho(v)$ affected by modifying these parameters (and combinations of parameters) for each suggested potential, we found surprisingly little control could be had over shaping $\rho(v)$ in the ways necessary to fit our data. Often the parameters modified $\rho(v)$ very little before creating a physically unrealistic $V(r)$. The reason for this is that there are regions of $V(r)$ that our measurements are quite insensitive to—regions where the integrands in Eq. 2.39 are always highly oscillatory (like inside the core) or negligibly small (like at long range, $r \gtrsim 3r_e$).

A potential was needed that could be modified in the area where our measurements *are* sensitive—namely, in the shape of the minimum and its transition to the long range region. Such a potential was created by combining the modifications proposed by Duren and Groger [28] (used to model their differential cross section data), with the potential suggested by Forrey *et al.* [38] (a Morse potential smoothly matched to a damped Van der Waals attraction).

We start with the Forrey potential, which is a Morse potential,

$$V_{\text{Morse}}(r) = D_e\left[e^{-2\beta(\frac{r}{r_e}-1)} - 2e^{-\beta(\frac{r}{r_e}-1)}\right], \tag{2.40}$$

connected to a Van der Waals potential (Eq. 2.34) at a "cutoff" distance. We use the Duren modifications to take a Gaussian "bite" out of the Forrey potential between the minimum and the Van der Waals cutoff. Three parameters are used to describe the

size, location, and width of the bite. Besides the bite there are only three additional parameters: the Morse well depth, the distance scaling of the Morse potential, and the Van der Waals cutoff location. We do not allow the strength of the Van der Waals potential to vary since these coefficients are fairly well known for each of the systems. Of the six parameters total, we can obtain a reasonable fit to our data for *all* four Na-gas potentials with three of the parameters fixed (the Van der Waals cutoff, and the width and location of the bite), and three with very slight modifications (the well depth, the scaling of the Morse potential, and the size of the bite).

The shape of the minimum in the Morse potential is determined by the same parameter that defines the small r exponential repulsion. For agreement with our data we found it necessary to have a wide, flat minimum, which requires an abnormally weak core repulsion in the Morse potential. So to have a realistic potential we create a third region of the potential, cutting off the Morse potential below distances $r < r_0$ (where r_0 satisfies $V(r_0) = 0$) and replacing it with a realistic exponential repulsive region ($V(r) = Ae^{-br}$, where the constants A and b are fairly well known). Our measurements are completely insensitive to this third region; we do this only to create a potential that agrees with others in that region. Also included are small constant offsets to avoid discontinuities where the different regions of the potential meet. $V(r)$ may still appear somewhat artificial due to the discontinuities in the slope where different regions are matched. However, we keep these cusps in order to keep the form of the potential simple; they could be smoothed out though with no discernable difference in $\rho(v)$. The full algorithm for creating the potential is shown in Table 2.1.

To provide a good fit for all four systems, we have fixed the width (4 Bohr) and location (15 Bohr) of the Gaussian bite and fixed the Van der Waals cutoff at a location of about $3r_e$ (27 Bohr), allowing the other three parameters to vary for the different systems. A good fit with our data is found using the choices in Table 2.2. The potentials produced by these parameters and the corresponding comparison with the data are shown in Fig. 2-11 to 2-14. The shapes of the sodium-rare-gas potentials, scaled by D_e and r_e, are compared in Fig. 2-15.

```
function/d Vg(r,param1,param2,param3)
variable r,param1,param2,param3
    //all units are atomic units
variable eV=1/27.21,angstrom=1/.5292,inversecm=1.240e-4*eV
variable De=45.43*inversecm,re=4.991*angstrom,a=.4989,rc=10.2672*angstrom
    //parameters from Forrey97
variable c6=190,c8=12700,c10=820000
    //VdW coefficients are for Ar; multiply by 1.49 for Kr or 2.32 for Xe
variable v,r0
re= 10
    //set minimum at r=10
rc= 27
    //set VdW cutoff at r=27
r0= re-ln(2)/(a*param1)
    //r0 is the radius where Vmorse(r0)=0
v+= De*exp(-2*a*(r-re)) *(r<=r0)
    //repulsive part of potential (has no effect but makes it realistic)
v+= -De*exp(-2*a*(r0-re)) *(r<=r0)
    //a constant offset to match repulsive core to Morse
De*= param3
    //adjust well depth of Morse
v+= De*(  exp(-2*a*param1*(r-re)) - 2*exp(-a*param1*(r-re))  ) *(r>r0) *(r<=rc)
    //Morse part of potential
v+= -De*(  exp(-2*a*param1*(rc-re)) - 2*exp(-a*param1*(rc-re))  ) *(r<=rc)
    //offset to match Morse to VdW potential
v+= ( -c6/max(r,rc)^6 -c8/max(r,rc)^8 -c10/max(r,rc)^10 )
    //VdW part of potential (includes an offset for r<rc to match Morse potential)
v*= 1 - param2*exp(-(r-15)^2/4^2)
    //bite part of potential
return v
end
```

Table 2.1: The algorithm for creating the interatomic potentials in Figs. 2-11 through 2-14.

gas	param1 well curvature	param2 size of bite	param3 scaling of well depth
Ar	0.40	0.4	0.7
Kr	0.52	0.4	1.1
Xe	0.67	0.55	2.2
N_2	0.60	0	0.55

Table 2.2: Parameters used with the algorithm in Table 2.1 to generate the potentials in Figs. 2-11 through 2-14.

We can also compare the product $D_e r_e$ for our fit potentials with the D_e and r_e of various predictions. The value of D_e varies by about 10% among the predictions, and the value of r_e varies by about 5%. Compared to the parameters for the three sodium-rare-gas Lennard-Jones potentials in Ref. [17], the product $D_e r_e$ is smaller for our potentials by 38% for Ar, 38% for Kr, and 18% for Xe. This is outside of the typical variation among various predictions. This most likely results from the imperfections in the ad hoc nature of the shape of our potential $g(x)$ which can weakly affect the phase of the glory oscillations.

We can now address the question of where the various predictions of $V(r)$ go wrong. In comparison to our *ad hoc* potentials, the biggest difference is the need for a "bite" in the midrange—in other words, the predictions for the potential need to be significantly less attractive in the range $r_e < r < 2r_e$. This is an effect that can't be duplicated by the parameters of the other model potentials, so we conclude that the various damping functions in general do not do enough to correct for the divergence of the Van der Waals series.

Around r_e, we can also conclude that the various predictions do not allow for a flat enough minimum. Some predictions use the Morse potential, which can replicate this behavior as we have done, but this in itself is not sufficient, since by doing so it creates an unrealistically weak repulsive core. Furthermore, it is not just the flatness of the minimum that is important but also the slight extension of the attractive portion of the well into the core region, i.e. the location of the repulsive-to-attractive transition ($V(r_0) = 0$) must be at a slightly smaller radius r_0.

A striking result of these comparisons is that the four sodium-gas interactions can

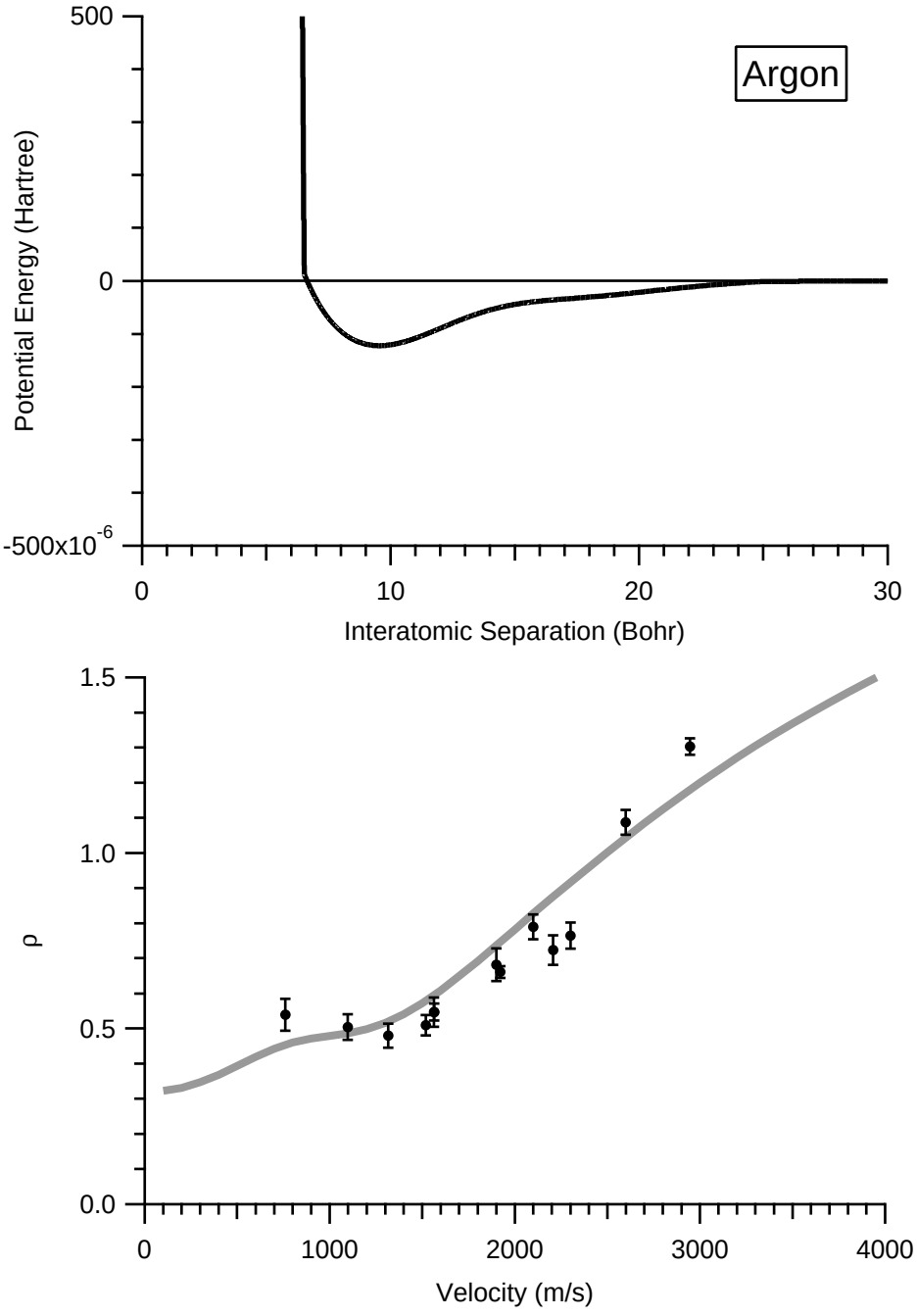

Figure 2-11: A model of the sodium-argon potential (top), and the corresponding function $\rho(v)$ in comparison with the data (bottom).

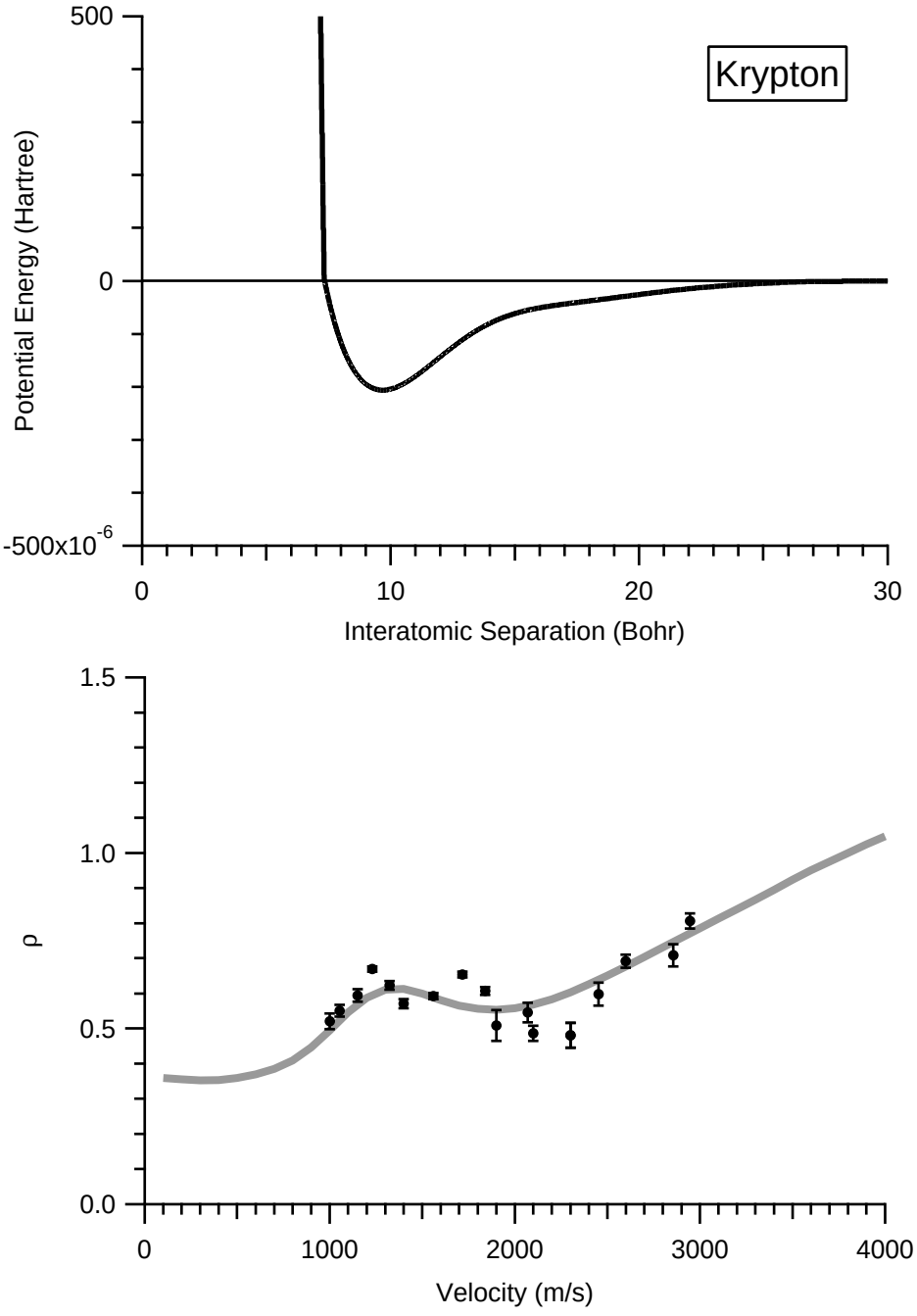

Figure 2-12: A model of the sodium-krypton potential (top), and the corresponding function $\rho(v)$ in comparison with the data (bottom).

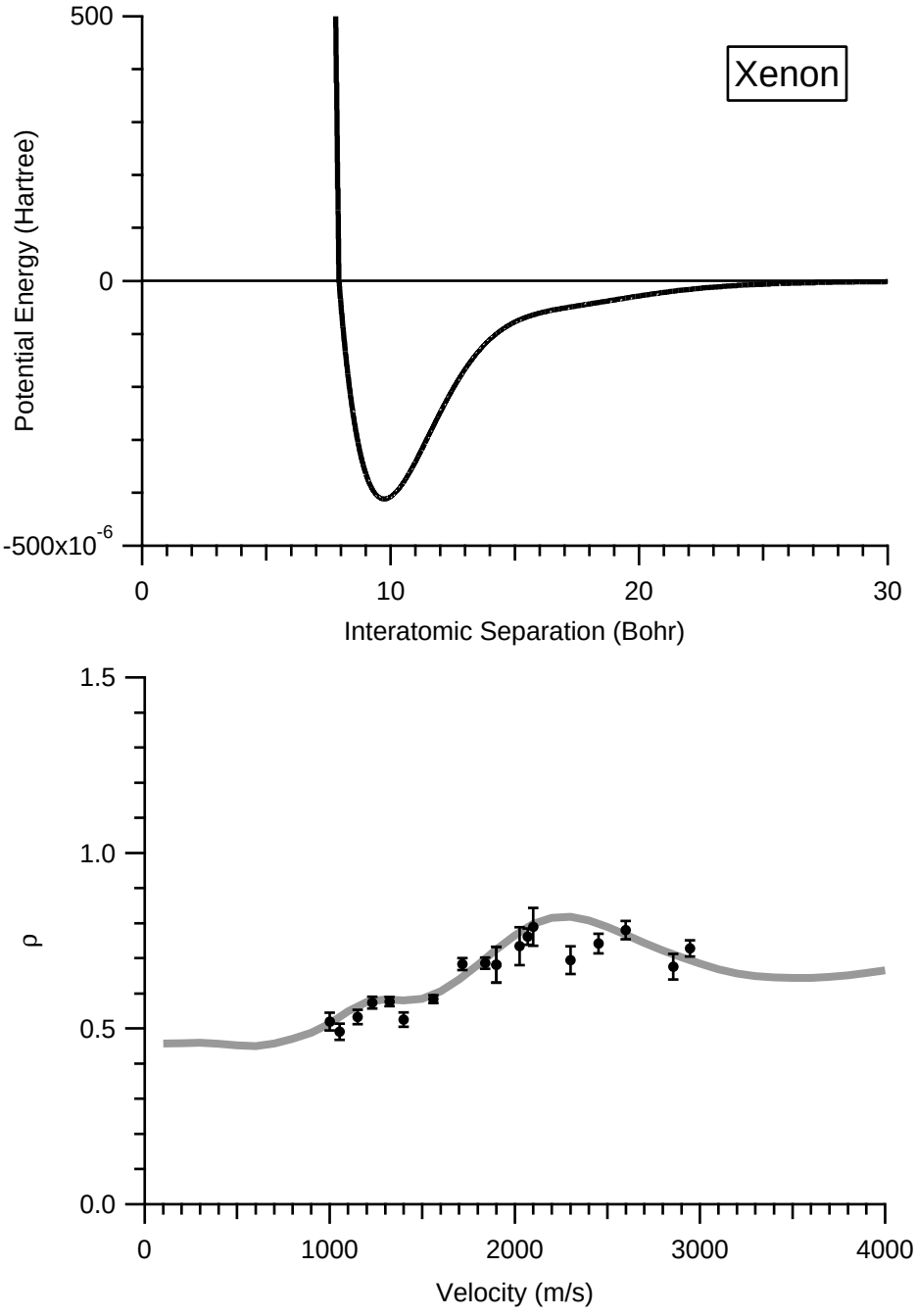

Figure 2-13: A model of the sodium-xenon potential (top), and the corresponding function $\rho(v)$ in comparison with the data (bottom).

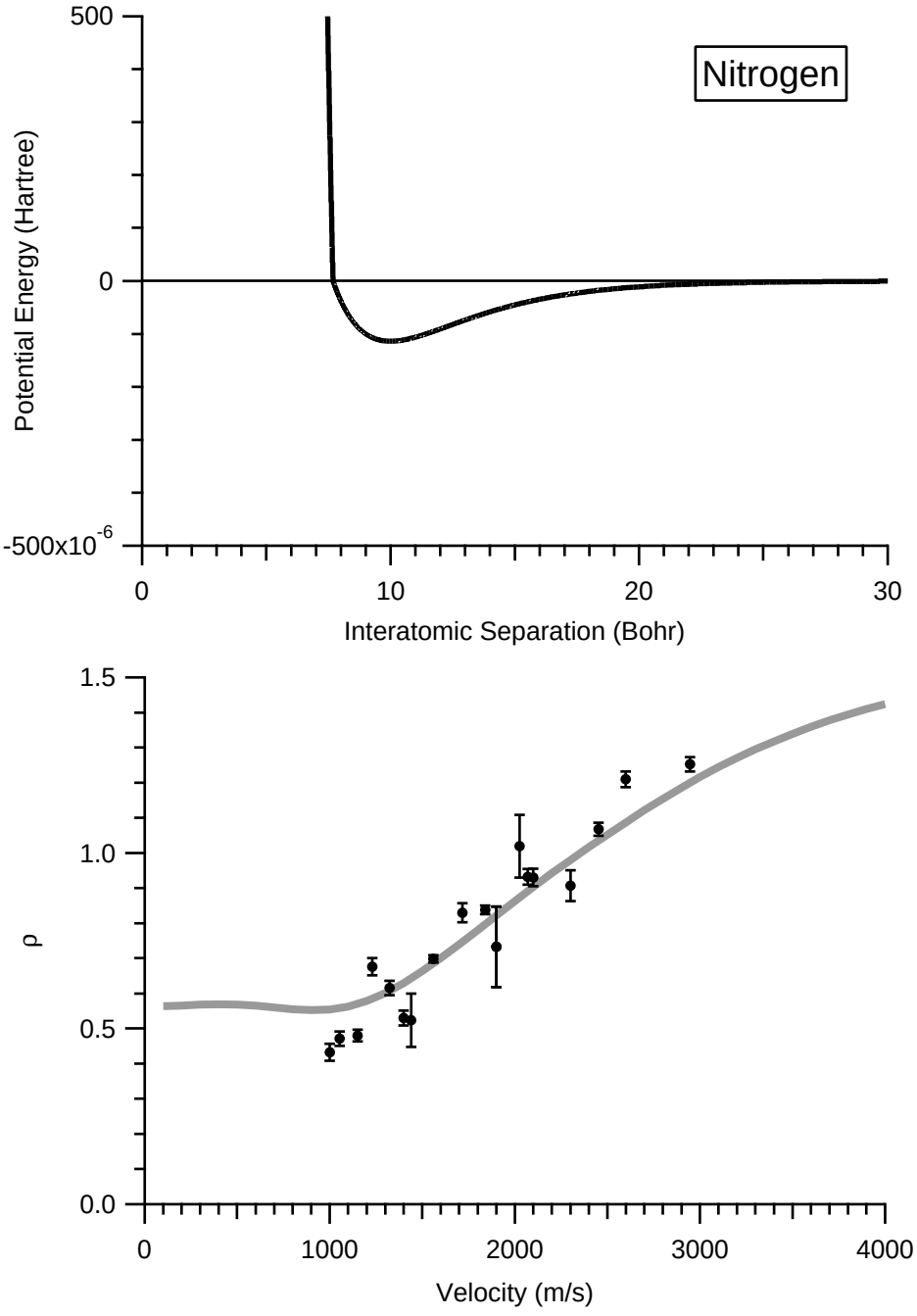

Figure 2-14: A model of the sodium-nitrogen potential (top), and the corresponding function $\rho(v)$ in comparison with the data (bottom).

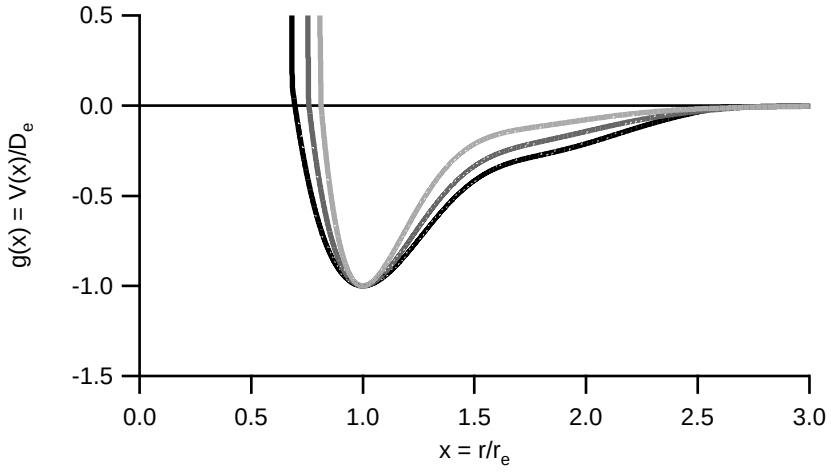

Figure 2-15: A comparison of shapes of the fit potentials in Fig. 2-11 to 2-13, for Ar (black), Kr (dark grey), and Xe (light grey). Each has been scaled by the depth D_e and location r_e of the minimum (Eq. 2.36).

seemingly be modeled by nearly the same potential, differing significantly only in the well depth. N_2 was in fact the most difficult to fit with this form, despite the data lying in a straight line. We might postulate that the sodium-rare-gas potentials are in fact quite similar except for their depth and the location of their minimum.

Because there is good agreement in the known values of D_e and r_e we can scale our measurements of $\rho(v)$ to verify this hypothesis. In Fig. 2-16 we have scaled our data, plotting all of the sodium-rare-gas measurements of ρ vs the parameter α using values of D_e and r_e taken from Ref. [17]. If the potentials all have the same shape $g(x)$ the data points should lie along the same curve. Of course, this neglects the effects of thermal averaging which would be 5% or less if the three systems had the same shape $g(x)$. Also included in the plot are data from the Na-Ne system taken with the old apparatus from Ref. [83], which are contained in Refs. [37, 8].

Scaled in this manner, the data show more than a full oscillation in the glory scattering. From the general overlapping of the data from different gases, we can conclude that the shape of the sodium-rare-gas potentials are all quite similar.

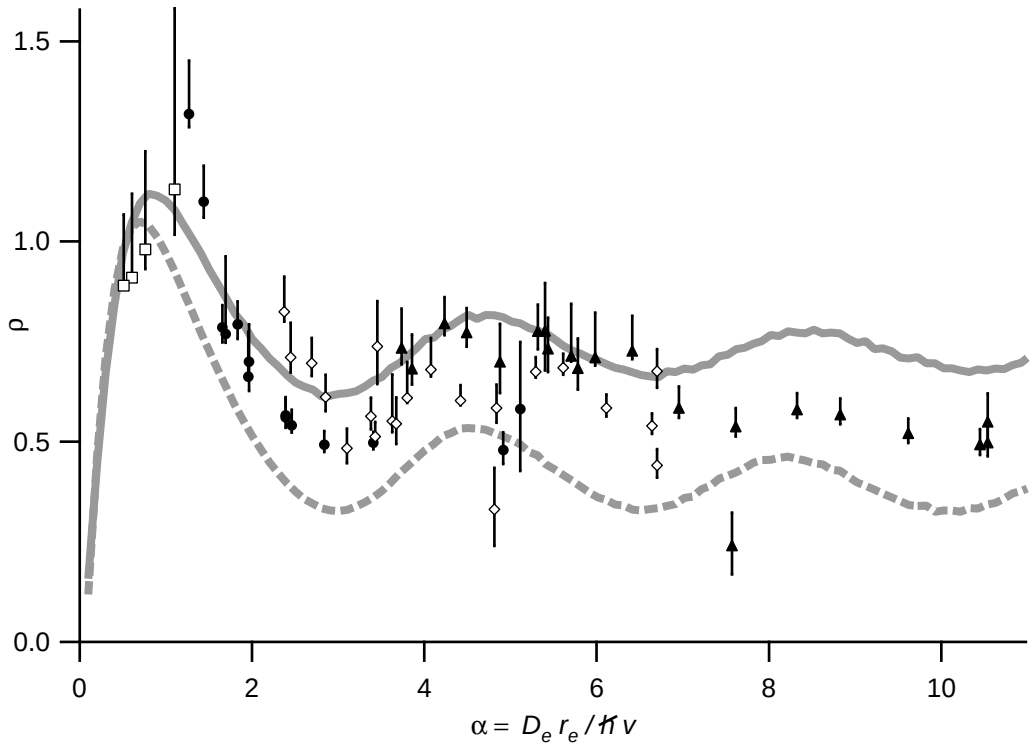

Figure 2-16: ρ for the Na-rare-gas systems, Na-Ne (□), Na-Ar (•), Na-Kr (◊), and Na-Xe (▲), plotted versus the dimensionless parameter $\alpha \equiv D_e r_e/\hbar v$. Also shown is the predicted ρ assuming a Lennard-Jones potential (—), and a Morse potential (– – –).

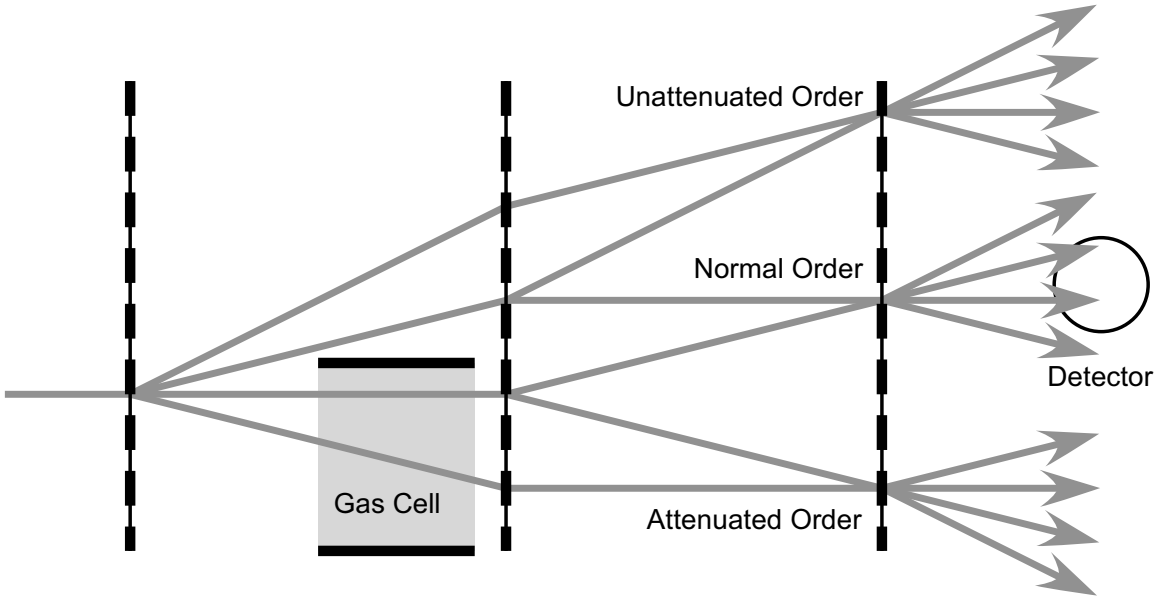

Figure 2-17: The various interfering orders that can be detected in the index of refraction measurement. The same three orders exist for molecules in the beam, but the diffraction angles are smaller by $\frac{1}{2}$.

2.12 Systematic Errors

2.12.1 Other Interfering Orders, Including Molecules

Systematic errors in this experiment were considered in detail in Ref. [56]. We revisit this topic with a more in-depth look at some of these errors and examine a few new ones.

The existence of other paths in the interferometer that can interfere at the detector is by far the largest systematic affecting our index of refraction measurements. To better account for this effect, we must model the intensity and shape of the different interfering pathways in the detector plane.

The profile of each interfering order is trapezoidal with a shape determined by the width and location of the beam collimation slits. The smallest slits were used almost exclusively in this experiment (except for the lowest velocity data points of the 200 nm Ar and 100 nm Ar, Kr, Xe, N_2 data). The slits were 11.5 μm and 16 μm wide, located 333 cm and 246 cm from the detector.

We need to calculate the intensity of other interfering pathways reaching the detector. The intensity is proportional to the product of the amplitudes of the two paths that are interfering. We represent the amplitude of one path with the notation ψ_{012}, which represents the plane wave that gets diffracted into the 0^{th} diffractive order by the first grating, the 1^{st} diffractive order by second grating, and the 2^{nd} diffractive order by last grating.

The other interferometers that we need to be concerned about are:

$\psi_{0\,1\,(n-1)}\,\psi_{1\,-1\,n}$	"normal" interference pattern (one path inside gas cell, one outside)
$\psi_{1\,1\,(n-1)}\,\psi_{2\,-1\,n}$	"unattenuated" interference pattern (both paths outside gas cell)
$\psi_{-1\,1\,(n-1)}\,\psi_{0\,-1\,n}$	"attenuated" interference pattern (both paths inside gas cell)

The same three interfering pathways occur for the molecules in the beam also, but the angles and separations are half that for the atoms. The variable n acknowledges the fact that two paths inside the interferometer can interfere at several locations in the detector plane due to diffraction by the third grating. Though the interfering orders with large n are greatly reduced in intensity, it is important to consider paths up to at least $n = \pm 4$ because they will be detected in spite of careful positioning of the detector.

The amplitude of the plane wave diffracted into the n^{th} diffractive order from a single grating is

$$A_n = f\text{sinc}(n\pi f) \tag{2.41}$$

where f is the open fraction of the grating. The intensity of an interfering order is the product of the diffraction amplitudes of each path for each order from each grating:

$$\begin{aligned}\psi_{m\,1\,(n-1)}\,\psi_{(m+1)\,-1\,n} = {} & I_0\, f_1^2\,\text{sinc}[m\pi f_1]\,\text{sinc}[(m+1)\pi f_1] \\ & \times f_2^2\,\text{sinc}^2[\pi f_2] \\ & \times f_3^2\,\text{sinc}[(n-1)\pi f_3]\,\text{sinc}[n\pi f_3]\end{aligned} \tag{2.42}$$

where I_0 is the intensity of the beam in the absence of the gratings (neglecting the

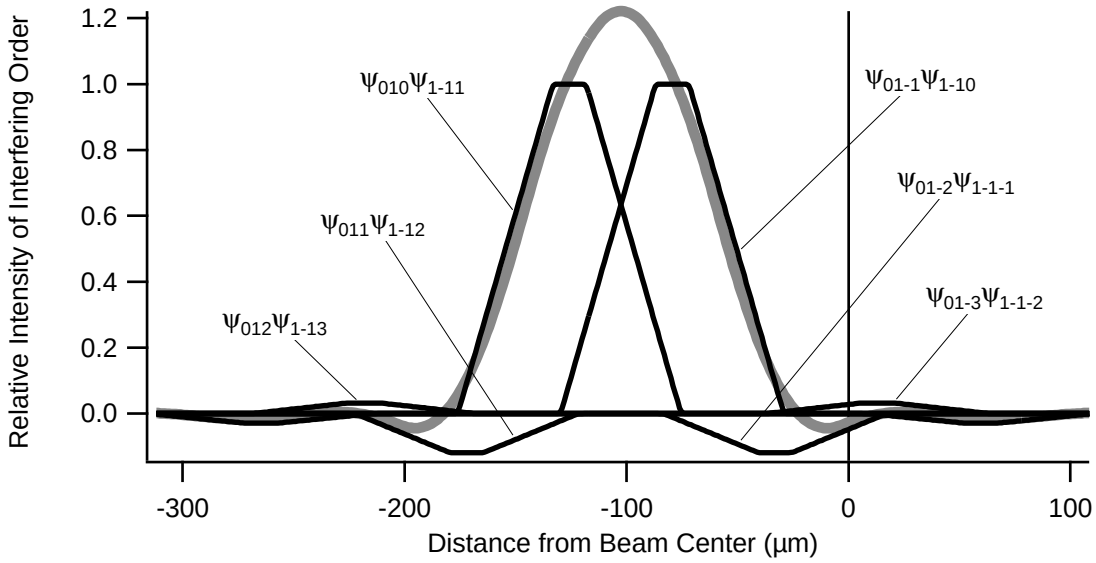

Figure 2-18: The intensity of interfering orders that make up the "normal" interference pattern (black). Also shown is the total detected interference intensity as a function of detector position (grey); it is the sum of all orders convolved over the 50 μm width of the detector. This example is for our 200 nm interferometer ($f_1 = 0.67$, f_3=0.57) at $v = 1$ km/s.

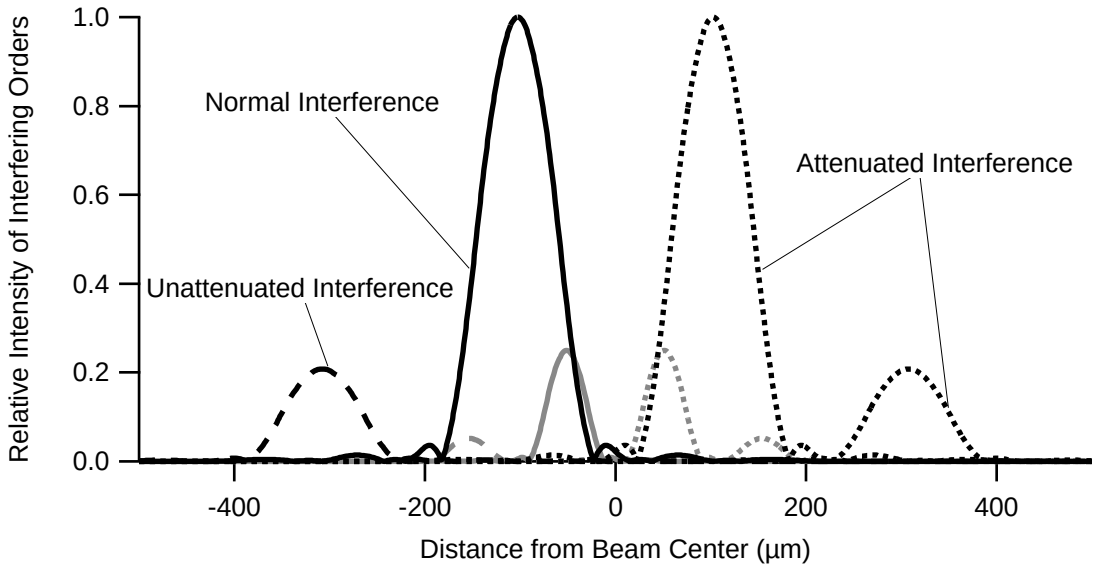

Figure 2-19: Relative intensities of "wrong" interfering orders compared to the "normal" order, as measured by the detector. The normal order (—) is the same as the grey curve in Fig. 2-18. The unattenuated order ($\cdots$) passes entirely outside of the gas cell, and the attenuated orders (- - -) pass though the gas cell. Also shown are the same interfering orders from the sodium molecules in the beam (grey).

flux lost to the grating support structure which reduces the intensity by 15–25%). Eq. 2.42, with all possible n and m, accounts for all of the interfering orders that will be *detected*. There are other diffracted paths that can interfere, but they are either not "white fringe" interference (i.e. having a velocity dependent phase that gets washed out) like the interference of $\psi_{000}\psi_{1-21}$, or they have higher period fringes like the diamond-shaped interferometer $\psi_{-12-1}\psi_{1-21}$.[1] Since $\mathrm{sinc}(x)$ can be positive or negative, the intensity of some interfering orders will be *negative*, meaning that the intensity will contribute 180° out of phase with the interference pattern. Fig. 2-18 shows the interfering orders that contribute to the profile of the "normal" interfering order, all the "wrong" interfering orders are similar in shape. Fig. 2-19 shows the intensity and location of this profile relative to the wrong orders (assuming a 20% molecule fraction in the intensity).

To accurately calculate the contamination by the wrong orders, we must also account for the cropping of each order by the gas cell. This is extremely important for the normal-molecule order because its maximum lies so closely on the detector and creates a huge uncorrectable error since ρ for Na_2 is completely unknown. Thankfully, a cataloging of all the septum widths as measured on each of the nights we took data shows that the septum was always wider than the molecule path separation, making molecule interference impossible. For our earliest measurements, we were simply lucky in this regard. Later, after we became aware of this source of error, we prevented it by deliberately misaligning the the septum (to an average effective septum width of 40 μm) to make it block all the molecules.[2]

Cropping was modeled assuming the septum acts as a straight-edge in the far field of the slit collimation. Fig. 2-20 shows the intensities of the attenuated/unattenuated atom/molecule interference relative to the normal interference. The example shown is for the worst case of infringement by the wrong orders—using a 2 km/s beam with 200 nm gratings. The problem is caused by both the closeness of the orders at this

[1] The presence of these higher period fringes means that the interference pattern we measure is not actually a sine wave, depending upon how much of these higher order components are present.

[2] The 1993 measurement did not consider this error and as a result as much as 20% of the detected interfering intensity was due to molecules.

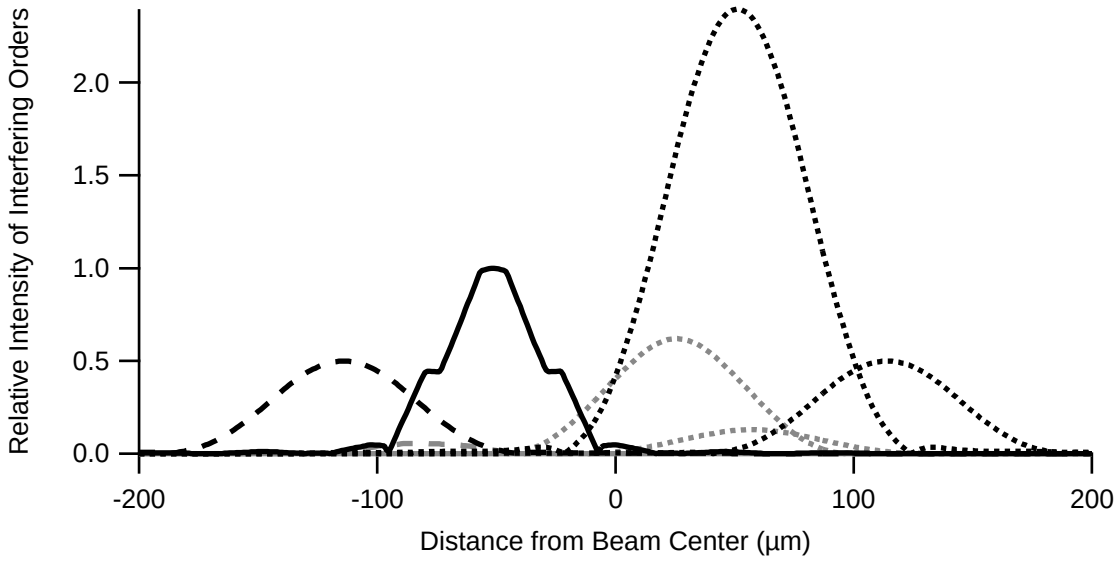

Figure 2-20: Intensities of "wrong" interfering orders ($\cdots$), (- - -) compared to the "normal" order (—), this time including the effects of clipping by the septum (molecule orders are in grey). This example models the worst case of contamination experienced during our measurements: $v = 1$ km/s, 200 nm gratings. The "normal" intensity is greatly reduced due to clipping by the septum.

velocity, and the attenuation of the normal order because its paths are clipped by both sides of the septum.

Fig. 2-21 shows the fraction of intensities of the wrong orders hitting the detector as a function of velocity. It doesn't matter whether the unattenuated orders are from molecules or atoms, so they are combined into one percentage. Similarly for the attenuated orders—we don't know the constant of attenuation $\eta_{\text{molecules}}$, but a good estimate is $\eta_{\text{molecules}} = \eta_{\text{atoms}}$ [56], so we can combine the attenuated orders into a single percentage as well. Fig. 2-21 has also taken into account possible uncertainty in the detector position due to initial misalignment or thermal drift, estimated at ± 20 μm.[3] The curves shown are the maximum percentage of contaminating orders found within ± 20 μm of the position we tried to align the detector to.

Once we known the fractional intensity of the contaminating orders, we can

[3]The ± 20 μm position uncertainty is primarily due to thermal drift, which was estimated by comparing how the position of the 0^{th} beam drifted during a night's worth of data.

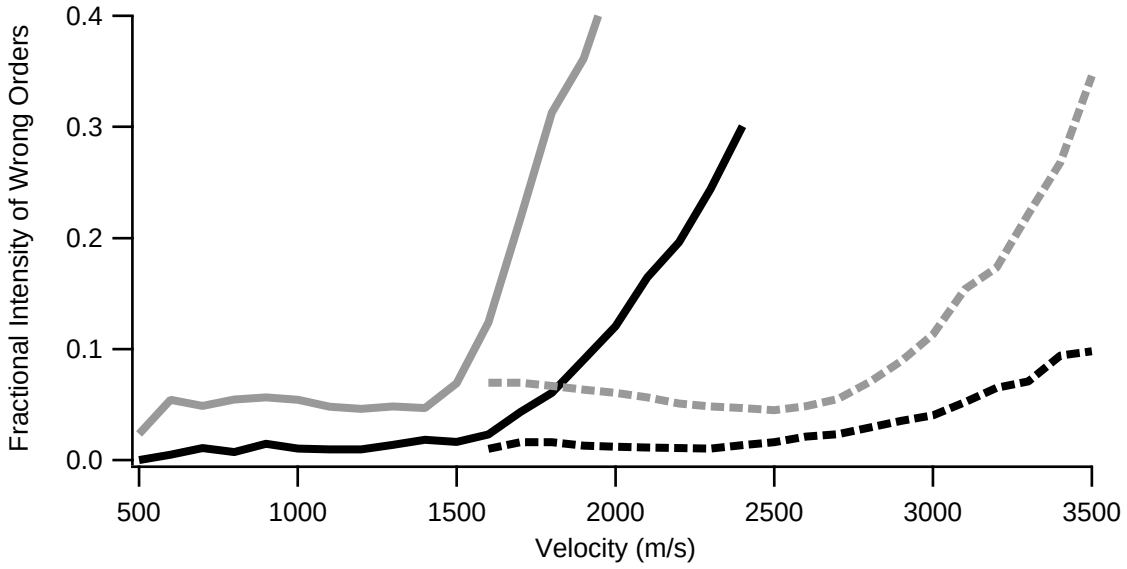

Figure 2-21: The fractional intensity of the wrong orders hitting the detector as a function of the interferometer velocity, using 200 nm (—) and 100 nm (- - -) gratings. The curves are for the unattenuated (black) and attenuated (grey) orders, and include the sum of intensities for both atoms and molecules.

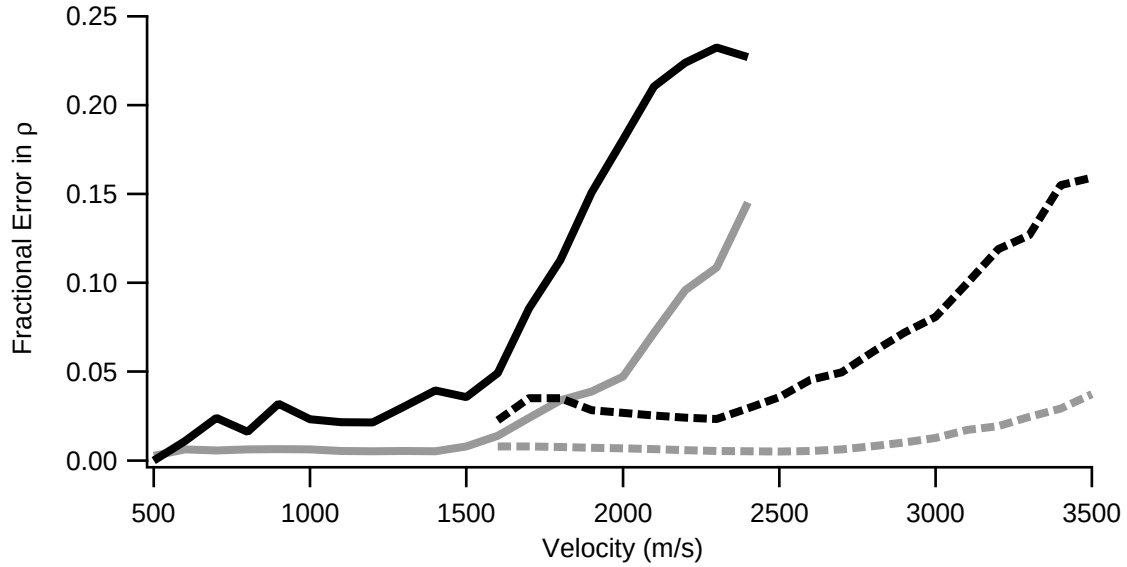

Figure 2-22: The fractional systematic error in the measurement of ρ due to wrong interfering orders, as a function of velocity for the 200 nm (—) and 100 nm (- - -) interferometers. Although the attenuated orders (black) are larger than the unattenuated ones (grey) to start with (see Fig. 2-21), they influence the measurement of ρ less because during the measurement they are greatly attenuated.

estimate the error in measuring ρ. Fig. 2-22 shows the fractional error $(\rho_{\text{true}} - \rho_{\text{measured}})/\rho_{\text{true}}$ due to unwanted interference. For simplicity, we have assumed typical parameters of $\rho_{\text{true}} = 0.75$ and $\eta = 1.5$. Varying these parameters doesn't significantly change the error estimate. For both the 100 nm and 200 nm interferometers, there is a critical velocity above which all the interfering orders overlap and the error grows dramatically. Note that the error in ρ is always *positive*. This means that our measurement of ρ is always a little *lower* than ρ_{true}.

2.12.2 Other Systematic Errors

Impure Target Gas

The low velocity Ar data presented here suffer from the presence of a small air leak that was present during some of the early data acquisition. This problem was fully described in Ref. [56], which estimated the error due to the leak (0–5%) for each of the affected data points.

Since those measurements we have been careful to check for leaks during each night of data. We do this by making a ratio measurement with the reservoir empty. A leak would put air either in the reservoir or the gas inlet line and show up as an attenuation of the fringes. These tests never showed a recurrence of the leak.

Attenuation of the Path Traveling Outside the Gas Cell

This error arises due to the imperfect nature of the gas cell, namely, that when exposing the inside path to the gas, some gas escapes through the ends of the cell and slightly attenuates the outside path. We characterize this by the ratio of attenuation $\epsilon \equiv \eta_{\text{outside}}/\eta_{\text{inside}}$. If not accounted for, the extra attenuation will give a mismeasurement of the ratio: $(\rho_{\text{true}} - \rho_{\text{measured}})/\rho_{\text{true}} = 2\epsilon$ for $\epsilon \ll 1$ [56]. The factor of two arises because the outside gas increases the attenuation of the fringe by a factor $(1+\epsilon)$ but decreases the phase shift by $(1-\epsilon)$.

To measure ϵ, we have followed the same procedure as in [56]. We measured the the attenuation of the beam inside and outside the cell at different pressures, with the

result: $\eta_{\text{outside}}/\eta_{\text{inside}} = 8.2(7) \times 10^{-3}$. However, this procedure neglects the presence of molecules in the beam which change the pressure dependence of η. The uncertainty of the molecule attenuation, estimated at $\eta_{\text{molecules}} = (1.5 \pm 0.5)\eta_{\text{atoms}}$, increases the uncertainty in the measured ϵ:

$$\epsilon = 8.2(1.4) \times 10^{-3}. \tag{2.43}$$

The bottom line is that we correct for this systematic by multiplying ρ_{measured} by a factor $(1 - 2\epsilon) = 0.9836$, and there remains a $\pm 0.3\%$ systematic error in ρ due to our uncertainty in ϵ. This is negligible compared to the error of unwanted interfering orders.

Gas Cell Filling and Emptying

The gas cell can be filled or emptied in just a few seconds. The quicker we alternate between a full cell and an empty one, the better we measure the phase difference between the two situations, since the phase is always drifting due to mechanical vibrations and thermal expansion. To shrink the fill-evacuate cycle time as short as possible, we collect some of the fringe data while the gas pressure is still coming to equilibrium. (In fact we collect data throughout the entire cycle, but in post-analysis the first three seconds of data taken during filling or emptying are thrown out.) There is a systematic error that arises because even after 3 sec the cell has not quite reached its equilibrium pressure. We end up fitting to a slightly time-averaged interference pattern rather than one taken at a fixed pressure.

The conclusion stated in Ref. [56] based on an analysis of this effect was that the error is negligible, because after waiting 3 sec the gas cell pressure is almost at equilibrium and because ρ doesn't depend on pressure even though η and ϕ do. One problem with that analysis is that it assumes the time-dependence of the amplitude and phase is the only thing affecting the *fit* for determining the amplitude and phase. Unfortunately, the average count rate (the offset of the fringe) also has a time-dependence, and it is large enough to hamper the fringe fit-routine. To illustrate, when filling, the

pressure in the cell has an exponential dependence

$$P(t) = P_0\Big[1 - e^{-t/\tau}\Big], \tag{2.44}$$

where τ is the time constant for filling. The attenuation constant has a linear dependence on pressure, so the fringe amplitude varies as

$$A(t) = A_0 \exp[-\eta(1 - e^{-t/\tau})], \tag{2.45}$$

and the average intensity varies as

$$N(t) = N_0 + N_1 \exp[-2\eta(1 - e^{-t/\tau})], \tag{2.46}$$

where η is the equilibrium attenuation constant. Assuming typical parameters, a fringe contrast $A(0)/N(0) = 5\%$ with an empty cell, a time constant $\tau = 2$ sec for filling the cell, and an equilibrium value of $\eta = 2$, then even after 10 seconds N still differs from its equilibrium value by an amount larger than A. Any change in the count rate larger than the size of the interference amplitude is bound to create significant errors in the fringe fit routine—e.g. the fit routine will preferentially fit the trough of the fringe to the place where the average count rate is lowest, and the peak of the fringe to where it is highest. Only the data taken when the cell is being filled need to be corrected for this problem—scans taken when evacuating the cell are at sufficient equilibrium after 3 sec.

We fix this problem by subtracting the time-dependent average count rate from the interference pattern before fitting it. To find the average count rate, we average all of the count-rate-vs-time files for each set of data and fit the result using Eq. 2.46. We found that Eq. 2.46 modeled $N(t)$ very well for all datasets, though interestingly the time constant τ depended on the gas used (Table 2.3).

After subtracting the time-dependent count rate from the interference pattern, we can then fit for ϕ and η. The remaining systematic error is then calculated using the procedure in Ref. [56], using Eq. 2.44 to predict the time-dependence. The remaining

Gas	Gas Cell Time Constant, τ	Remaining Systematic Error in ρ after Correction
Ar	1.2 sec	0.09%
Kr	1.7 sec	0.26%
Xe	2.1 sec	0.53%
N_2	1.1 sec	0.06%

Table 2.3: Total fractional systematic error in ρ due to the time dependence of the pressure in the gas cell, during both filling and evacuating.

error ranges from 0.1–0.5% depending on the gas used (Table 2.3). This error is included in the systematic error bars for ρ in Figs. 2-7 through 2-10.

Conclusion

Error bars on the new data points in Figs. 2-7 through 2-10 include the sum of statistical and systematic errors. The average size of the statistical-plus-systematic error bars is 9% of ρ. The systematic error due to "wrong" interfering orders is the only non-negligible systematic error (apart from some of the Ar data affected by a leak) contributing to those error bars.

Because the only non-negligible systematic comes from interfering orders that are erroneously detected due to beam alignment and drift, we have an independent check of this error by examining the repeatability of data taken on different nights. We expect that the error in alignment or drift may exceed our estimates on some nights, but this can be recognized: ρ will be artificially low compared to other nights, we will see this deviation in all the gases measured, and the measurement will have larger statistical error bars as the ratio changes due to drift. An example of these features can be seen in the severely outlying data points measured at 1450 m/s for Kr, Xe, and N_2.

Another indication of this systematic error would be a dependence of ρ on the pressure at which the index of refraction is measured. The reduced χ^2 for the average of ρ from two or more sets of data taken at different pressures is 0.64 on average. The fact that χ^2 is not greater than one suggests that there is not a correlation between ρ and the pressure at which it is measured—such a correlation would be an indication of

any kind of possible pressure-dependent systematic error. The χ^2 also indicates that on average the systematic error due to thermal drift is not greater than the statistical error, since if the thermal drift was large, data taken at different times during the night would give slightly different values of ρ.

Another check of systematics can be made by comparing the 100 and 200 nm data where they overlap. At this velocity, unwanted interference is seven times larger for the 200 nm data than for the 100 nm data, yet the agreement between the two is well within the error estimates, suggesting that our worst case scenario overestimates the effects of the undesired interfering pathways.

Chapter 3

Measuring Polarizability with an Atom Interferometer

3.1 Introduction

The MIT atom interferometer was previously used to perform the most precise measurement of sodium's polarizability [34]. The measurement was limited by the spread of velocities in the atomic beam. We present a new technique which has evolved from earlier ideas [48] that described how atomic beam choppers can be used to overcome the limitations of that experiment, though at a substantial loss in signal-to-noise. In this chapter we will generalize the ideas of atomic beam choppers to the quantum regime, showing how a new pulsed-phase-shift technique has evolved from those ideas, and how it can push polarizability measurements to far greater precision.

The MIT measurement of polarizability was performed with a precision of 0.4% [34]. The precision was limited by three factors:

1. The electric field produces a velocity-dependent phase shift of the interference pattern. The atomic beam has a spread of velocities resulting in a washed-out interference pattern at high electric fields.

2. Uncertainties in the mean velocity and the detected velocity distribution introduce systematic errors.

3. The geometry of the electric field region has limited precision.

The new rephasing technique completely eliminates the obstacles imposed by limitations 1 and 2. Limitation 3 can be overcome using some improvements discussed in later in the chapter. Alternatively, it can be eliminated from consideration by making a relative measurement of the polarizabilities of two atoms—although each individual measurement is in error due to geometrical uncertainties, the ratio of polarizabilities is exact.

3.2 Evolution of the Rephasing Technique for Measuring Polarizability

3.2.1 The Problem: Interference Fringe Dephasing

Polarizability is measured in an atom interferometer by applying a region of constant electric field on one of the paths, introducing a relative phase shift between the paths, and a change in the phase of the interference pattern. The phase depends not only on the strength of the electric field but also on the transit time through the region, consequently, the phase depends on the velocity of the atom as well. If the phase of the slowest atoms differs from that of the fastest atoms by more than a few radians, the interference pattern is washed out. We will quantify this contrast loss.

The interference pattern we measure is usually independent of velocity of the atoms in the beam. We see a count rate that varies with the "reference" phase of the interferometer as

$$I(\phi_0) = N + A\cos\phi_0, \tag{3.1}$$

where the reference phase

$$\phi_0 \equiv k(x_1 - 2x_2 + x_3) \tag{3.2}$$

depends on the position of the gratings.

The energy of an atom in an electric field is $U = \alpha E^2/2$, where E is the magnitude of the electric field and α is the polarizability. To measure α, we introduce an electric

field on one path of the interferometer, which shifts the phase of the interference pattern by an amount $Ut/\hbar$, where t is the time spent in the the field. Because the transit time depends on the inverse-velocity, the phase shift does too:

$$\phi_{\rm elec}(v) = \frac{\alpha}{2}\Big(\frac{V}{d}\Big)^2 \frac{\ell}{\hbar v} \equiv 2\pi v_{\rm ref}/v \tag{3.3}$$

where V, ℓ, and d are the voltage, length, and plate separation for a constant electric field interaction region. To simplify the notation, we have introduced the variable

$$v_{\rm ref} \equiv \frac{\alpha}{2}\Big(\frac{V}{d}\Big)^2 \frac{\ell}{h}, \tag{3.4}$$

which can be thought of as the beam velocity that sees a phase shift of exactly 2π in the interaction region.

Average over the observed fringes of the velocity-dependent interference pattern reduces the contrast:

$$\begin{aligned} I = \int P(v)I(v)dv =& N + A\int \frac{1}{\sqrt{2\pi\sigma_v^2}}\, e^{-\frac{1}{2}(v-v_0)^2/\sigma_v^2}\, \cos[\phi_0 + 2\pi v_{\rm ref}/v]dv \\ =& N + AC'\cos\phi' \end{aligned} \tag{3.5}$$

where

$$\begin{aligned} \phi' =& \phi_0 + 2\pi v_{\rm ref}/v_0 \qquad\qquad \text{and} \\ C' =& \exp\Big[-\frac{1}{2}\Big(\frac{2\pi v_{\rm ref}\sigma_v}{v_0^2}\Big)^2\Big], \end{aligned} \tag{3.6}$$

and we have assumed the probability distribution $P(v)$ is Gaussian with average velocity v_0, rms velocity σ_v, and $\sigma_v \ll v_0$.

The result is that the contrast C' falls off dramatically when the interaction phase is large ($v_{\rm ref} \gg v_0$). To measure polarizability, we cannot surpass an interaction phase of about $\phi_{\rm elec}(v_0) \approx 2\pi v_0/\sigma$ without drastically loosing signal-to-noise. Since the measurement is limited by how well we can statistically determine the phase of the interference pattern, $\Delta\phi$, we are limited in the precision with which we can determine

the polarizability: $\Delta\alpha/\alpha = \Delta\phi/\phi_{\rm int}(v_0)$.

3.2.2 Rephased Interference with Beam Choppers

Atomic beam choppers can be used to prevent contrast loss due to the velocity spread. Beam choppers, typically implemented using spinning slotted disks, act as shutters that open and close at a fixed frequency f. Two of these choppers placed a distance L apart change the velocity distribution of the beam—atoms with velocities fL/n for integer n can get through both choppers, and atoms with velocities $fL/(n+\frac{1}{2})$ cannot (Fig. 3-1). For the atoms that do get through, we can make sure they all contribute in phase to the interference pattern. By adjusting the frequency f we can adjust the spacing of the peaks in the velocity distribution, so that the phase picked up in the electric field region differs by a multiple of 2π for each peak. We will calculate how well the interference pattern can be rephased by this method.

Transmission of Beam Choppers

If we chop the intensity of the beam with mechanical choppers, we can create a new velocity distribution, since the transmission through the choppers depends on velocity. We will calculate this transmission, $T(v)$. Suppose the intensity transmitted by a single chopper is periodic with frequency $f \equiv \omega/2\pi$. Then we can write the transmission as:

$$a(t) = \sum_{n=0}^{\infty} a_n \cos(n\omega t) \qquad \text{where} \quad 0 < a(t) < 1 \tag{3.7}$$

For a square wave chopper, $a_0 = p$ and $a_n = \frac{2}{n\pi}\sin(n\pi p)$ where p is the fraction of time the chopper is open.

For two choppers separated by a distance L, the total transmission through the choppers now depends on the velocity of the beam:

$$T(t,v) = a(t)a(t+L/v) = \sum_{n,m} a_n a_m \cos[n\omega t]\cos[m\omega(t+L/v)] \tag{3.8}$$

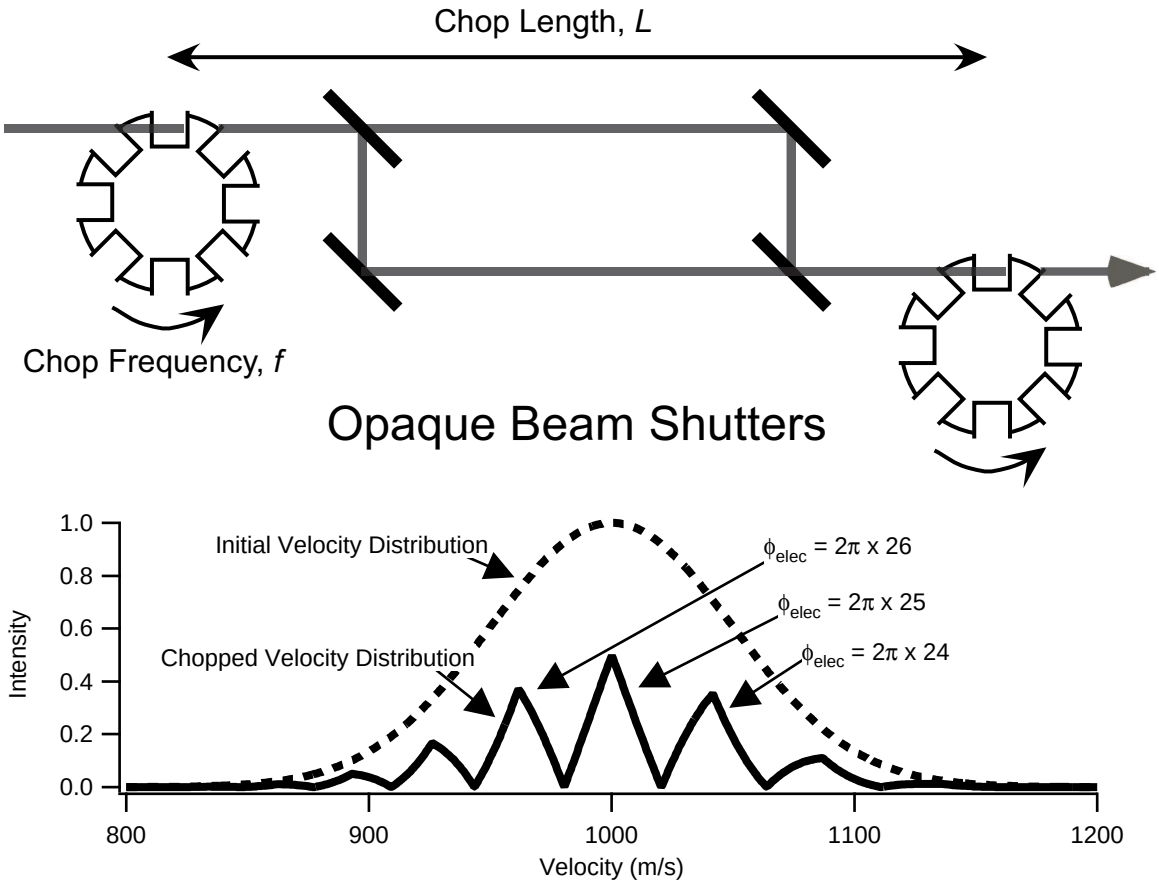

Figure 3-1: A schematic of mechanical beam choppers and the resulting velocity distribution. If an electric field is applied to one path, the frequency can be adjusted so that the phase picked up by neighboring peaks in the velocity distribution differs by exactly 2π, rephasing the interference pattern. The initial distribution is Gaussian with a mean of 1000 m/s and 5% rms spread. The chopped distribution uses 50% duty cycle choppers with $L = 1$ m and a $f = 25$ kHz (Eq. 3.9).

We are only interested in the time-averaged transmission:

$$\begin{aligned} T(v) &= \Big\langle T(t,v) \Big\rangle_t = \Big\langle \sum_n a_n^2 \cos^2[n\omega t] \cos[n\omega L/v] \Big\rangle_t \\ &= a_0^2 + \sum_{n=1}^{\infty} \frac{1}{2} a_n^2 \cos[n\omega L/v]. \end{aligned} \tag{3.9}$$

Rephased Contrast of Beam Choppers

Chopping the beam creates a new velocity distribution $P'(v) = P(v)T(v)$ where $P(v)$ is the initial Gaussian distribution and $T(v)$ is the transmission of the choppers. The new distribution will no longer have the same exponential contrast loss when the "polarizability phase" is applied by turning on the electric field interaction region. As before, the detected interference pattern is an average over the fringes having different phases depending on velocity:

$$\begin{aligned} I = \int P'(v) I(v) dv = \int P(v)\, a_0^2 \left(N + A\cos[\phi_0 + 2\pi v_{\text{ref}}/v]\right) dv \\ + \sum_{n=1}^{\infty} \int P(v)\, \frac{a_n^2}{2} \cos[n\omega L/v] \left(N + A\cos[\phi_0 + 2\pi v_{\text{ref}}/v]\right) dv \end{aligned} \tag{3.10}$$

If $v_{\text{ref}} \gg v_0$, the first term averages to $a_0^2 N$—we get no contribution to the interference from this term because the contrast is exponentially small. We can also assume that subsequent terms will vanish as well unless $2\pi v_{\text{ref}} \approx n\omega L$. If we choose the chopping frequency such that

$$\omega = 2\pi v_{\text{ref}}/L \tag{3.11}$$

then the only surviving contributions to the interference pattern will be

$$I = a_0^2 N + \frac{a_1^2}{2} A \int P(v)\, \cos[\omega L/v]\, \cos[\phi_0 + \omega L/v] dv \tag{3.12}$$

If the function $P(v)$ varies smoothly with v compared to the function $\cos(\omega L/v)$, then the term $\cos[\omega L/v]\cos[\phi_0 + \omega L/v]$ averages to $\frac{1}{2}\cos\phi_0$:

$$I = a_0^2 N + \frac{a_1^2}{4} A \cos\phi_0 \tag{3.13}$$

For a square wave we have

$$I = N' + A' \cos \phi_0 \tag{3.14}$$

with intensity $N' = p^2 N$ and contrast $(A'/N') = (A/N)\mathrm{sinc}^2(\pi p)$ (p is the duty cycle).

The resulting interference pattern is rephased, but at a loss of both intensity and contrast compared to the original interference pattern. The signal-to-noise ratio for the fringe measurement is proportional to $A\sqrt{N}$ (see Appendix E). For a 50% duty cycle, the intensity is down by a factor $\frac{1}{4}$ and the contrast is down by 0.405, so the signal-to-noise ratio is down by 0.203. The best signal-to-noise occurs at $p = 0.371$, where it is down by a factor 0.231.

3.2.3 Rephased Interference with Phase Choppers

Phase choppers are similar to mechanical choppers but instead of modulating the intensity of the beam in two locations, we modulate the phase of the interferometer. Modulating the phase of the interference pattern between 0 and π is like modulating the intensity of the sine-wave fringe between positive and negative amplitude (compared to the mechanical choppers which modulated the intensity between positive amplitude and zero). The resulting rephased fringe will have a much-improved signal-to-noise level, since the phase choppers do not remove atoms from the beam.

We will calculate the intensity and contrast of the rephased interference pattern using phase choppers. Consider square wave phase choppers with a 50% duty cycle that each apply a π phase shift to the interferometer when they are on, and zero phase shift when they are off. We can treat the phase choppers in the same manner as beam choppers if we identify four different classes of atoms that pass through the interferometer—those that pass through the choppers in each combination of states ($1^{\mathrm{st}}$and 2^{nd}choppers either on or off). The choppers have no affect on the intensity of the beam, but each individual class of atoms can be treated as if it is being chopped out—intensity lost to one class of atoms (when the phase applied by the chopper changes) will be gained by another. We now have four different velocity distributions

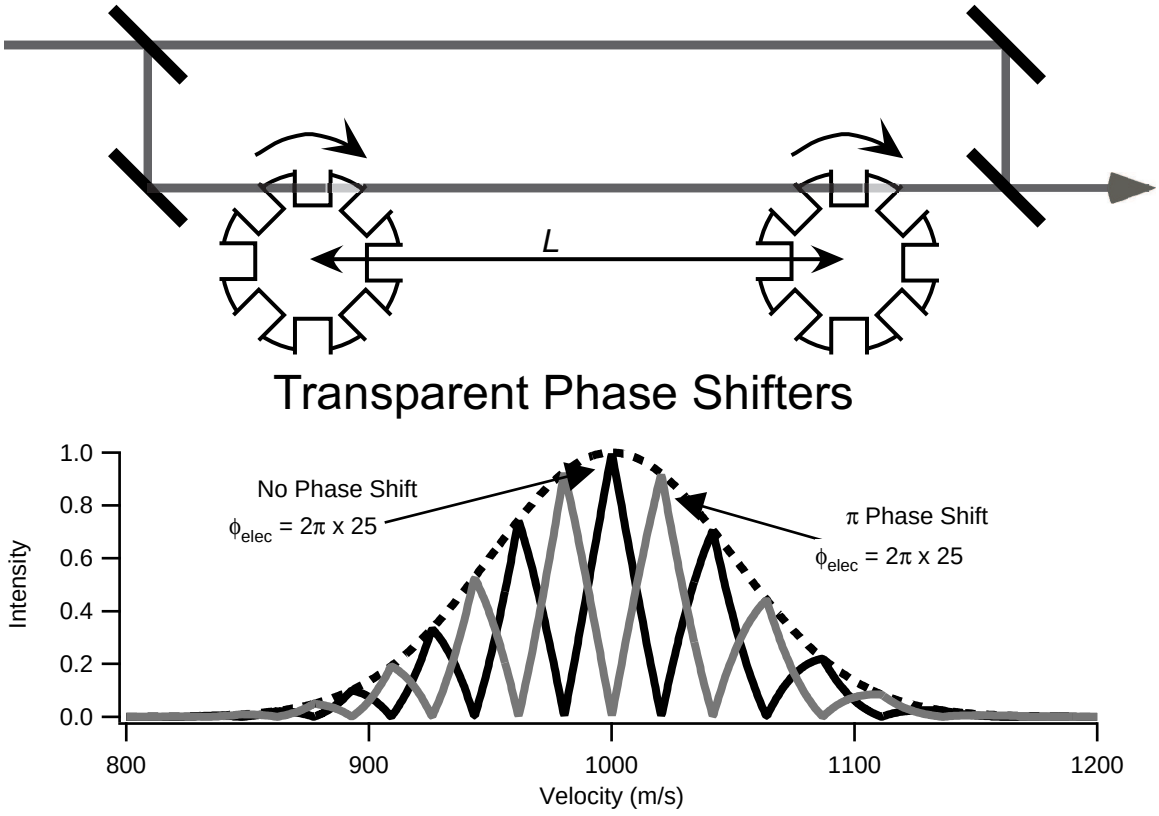

Figure 3-2: A schematic of phase choppers and the corresponding velocity distribution, using the same parameters as in Fig. 3-1. When they are on, the phase choppers introduce a π phase shift to the velocity distribution in grey, and the peaks of both velocity distributions contribute in phase to the interference pattern.

to deal with, which each pick up different total phases from the two choppers:

$$\begin{aligned} T_1(v) &= \Big\langle a(t)a(t+L/v)\Big\rangle_t && \text{Both choppers on} \\ T_2(v) &= \Big\langle a(t)\big[1-a(t+L/v)\big]\Big\rangle_t && \text{One on, one off} \\ T_3(v) &= \Big\langle \big[1-a(t)\big]a(t+L/v)\Big\rangle_t && \text{One off, one on} \\ T_4(v) &= \Big\langle \big[1-a(t)\big]\big[1-a(t+L/v)\big]\Big\rangle_t && \text{Both choppers off} \end{aligned} \tag{3.15}$$

Since we are driving the chopper with a square wave, $a(t)$ is the intensity of atoms transmitted when the chopper is on and $1-a(t)$ is the intensity transmitted when the chopper is off. Re-deriving the time-averaged transmission of the choppers (as in Eq. 3.9) while now allowing for chopping to occur out of phase (with a time delay t_{chop}),

$$T(v) = a_0^2 + \sum_{n=1}^{\infty} \frac{1}{2} a_n^2 \cos[n\omega(L/v + t_{\text{chop}})]. \tag{3.16}$$

Using the fact that $1-a(t) = a(t)|_{t_{\text{chop}}=\pi/\omega}$ for a 50% duty cycle and neglecting the rephasing at higher harmonics ($n \neq 1$) of the chopping frequency we find:

$$\begin{aligned} T_{1,4}(v) &= \frac{1}{4} + \frac{1}{2}\text{sinc}^2\big(\frac{\pi}{2}\big)\cos[\omega L/v] \\ T_{2,3}(v) &= \frac{1}{4} + \frac{1}{2}\text{sinc}^2\big(\frac{\pi}{2}\big)\cos[\omega L/v + \pi] \end{aligned} \tag{3.17}$$

Each of these distributions has a different interference pattern associated with it, picking up a π shift from each chopper if it is on:

$$\begin{aligned} I_1(v) &= N + A\cos\phi_0 \\ I_2(v) &= N + A\cos[\phi_0 + \pi] \\ I_3(v) &= N + A\cos[\phi_0 + \pi] = I_2(v) \\ I_4(v) &= N + A\cos[\phi_0 + 2\pi] = I_1(v) \end{aligned} \tag{3.18}$$

If we apply an electric field interaction, $\phi_{\text{int}}(v) = 2\pi v_{\text{ref}}/v$, such that $v_{\text{ref}} = \omega L/2\pi$,

Method	Duty Cycle	Intensity	Contrast	Signal-to-noise	Measurement Time
Mechanical Choppers	50%	0.25	0.405	0.203	24.3
Mechanical Choppers	37.1%	0.138	0.622	0.231	18.7
Phase Choppers	50%	1	0.405	0.405	6.1

Table 3.1: Comparison of the signal-to-noise ratio for mechanical vs phase choppers. All values are relative to an interference pattern in the absence of chopping with no electric field interaction applied.

the interference pattern created by the choppers is:

$$I = \int P(v)[T_1(v)I_1(v) + T_2(v)I_2(v) + T_3(v)I_3(v) + T_4(v)I_4(v)]dv. \tag{3.19}$$

Each of the four contributions to the interference pattern is exactly the same (note that $T_1I_1 = T_2I_2 = T_3I_3 = T_4I_4$), so the total interference pattern is:

$$I = N' + A' \cos\phi_0 \tag{3.20}$$

where $N' = N$ and the contrast $(A'/N') = (A/N)\text{sinc}^2(\pi/2) = 0.405$.

The advantage of phase choppers is that we get the same rephased interference pattern but with four times the signal. This greatly improves the signal-to-noise ratio in our measurement of the interference pattern (see Table 3.1).

3.2.4 Implementing Phase Choppers with a Gradient Field Region

Theoretical Design of a Gradient Field Region

The phase choppers must apply a relative phase shift between the two paths at a certain location inside the interferometer. To implement this experimentally, we need interactions that are physically small (so that their separation is precise) with an interaction phase that can be modulated very quickly. The best way to do this is by using an electric field gradient. We produce the gradient field using a charged cylinder located next to the interferometer paths (Fig. 3-3).

We will calculate how the gradient field affects the phase of the interferometer,

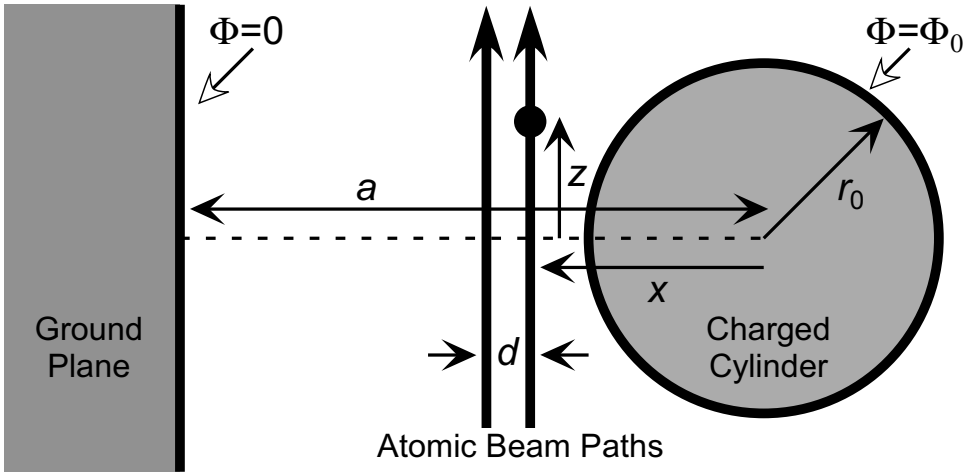

Figure 3-3: A charged cylinder is used to apply a differential phase shift to the separated paths of the wavefunction inside the interferometer.

and calculate the parameters of the setup required to produce a π phase shift. As an atom passes the charged cylinder, phase is accumulated at a rate ω_E where $\hbar\omega_E$ is the energy of the atom in the field. We can integrate the total phase accumulated along each path of the interferometer and take the difference to find the total phase shift of the interference pattern.

The charged cylinder has radius r and is at a potential $\Phi = \Phi_0$, oriented with its axis perpendicular to the plane of the interferometer. The cylinder sits next to a ground plane at $\Phi = 0$ a distance a from the axis and parallel to the axis and the beam. The potential around the cylinder is:

$$\Phi = \Phi_0 \ln^{-1}\left[\frac{a+b}{a-b}\right] \ln\left[\frac{(a+b-x)^2+z^2}{(a-b-x)^2+z^2}\right] \tag{3.21}$$

where $b \equiv \sqrt{a^2-r^2}$. The square of the electric field is:

$$E^2 = (\partial_x\Phi)^2 + (\partial_z\Phi)^2 = \Phi_0^2 \ln^{-2}\left[\frac{a+b}{a-b}\right] \frac{16b^2}{\left[(a+b-x)^2+z^2\right]\left[(a-b-x)^2+z^2\right]}. \tag{3.22}$$

The potential energy of a passing atom is $U(x,z) = -\frac{1}{2}\alpha E^2(x,z)$ and the total

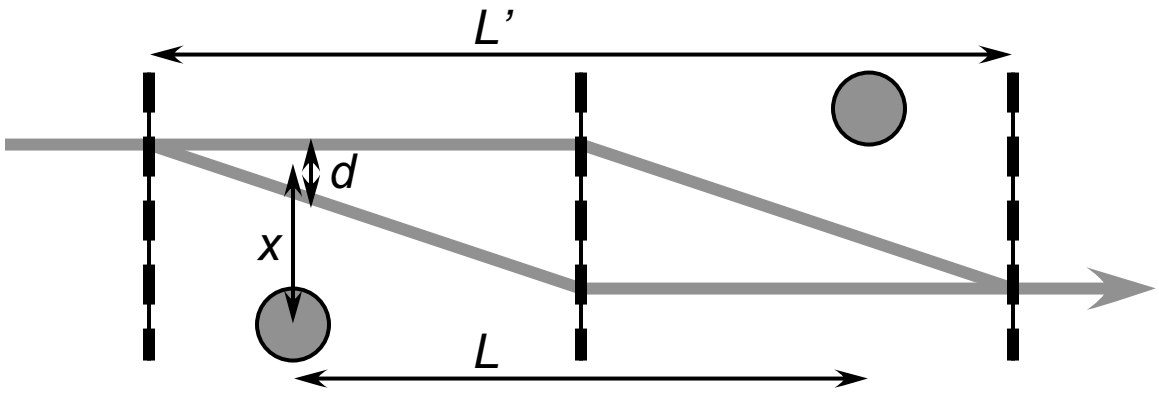

Figure 3-4: The charged cylinders apply a relative phase shift to the paths inside the interferometer.

phase acquired along one path through the interferometer is:

$$\begin{aligned}\theta(x) &= \int_{-\infty}^{\infty} \frac{1}{\hbar v} U(x,z)dz \\ &= -4\pi \frac{\alpha\Phi_0^2}{\hbar v} \ln^{-2}\left[\frac{a+b}{a-b}\right] \frac{b}{b^2-(a-x)^2}\end{aligned} \tag{3.23}$$

The phase shift to the interference pattern is the difference in the phase applied to the two paths of the interferometer, separated by distance d. For $d \ll x$ we can approximate the phase difference as $\Delta\theta \simeq \frac{d\theta}{dx} d$. d is given by the diffraction angle $\theta_{\text{diff}} = h/mv\lambda_g$ and the location of the choppers within the interferometer of total length L'. Assuming the choppers are equidistant from the second grating, then $d = (L'-L)h/2mv\lambda_g$, and the phase shift of the interference pattern is:

$$\Delta\theta = -8\pi^2 \frac{\alpha\Phi_0^2}{mv^2} \left(\frac{L'-L}{\lambda_g}\right) \ln^{-2}\left[\frac{a+b}{a-b}\right] \frac{b(a-x)}{\left[b^2-(a-x)^2\right]^2} \tag{3.24}$$

In the limit of $a \gg x$ (using $b \simeq a[1 - r^2/2a^2]$) this simplifies to

$$\Delta\theta \simeq -\frac{\pi^2}{2} \frac{\alpha\Phi_0^2}{mv^2} \left(\frac{L'-L}{\lambda_g}\right) \ln^{-2}(2a/r) \frac{1}{x^2}. \tag{3.25}$$

For sodium, $\alpha_{\text{Na}}/m_{\text{Na}} = 7.03 \times 10^{-14}$ volt^{-2} s^{-2} m^4 (for cesium, $\alpha_{\text{Cs}}/m_{\text{Cs}} =$

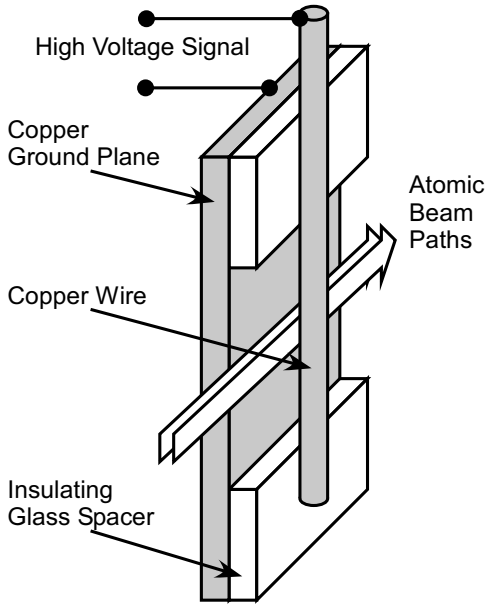

Figure 3-5: Schematic of the electric field gradient region used as a phase chopper.

$0.428 \times \alpha_{\mathrm{Na}}/m_{\mathrm{Na}}$). For the choppers we have constructed ($r = 0.5$ mm, $a = 1.5$ mm, $x \approx r$) with typical interferometer dimensions ($\lambda_g = 200$ nm, $L' - L = 1$ m) it takes a voltage of 1.2 kV to create a phase shift of π radians for a $v = 1$ km/s sodium beam.

Construction of the Gradient Field Region

Construction of the choppers is relatively simple. The ground plane is copper, about 1" wide by 3" tall, polished smooth to prevent arcing. A glass microscope slide with thickness $a - r_0 = 1$ mm is used as a spacer and high voltage insulator. A copper wire with a radius $r_0 = 0.5$ mm is separated from the ground plane by the glass separator. The elements are glued in place with epoxy, and electrical connections are soldered to the wire and back plane. The chopper is mounted through an insulator to a motorized stage. The stage moves the wire laterally for fine adjustment of the variable x, and tilts to make x the same at both the top and bottom of the 1 mm tall beam. The two choppers are placed equidistant from the second grating, with the distance between them measured to be $L = 985.8(4)$ mm.

Imperfections of the Gradient Field Region

The phase produced by the electric field gradient is not ideal. We desire the phased to be exactly $\Delta\theta = \pi$, but from Eq. 3.25 we find that the phase depends on the beam velocity and the location of the path relative to the cylinder. There is a spread in both of these parameters, which will cause a slight spread in phase when the field is on, reducing the contrast of the interference pattern.

To find the amount of contrast loss, first consider the velocity spread. The phase difference between the paths is $\Delta\theta(v) = \pi v_0^2/v^2$ where v_0 is the mean velocity. The $1/v^2$ dependence arises because the phase depends linearly on both the the transit time ($\propto 1/v$) and the path separation ($\propto 1/v$). Using the fact that

$$\int P(v)\cos[\phi_0 + \pi v_0^2/v^2]dv \simeq \exp\big[-2(\pi\sigma_v/v_0)^2\big]\cos[\phi_0+\pi] \tag{3.26}$$

we find that we can get a π phase shift only with a reduction in contrast by an amount $\exp\big[-2(\pi\sigma_v/v_0)^2\big]$.

If the beam has an appreciable width, the contrast will be further reduced because the phase depends on the distance from the cylinder. If the beam has a Gaussian spatial distribution $P(x) = (2\pi\sigma_x^2)^{-\frac{1}{2}}\exp[-\frac{1}{2}(x-x_0)^2/\sigma_x^2]$ we can apply a phase $\Delta\theta(x) = \pi x_0^2/x^2$ with resulting contrast loss $\exp\big[-2(\pi\sigma_x/x_0)^2\big]$ when a chopper is on.

In general, an arbitrary phase applied with a $1/v^\gamma$ velocity dependence,

$$\phi(v) = \phi_0\Big(\frac{v_0}{v}\Big)^\gamma \tag{3.27}$$

will suffer a change in contrast by a factor

$$\exp\Big[-\frac{1}{2}\gamma^2\big(\frac{\sigma_v}{v_0}\big)^2\phi_0^2\Big] \tag{3.28}$$

where σ_v/v_0 is assumed to be small.

Our field gradient regions apply a phase $\phi_0 = \pi$ with $\gamma = 2$, and for a velocity width $\sigma_v/v_0 = 0.05$ the contrast will be 95% of the original. If the gradient regions

are used to apply a phase $\phi_0 = 2\pi$ the contrast decreases to 82%.

3.2.5 Dephasing and Rephasing using Phase choppers

In Section 3.2.3 we calculated the contrast of the rephased interference pattern formed using the phase choppers. We extend this derivation now to find how the phase and contrast of the rephased fringe depends on the chopping parameters. We will also predict how the phase choppers function in the absence of the interaction phase, as they *dephase* the interference at high chopping frequency. We have measured this dephasing effect, and we show that it is a useful tool for accurately measuring the mean velocity and the shape of the velocity distribution.

Predicted Interference Pattern as a Function of Phase-Chopping Parameters

For a single velocity and no choppers, we represent the interference pattern as:

$$I = \cos\left[\phi_0 + 2\pi\left(\frac{v_{\mathrm{ref}}}{v}\right)^{\gamma}\right] \tag{3.29}$$

where $2\pi(v_{\mathrm{ref}}/v)^{\gamma}$ is a phase applied by an interaction region. We allow for the possibility of using a different kind of interaction region, with a $1/v^{\gamma}$ dependent phase (for instance, $\gamma = 1$ for a constant electric field region, or $\gamma = 2$ for a gradient field region). We have simplified the form of the interference pattern here; to get the actual interference pattern we can always multiply by A and add N to get $I = N + A\cos[\phi_0 + 2\pi(v_{\mathrm{ref}}/v)^{\gamma}]$.

For two identical choppers separated by L each applying π phase when on, we

create two new velocity distributions, $P_+(v)$ and $P_-(v)$:

$$\begin{aligned}
\text{Choppers off:} \qquad & P(v) = \frac{1}{\sqrt{2\pi\sigma^2}} \exp\Big[- \frac{(v-v_0)^2}{2\sigma^2} \Big] \\
\text{Choppers on:} \qquad & P_+(v) = P(v)T_+(v) = \big[\frac{1}{2} + \sum_{n=0}^{\infty} b_n \cos(n\omega L/v)\big] P(v) \\
& P_-(v) = P(v)T_-(v) = \big[\frac{1}{2} - \sum_{n=0}^{\infty} b_n \cos(n\omega L/v)\big] P(v)
\end{aligned} \tag{3.30}$$

The $P_+(v)$ distribution has an interference pattern with no phase difference. The $P_-(v)$ distribution has a π phase difference:

$$\begin{aligned}
I_+(v) &= \cos[\phi_0 + 2\pi(v_{\rm ref}/v)^\gamma] \\
I_-(v) &= \cos[\phi_0 + 2\pi(v_{\rm ref}/v)^\gamma + \pi] = -I_+(v)
\end{aligned} \tag{3.31}$$

The total interference pattern is:

$$\begin{aligned}
I &= \int dv[P_+(v)I_+(v) + P_-(v)I_-(v)] \\
&= \int dv P(v)[\sum_{n=1}^{\infty} 2\, b_n \cos(n\omega L/v)\, \cos(\phi_0 + 2\pi(v_{\rm ref}/v)^\gamma)]
\end{aligned} \tag{3.32}$$

Now express $\cos(n\omega L/v) = \frac{1}{2}[e^{in\omega L/v} + e^{-in\omega L/v}]$ and $\cos(\phi_0 + 2\pi(v_{\rm ref}/v)^\gamma) = \mathrm{Re}\, e^{i\phi_0}\, e^{i2\pi(v_{\rm ref}/v)^\gamma}$.

$$I = \mathrm{Re}\, e^{i\phi_0} \int dv P(v) \sum_{n=-\infty}^{\infty} b_n\, e^{in\omega L/v}\, e^{i2\pi(v_{\rm ref}/v)^\gamma} \tag{3.33}$$

where we define $b_0 \equiv 0$, and for 50% duty cycle square-wave chopping

$$b_n = \begin{cases} 0 & \text{for } n \text{ even} \\ \frac{4}{n^2\pi^2} & \text{for } n \text{ odd} \end{cases} \tag{3.34}$$

(In general, $b_n = \mathrm{sinc}^2[n\pi \times \text{duty cycle}]$.)

We can perform the integral using the approximation $v_0 \gg \sigma$ so $\frac{1}{v^\gamma} \approx \frac{1}{v_0^\gamma}(1 - \gamma\frac{v-v_0}{v_0})$.

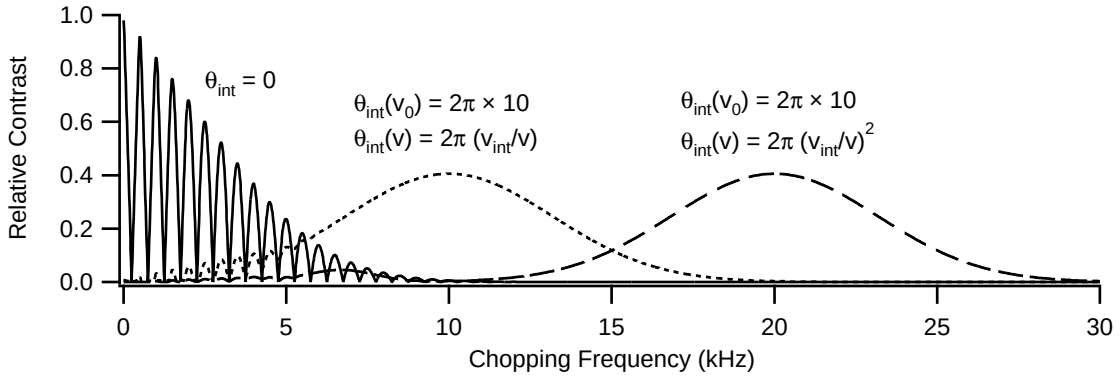

Figure 3-6: The contrast (from Eq. 3.35) vs the chopping frequency $f \equiv \omega/2\pi$ assuming $v_0 = 1$ km/s, $L = 1$ m, and $\sigma/v_0 = 5\%$. Three cases are shown: no interaction phase (—); a $1/v$-dependent interaction phase like that produced by a high voltage septum ($\cdots$); and a $1/v^2$-dependent interaction phase like an electric field gradient (– – –). Note that the mean phase applied is the same for both interactions ($2\pi \times 10$ radians), but the revivals occur at different frequencies. For the larger frequency revival, higher order revivals can be seen (though barely) at multiples $\frac{1}{3}, \frac{1}{5}, \ldots$ of the rephasing frequency.

Substituting $v' = v - v_0$,

$$I = \mathrm{Re}\, e^{i\phi_0} \sum_{n=-\infty}^{\infty} b_n\, e^{in\omega L/v_0}\, e^{i2\pi(v_{\mathrm{ref}}/v_0)^\gamma} \int dv' \frac{e^{-\frac{1}{2}v'^2/\sigma^2}}{\sqrt{2\pi\sigma^2}}\, e^{-in\omega L v'/v_0^2}\, e^{-i2\pi\gamma(v_{\mathrm{ref}}/v_0)^\gamma v'/v_0}$$

$$I = \sum_{n=-\infty}^{\infty} b_n \exp\Big(-\frac{1}{2}\Big[n\omega L/v_0 + 2\pi\gamma\big(\frac{v_{\mathrm{ref}}}{v_0}\big)^\gamma\Big]^2 \frac{\sigma^2}{v_0^2}\Big) \cos\Big[\phi_0 + n\omega L/v_0 + 2\pi\big(\frac{v_{\mathrm{ref}}}{v_0}\big)^\gamma\Big] \tag{3.35}$$

Dephasing

Now we can predict the effects of dephasing caused by the phase choppers. If the choppers are on but there is no interaction phase applied ($\theta_{\mathrm{int}} = 0$), Eq. 3.35 reduces to:

$$I = \cos\phi_0 \sum_{n=1}^{\infty} 2b_n\, e^{-\frac{1}{2}[n\omega L\sigma/v_0^2]^2} \cos[n\omega L/v_0]. \tag{3.36}$$

An example of this can be seen in the solid curve of Fig. 3-6.

Rephasing

If the interaction phase is large enough, $v_0/\sigma \lesssim (v_{\rm ref}/v_0)^\gamma$, and only $n < 0$ terms in Eq. 3.35 contribute:

$$I = \sum_{n'=1}^{\infty} b_{n'}\, e^{-\frac{1}{2}[n'\omega L/v_0 - \gamma\theta_{\rm int}]^2\sigma^2/v_0^2}\, \cos\left[\phi_0 - n\omega L/v_0 + \theta_{\rm int}\right]. \tag{3.37}$$

Revivals in contrast occur when the mean interaction phase, $\theta_{\rm int} \equiv 2\pi(v_{\rm ref}/v_0)^\gamma$, is an odd multiple of $\frac{1}{\gamma}\omega L/v_0$ (see Fig. 3-6). The main revival occurs at a frequency $f_{\rm reph} = \gamma\theta_{\rm int}v_0/2\pi L$, which for $\gamma = 1$ is equivalent to

$$f_{\rm reph} = v_{\rm ref}/L. \tag{3.38}$$

Experimental Verification

Experimental operation of square-wave electric choppers is demonstrated in Fig. 3-7, showing dephasing of the interference pattern as the chopping frequency is increased with no interaction applied. We can fit the data using Eq. 3.36, and adjusting the parameters v_0 and σ. The fit demonstrates that the electric choppers are working as expected. This a very precise method of measuring the velocity of the beam and its velocity distribution, yielding $v_0 = 3007(5)$ m/s, $\sigma/v_0 = 5.7(1)\%$. This measurement constitutes the most accurate determination of the beam velocity and rms velocity ever performed with the MIT atom interferometer.

3.3 Fully Rephased Interference Using Ramped-Phase Choppers

The analysis that we have considered so far uses phase choppers switching between discrete phases. We will show that by continuously ramping the phase of the choppers instead, we can actually achieve a full rephasing of the interference pattern, with an intensity and contrast equal to the original interference pattern.

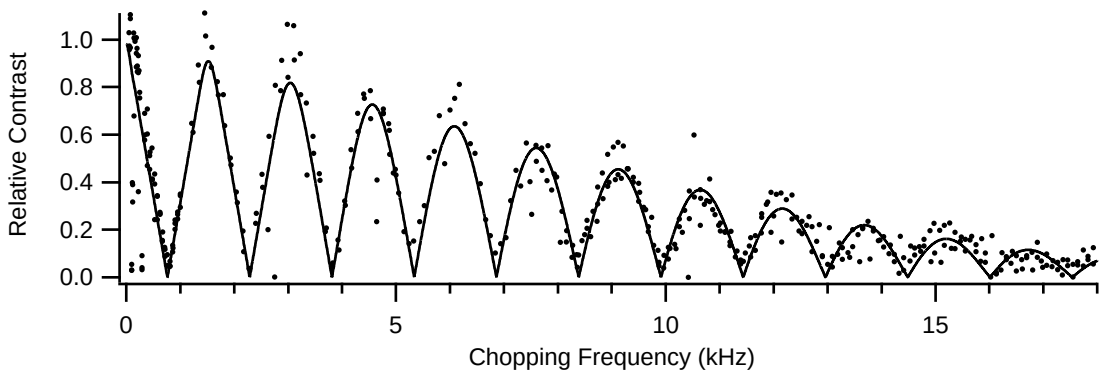

Figure 3-7: A measurement of contrast vs chopping frequency with no interaction phase applied. Eq. 3.36 was used to fit the data. The fit to the data yields a very precise method of measuring the mean and rms velocity: $v_0 = 3007(5)$ m/s, $\sigma/v_0 = 5.7(1)\%$.

3.3.1 Finding the Optimum Phase Function

We can control the gradient field choppers with a time-dependent voltage of any form, and we will now consider what the optimum time-dependent phase function would be. We will show that with the right function, it is possible to get rephasing with 100% of the initial signal-to-noise, for arbitrarily large interactions.

Consider the phase of each chopper having an arbitrary, periodic function of time, $\phi_1(t)$ and $\phi_2(t)$. We represent the original interference pattern (with no applied interaction or choppers) as $I = e^{\phi_0}$. (To get the actual interference pattern we can always take the real part, multiply by A, and add N.) Then in the presence of an interaction phase $\phi_{\rm int}(v) = 2\pi v_{\rm ref}/v$ and choppers phases $\phi_1(t)$ and $\phi_2(t)$ the interference pattern is:

$$I = \left\langle e^{i\phi_0}\ \ e^{i\phi_{\rm int}(v)}\ \ e^{i\phi_1(t)}\ \ e^{i\phi_2(t+L/v)} \right\rangle_{t,v} \tag{3.39}$$

where $\langle \ldots \rangle_{t,v} \leftrightarrow \int P(v)dv \int_{t=0}^{1/f} f dt$ is an average over time ($f = \omega/2\pi$ is the repetition frequency) and the velocity distribution.

We want $|I|$ to be as large as possible, ideally $|I| = 1$, and we would like the rephasing to occur no matter how wide the velocity distribution is. Consider I in the limit of large velocity $v \to \infty$, or any velocity for which L/v is an integer multiple of

$1/f$. Then for these velocities

$$I = \left\langle e^{i\phi_0}\, e^{i\phi_1(t)}\, e^{i\phi_2(t)} \right\rangle_t \tag{3.40}$$

For best contrast at these velocities we should choose $\phi_1(t) = -\phi_2(t)$. (They could differ by a constant phase as well, which we will choose to be zero.) At rephasing the repetition frequency will satisfy the rephasing condition (Eq. 3.38), $\omega L/v = \phi_{\rm int}(v)$. We then have

$$I = \left\langle e^{i\phi_0}\, e^{i\omega L/v}\, e^{i\phi_1(t)}\, e^{-i\phi_1(t+L/v)} \right\rangle_{t,v} \tag{3.41}$$

The contrast of the interference pattern would be ideal if we could satisfy the condition

$$\phi_1(t + L/v) - \phi_1(t) = \omega L/v \tag{3.42}$$

for all v. Again, to satisfy this equation in the limit $v \to \infty$, or for any v for which $L/v \approx n/f$, this reduces to the condition $\frac{d}{dt}\phi_1(t) L/v = \omega L/v$, from which we conclude

$$\phi_1(t) = -\phi_2(t) = 2\pi f t. \tag{3.43}$$

Substituting this form for $\phi_1(t)$ we find that the resulting contrast is actually ideal for any velocity distribution:

$$I = \left\langle e^{i\phi_0}\, e^{i\omega L/v}\, e^{i2\pi f t}\, e^{-i2\pi f(t+L/v)} \right\rangle_{t,v} = \left\langle e^{i\phi_0} \right\rangle_{t,v} = e^{i\phi_0}. \tag{3.44}$$

We have 100% rephasing of the original contrast!

The reason this works is that, due to the time-delay in traveling from the first to the second chopper, and due to the ramping of the second chopper phase, there is a larger phase applied to slower atoms. The velocity dependence of this phase exactly cancels the velocity dependence of the phase produced by the interaction region. The phase of the first chopper must be ramped as well, so that the sum of the phases of the two choppers doesn't depend on the time at which the atom enters the interferometer.

3.3.2 Predicted Interference Pattern as a Function of Ramped-Phase Parameters

We will now calculate how the phase and contrast of the rephased interference pattern depends on the parameters of the phase-ramp function. In Section 3.5, we will show that in a precision measurement of the interaction phase, the goal will be to determine the precise frequency at which rephasing occurs.

Combining Eq. 3.39 and Eq. 3.43 gives us:

$$I = e^{i\phi_0} \int P(v)dv\, e^{i\phi_{\rm int}(v)}\, e^{-i2\pi fL/v} \tag{3.45}$$

For a narrow Gaussian velocity distribution this reduces to:

$$I = C' e^{i\phi'} \tag{3.46}$$

where (quite similar to Eq. 3.6)

$$\begin{aligned} \phi' =& \phi_0 + 2\pi(v_{\rm ref} - fL)/v_0, \\ C' =& \exp\Big[-\frac{1}{2}\Big(\frac{2\pi(v_{\rm ref} - fL)\sigma_v}{v_0^2}\Big)^2\Big]. \end{aligned} \tag{3.47}$$

Or, in terms of the mean interaction phase applied $\overline{\phi}_{\rm int} \equiv \langle\phi_{\rm int}\rangle_v \approx \phi_{\rm int}(v_0)$,

$$\begin{aligned} \phi' =& \phi_0 + \overline{\phi}_{\rm int} - 2\pi fL/v_0, \\ C' =& \exp\Big[-\frac{1}{2}\Big(\overline{\phi}_{\rm int} - 2\pi fL/v_0\Big)^2\Big(\frac{\sigma_v}{v_0}\Big)^2\Big]. \end{aligned} \tag{3.48}$$

An example of the rephased contrast and phase is shown in Fig. 3-8. The rephasing frequency $f_{\rm reph}$ must be found by examining where the plotted phase $\phi' - \phi_0$ passes though zero underneath the exact center of the peak of the rephased contrast.

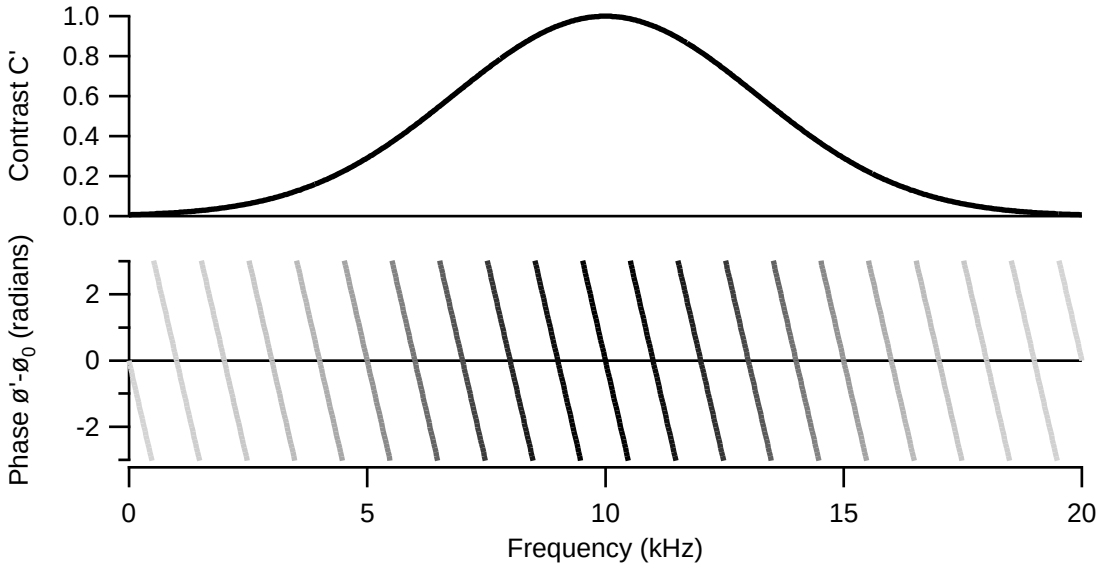

Figure 3-8: Contrast and phase of the interference pattern using ramped-phase choppers to perform the rephasing. In this example, we have used $v_0 = 1$ km/s, $\sigma_v/v_0 = 0.05$, $L = 1$ m, and an applied phase of $2\pi v_{\text{ref}}/v_0 = 2\pi \times 10$ rad. The resulting rephasing frequency under these conditions is $f_{\text{reph}} = 10$ kHz.

3.4 Implementing Ramped-Phase "Choppers"

It would be impossible in practice to apply a phase as in Eq. 3.43 that keeps increasing for all time. However, since a phase of 2π has no noticeable difference from a phase of zero, we can use a ramping phase that quickly returns to zero after reaching 2π or any multiple of 2π. The periodicity of the ramp is very important for another reason as well—instead of needing to measure the mean velocity of the beam with great accuracy, we will only need to know the repetition frequency f and chopper separation L.

To put this into practice, we must apply the correct time-dependent voltage to the phase choppers. Recall that the charged cylinders produce a phase that depends on the square of the applied voltage. To create a phase linear in time $\phi \sim t$ requires a voltage $\Phi_0 \sim \sqrt{t}$. In practice it would be expensive to produce such an arbitrary high-voltage waveform, which would require an arbitrary waveform generator and a very fast, high-power, high-voltage amplifier. We can overcome this difficulty be

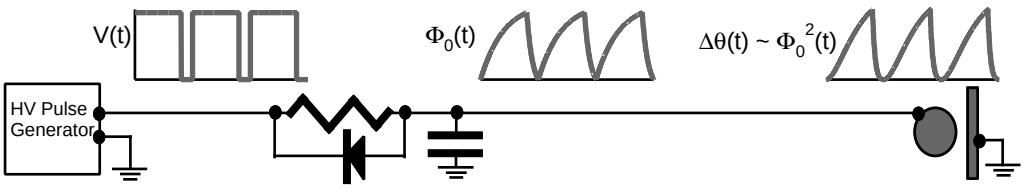

Figure 3-9: An approximate triangular phase ramp is created using a high voltage square wave and a low-pass RC filter.

approximating the square-root dependence with an RC circuit (Fig. 3-9). The pulse generator remains at a fixed high voltage most of the time, briefly returning to zero at the end of the cycle. When the input is high, the RC filtered voltage is $\Phi_0(1-e^{-t/RC})$. The voltage drains quickly to zero through a diode when the input is low. The phase produced is:

$$\phi_{1,2}(t) = \pm 2\pi\gamma(1 - e^{-t/RC})^2 \qquad 0 < (t \mod 1/f) < p/f. \tag{3.49}$$

We set $\gamma = 0.8$ and $RC = 0.4/f$ to best approximate a straight ramp when using a duty cycle $p = 90\%$. $\phi_{1,2}$ are made equal and opposite by applying the same voltage to each of gradient field region and orienting them on opposite sides of the interferometer, as in Fig. 3-10. The resulting phase and its deviation from an ideal ramp is discussed in detail in Section 3.6.1 (and plotted in Fig. 3-13) where we consider how the error affects the rephasing.

To demonstrate rephasing, we also need to apply the $1/v$-dependent interaction phase. We do this by exposing one path of the interferometer to a region of constant electric field, using the same type of assembly as describe in the last polarizability measurement [34]. It is essentially a parallel-plate capacitor, consisting of a 10 μm thin copper foil, or septum, suspended between metal plates separated with high-precision spacers (Fig. 3-10). The septum and one of the plates is kept at ground, and a high voltage is applied to the other plate. As discussed earlier, this applies a

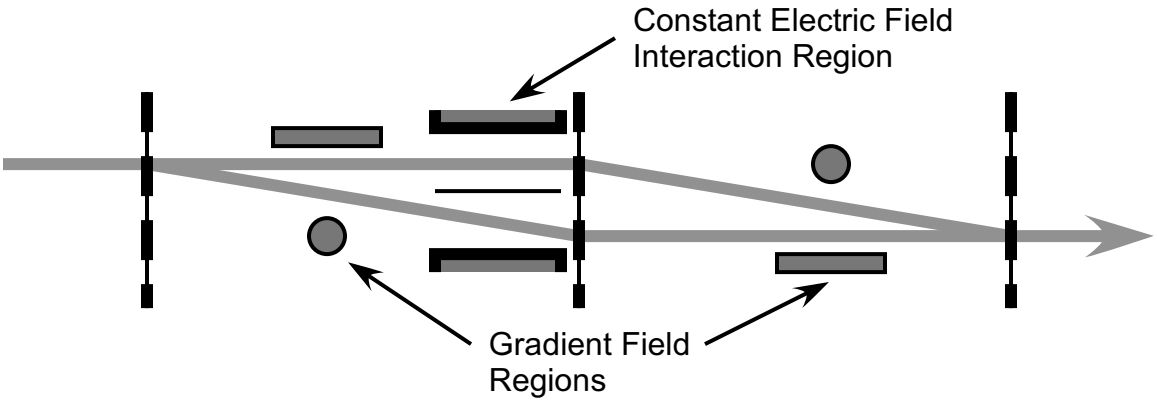

Figure 3-10: Interferometer layout for measuring rephased interference with an electric field interaction applied. In the depicted arrangement, the interaction region voltage must be applied to the *bottom* plate to see a rephasing, since the magnitude of the voltage applied to the gradient regions is *increasing* in time.

Stark shift to one path while leaving the other path undisturbed:

$$\phi_{\rm int}(v) = \frac{\alpha V^2 \ell}{2\hbar d^2}\,\frac{1}{v} \tag{3.50}$$

where V, ℓ, and d are the voltage, length, and plate separation of the interaction region.

3.5 Measuring Polarizability Using Ramped-Phase Choppers: A Demonstration

3.5.1 Contrast of Rephased Fringes

Using this scheme we have measured the rephased interference pattern as a function of applied voltage. In Fig. 3-11 we display the contrast of the interference fringes as a function of the average applied interaction phase, $\overline{\phi}_{\rm int} \approx \frac{\alpha V^2 \ell}{2\hbar d^2 v_0}$. The interaction phase is adjusted by scanning the septum voltage, V (a negative phase is introduced by

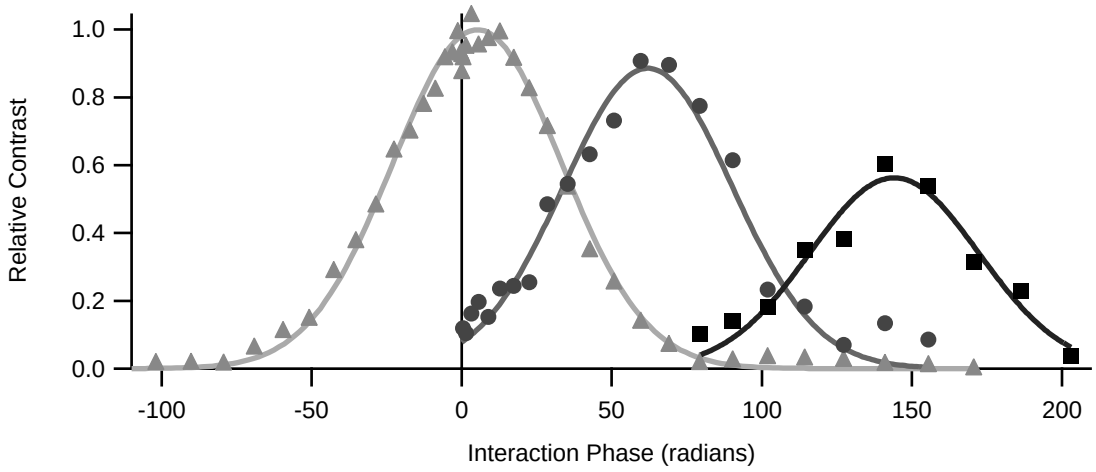

Figure 3-11: The contrast of the interference fringes as a function of the mean interaction phase, $\overline{\phi}_{\rm int} \approx \frac{\alpha V^2 \ell}{2\hbar d^2 v_0}$, measured with the choppers off (▲), and with the choppers on. At a chopping frequency of $f = 17$ kHz (●), we have achieved a 89% contrast revival at a mean interaction phase of 62 radians. At $f = 40$ kHz (■), a 56% revival is obtained at a mean phase of 144 radians.

applying voltage to the opposite side of the septum).[1] Data points were measured as a function of V but are plotted versus $\overline{\phi}_{\rm int}$ using the constant $\overline{\phi}_{\rm int}/V^2 = 35.3(2)$ rad/kV^2 for the particular septum and beam velocity used. We will show below how this constant is obtained from the phase data of the contrast revivals.

The plotted points have been fit with a Gaussian curve according to Eqs. 3.6 and 3.48. The rephased interference at 62 radians is 89% of the original contrast. This about the maximum expected using a ramp with a 90% duty cycle, as discussed earlier. The revival at 144 radians is only 56% of the original contrast. This is most likely because the ramp parameters γ and RC were not optimized (these factors need to be re-tweaked every time the frequency is changed, and the frequency must be changed when the interaction phase is changed), but there are many other factors that can lower the rephased contrast as well. These will be discussed later along with other chopper errors and imperfections.

[1]Note that the normal contrast envelope without the choppers can be slightly offset from zero due to the presence of any of a number of possible velocity dependent interactions: rotation phase due to the earth's spin, gravity phase (Eq. 1.16), or the diffraction-angle-dependent alignment errors $\Delta\phi_2$ and $\Delta\phi_4$ mentioned in Chapter 1.

The envelopes of the contrast revivals can be used to determine information about the velocity distribution of the beam. Eq. 3.45 shows that, the envelope is the Fourier transform of the velocity distribution, which is well-modeled by a Gaussian since the velocity distribution is approximately Gaussian. All three of the contrast envelopes are fit with the same width Gaussian, from which we infer that the rms velocity width of the beam is $\sigma_v/v_0 = 3.55(6)\%$. The mean velocity can be inferred too. When the rephased contrast is peaked, the relation $\overline{\phi}_{\rm int} = 2\pi f L/v_0$ holds. From the centers of the 17 kHz and 40 kHz peaks, we find mean velocities of $v_0 = 1700(40)$ m/s and $v_0 = 1720(40)$ m/s respectively. (The mean velocity can be found even more accurately by using the phase data.)

When we compare this with measurements of v_0 and σ_v as determined from the diffraction pattern, we find a large difference. A fit to the diffraction from a 100 nm grating finds a mean velocity $v_0 = 1940(10)$ m/s and $\sigma_v/v_0 = 6.8\%$. The discrepancy is not due to an error in either method of velocity measurement, but arises because the velocity distribution itself is different in the two cases.[2] Atoms with a smaller diffraction angle (larger velocity) have a greater chance of being blocked by the septum, making the mean velocity smaller and the velocity spread narrower. Also, when interference is measured there is a correlation between velocity and the position of the detector (just as exists in the diffraction pattern) resulting in a narrower velocity spread. These were both complications that needed to be modeled in the previous polarizability measurement [34], and contributed to about half of the reported systematic error. This is just one of the many sources of systematic error eliminated by using phase choppers.

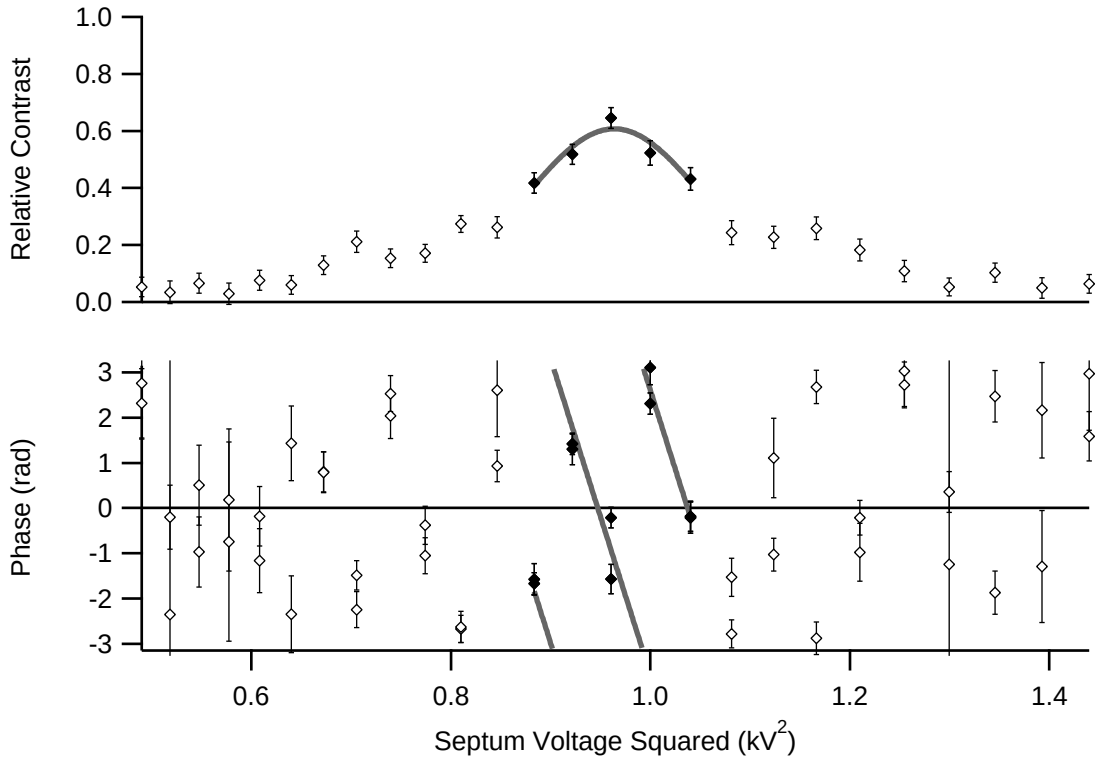

Figure 3-12: The contrast and phase of the rephased fringes as a function of the voltage-squared in the interaction region. By finding the voltage at which the interference pattern is exactly rephased (i.e. where the phase is zero under the peak) the polarizability can be determined very accurately. Note that the phase error is small only where the contrast revives.

3.5.2 Phase of Rephased Fringes

At rephasing, the condition

$$\frac{\alpha V^2 \ell}{2\hbar d^2 v} = 2\pi f L/v \tag{3.51}$$

holds for all v. Since we will be using a fixed frequency f in this experiment, our goal will be to determine the voltage V_{reph} that gives perfect rephasing. Then we will be able to express the polarizability in terms of very precisely known quantities:

$$\alpha = \frac{2hfL}{V_{\text{reph}}^2}\left(\frac{d^2}{\ell}\right) \tag{3.52}$$

so long as the geometry of the interaction region, characterized by d^2/ℓ, is well determined.

We have already seen one way of finding V_{reph}—by fitting the location of the peak contrast revival as in Fig. 3-11—however, using the phase of the revival is much more accurate. We know that at $V = V_{\text{reph}}$ the phase of the revival is exactly zero, and since the phase changes very steeply with voltage, we can find the zero crossing very precisely. To demonstrate this we refer to Fig. 3-12, which shows the contrast and phase of the interference revival measured at various septum voltages. (A different length septum and beam velocity was used here, so the phase for a given septum voltage will be different compared to Fig. 3-11.) To reduce errors due to phase drift of the interferometer, the data were taken by alternating very quickly between a measurement of the fringe with the choppers and interaction region on, and again with both turned off. We are interested in the relative ratio of the contrasts, $C_{\text{rel}} = C_{\text{“on”}}/C_{\text{“off”}}$, and the relative phase difference $\phi_{\text{rel}} = \phi_{\text{“on”}}/\phi_{\text{“off”}}$. By doing a comparison measurement on a short timescale we reduce errors due to vibration and thermal drift.

[2]We have, however, discovered an irregularity in the diffraction measurement that may contribute to the error. The separation between the $+1$ and 0^{th} order peaks sometimes differs by as much as 10% from the -1 and 0^{th} order separation, most likely due to an alinearity in the detector translation motor drive.

Based on Eq. 3.45, we predict:

$$C_{\rm rel}\, e^{i\phi_{\rm rel}} = \int P(v)\, dv\, e^{i2\pi\left(fL - \frac{\alpha V^2 \ell}{2hd^2}\right)/v} \tag{3.53}$$

By inspection, $\phi_{\rm rel}|_{V_{\rm reph}} = 0$ *exactly*. For arbitrary V we have:

$$\phi_{\rm rel} = 2\pi\big[fL - \frac{\alpha V^2 \ell}{2hd^2}\big]/v_0, \tag{3.54}$$

Keep in mind that whereas this expression is exact for $V = V_{\rm reph}$, it is only an *approximation* for $V \neq V_{\rm reph}$—the expression is true only in the limit of a very narrow velocity distribution (it is only approximate that $\langle\phi_{\rm int}(v)\rangle_v = \phi_{\rm int}(v_0)$), and the velocity distribution is not predicted to be precisely Gaussian anyway.

To find the zero crossing, we first must find the location of the contrast revival peak. This was accomplished by fitting a Gaussian to the highest contrast points (grey line in Fig. 3-12 contrast plot). The contrast measurements define the peak of the revival well enough so that we can choose the right zero crossing and are not off by a multiple of 2π (this kind of error would show up as a deviation in the α dependence on V). Next, we use the location of the contrast peak as a guess for fitting a line through the zero crossing (grey line in Fig. 3-12 phase plot). $V_{\rm reph}$ is the voltage at which the line fit crosses zero.

Residuals of the fit are shown below the phase plot. The residuals outside the range of the line fit are scattered around zero, confirming that we have unwrapped the phase correctly. This also displays how the error in the phase measurement grows rapidly as the contrast decays.

The zero crossing as determined by the line fit is $V^2_{\rm reph} = 0.947(2)$ kV^2. The data were taken at a ramp frequency $f = 21.40(5)$ kHz, with choppers a distance $L = 98.58(4)$ cm apart. The effective length of the septum was $\ell = 4.6(2)$ cm with $d = 0.2000(3)$ cm for the septum spacing.[3]

[3]The septum used here did not have guard electrodes. This made the measurement of ℓ fairly uncertain. The length also varied across the height of the beam, creating a spread in applied interaction phase contributing to loss of contrast in the contrast revival. This motivated construction

To calculate the measured polarizability given these parameters, use the following for Planck's constant,

$$h = 5.955\ 213\ 6(5) \times 10^{-22}\ \text{cm}^3\ (\text{volt/cm})^2\ \text{sec}, \tag{3.55}$$

derived from 1998 CODATA recommended values. Using this will give the polarizability in Gaussian units of cm^3. Take care in using this form of h—it is a convenient way to use the SI unit of volt in an equation that is only meant for Gaussian units.

Our determination of α in this example is

$$\alpha = \frac{2hfL}{V_{\text{reph}}^2}\left(\frac{d^2}{\ell}\right) = 23.07(1.04)_{\text{geom}}(0.06)_{\text{chop}}(0.05)_{\text{stat}}\ \text{Å}^3. \tag{3.56}$$

This agrees with the MIT interferometer's published value of $\alpha = 24.1(1)\ \text{Å}^3$. Let's discuss the errors in our measurement of α. Certainly the biggest here is the geometry, which has a large uncertainty here because we didn't take the same care that went into the precision of the old measurement. In an actual polarizability measurement, the geometry could be measured to a precision of 0.2% using the techniques of the old experiment. A subsequent section will suggest how this uncertainty can be overcome, by either improving the knowledge of d^2/ℓ or performing a relative measurement in which dependence on the geometry is eliminated.

The second source of uncertainty arises from the dependence on the chopping parameters f and L. In an actual polarizability measurement f would effectively be exact, by means of a frequency counter or a precision function generator. L was measured to a precision of 4×10^{-4} simply by measuring it with a long ruler. This could certainly be pushed to $\pm100\ \mu$m out of a meter, or orders better if an interferometric method was used. The chopping also introduces some systematic error, but we will discuss this in the next section.

The last amount of certainty comes from the error in V_{reph}. In a precision measurement, V will have to be measured with a precision voltmeter, but in our experiment

of a new septum with guard electrodes, which was used to take the data in Fig. 3-11.

the source of error is the statistical nature of the phase measurement. This depends on how many phase measurements are taken, the rms phase error of each measurement, and the slope of the phase as it depends on the square-voltage. Using the velocity of the beam we can predict the slope of the phase and hence the statistical error:

$$\frac{\Delta\alpha_{\rm stat}}{\alpha} = \frac{\Delta V^2_{\rm reph}}{V^2_{\rm reph}} = \frac{v_0}{2\pi f L}\ \phi_{\rm rms}/\sqrt{N} \tag{3.57}$$

(As a side note, alternatively we can use the slope of the line fit to determine the mean velocity $v_0 = \frac{2\pi f L}{V^2_{\rm reph}}\frac{d}{d\phi}(V^2)$. If we fit a line through *all* of the phase points in Fig. 3-12, we find $v_0 = 1962(8)$ m/s.)

In this example there are only $N = 10$ phase measurements (two measurements at each of five different voltages), each with $\phi_{\rm rms} \approx 400$ mrad. $\phi_{\rm rms}$ is unusually large here for two reasons—each choppers-on and choppers-off fringe measurement was only 1 sec long, and there was a delay of 10 sec between each measurement (which allowed the phase drift to grow). Combining the measurements, we have a total phase error of 400 mrad$/\sqrt{10} = 130$ mrad in 20 sec of measurement time (neglecting the delay between measurements). The resulting statistical error in α is 0.2% The error could easily be made even smaller by shrinking the delay time, thereby minimizing the phase drift error.

For comparison, the old experiment measuring α took 10 min of data collection time to reach the same statistical precision of 0.2%. This demonstrates the great advantage of applying large interaction phases using the rephasing technique.[4]

Consider what we are now capable of in a comparable amount of data collection time. Conservatively, we could alternate between a choppers-on and choppers-off fringe measurement every $\frac{1}{2}$ sec and still have plenty of signal for each fringe fit. We had a count rate of 65 kHz with a choppers-off contrast of 16% and a revival contrast of 9%, so in a half second the phase can be fit to $\sqrt{2}/C\sqrt{N} = 50$ mrad (see Appendix E),

[4]It might be thought that we have an additional advantage over the old experiment due to having much higher flux from a beam with twice the velocity, as made possible by the new 100 nm gratings. However, the 100 nm gratings have much lower contrast, and the signal-to-noise here ($9\% \times \sqrt{65\ \text{kHz}}$) is the same as in 1995 ($35\% \times \sqrt{3.5\ \text{kHz}}$)

or 90 mrad with choppers on. Our short term phase drift is approximately 30 mrad in $\frac{1}{2}$ sec. Then for each phase measurement, comprising 1 sec of data ($\frac{1}{2}$ sec on, $\frac{1}{2}$ sec off), the total rms statistical phase error is $\phi_{\rm stat} = 110$ mrad. In 10 min, the phase error is down to 4 mrad, with corresponding error $\Delta\alpha_{\rm stat}/\alpha = 6 \times 10^{-5}$. And this result only assumes rephasing at the applied phase $\phi_{\rm int}(v_0) = 66$ rad used here. Larger phases are possible, and the statistical error will decrease in proportion to how far out the rephasing occurs.

3.6 Sources of Systematic Error

The phase chopping technique falls short of ideal in several respects, which introduce several imperfections into the polarizability measurement, some of which may produce an error in the phase of the rephased fringe and affect the accuracy of a polarizability measurement:

1. The phase applied is not an ideal ramp function.

2. The chopper phase varies across the width of the beam.

3. The magnitude of the phase applied is unequal between the two choppers due to imperfect translational alignment.

4. The chopper phase depends on velocity—slower atoms see a stronger phase ramp function.

5. The choppers have a finite length, so the chopper phase function will be destroyed if the transit time is large compared to the repetition period.

All of these effects arise because we cannot apply a perfect ramp with each chopper:

$$\begin{aligned} \phi_1(t) &= +2\pi f t + \delta\phi_1(t) + i\Delta_1(t) \\ \phi_2(t) &= -2\pi f t - \delta\phi_2(t) + i\Delta_2(t) \end{aligned} \tag{3.58}$$

where $\delta\phi_{1,2}(t)$ accounts for the imprecision in the phase (Imperfections 1 and 2), and $\Delta_{1,2}(t)$ accounts for loss of contrast (Imperfection 3) due to the applied chopper phase. These functions may depend on velocity as well (Imperfections 4 and 5).

If we represent the interference pattern as $I = e^{i\phi_0}$ when the choppers and interaction region are off, then with everything turned on we have $I = e^{i\phi_0} I'$ where

$$I' = \left\langle e^{i\phi_{\rm int}(v)}\, e^{i\phi_1(t)}\, e^{i\phi_2(t+L/v)} \right\rangle_{t,v} \tag{3.59}$$

We can re-express this as

$$I' = \left\langle e^{i(\omega_{\rm int}-\omega)L/v}\, a_1(t)\, a_2^*(t+L/v) \right\rangle_{t,v} \tag{3.60}$$

where $\hbar\omega_{\rm int} \equiv (\frac{1}{2}\alpha V^2/d^2) \times (\ell/L)$, or $\omega_{\rm int} = 2\pi v_{\rm ref}/L$, and

$$a_{1,2}(t) \equiv e^{i\delta\phi_{1,2}(t)}\, e^{-\Delta_{1,2}(t)} = \sum_{n=-\infty}^{\infty} c_{1,2\,n}\, e^{in\omega t}. \tag{3.61}$$

By expressing $a_{1,2}(t)$ in terms of a Fourier series, we can simplify the average over t:

$$\left\langle a_1(t)\, a_2^*(t+t') \right\rangle_t = \left\langle \sum_{n,m} c_{1\,n} {c_2}^*_m\, e^{in\omega t}\, e^{-im\omega(t+t')} \right\rangle_t = \sum_n c_{1\,n} {c_2}^*_n\, e^{-in\omega t'} \tag{3.62}$$

We will define the preceding expression as the convolution function, $g(t')$:

$$g(t') \equiv \left\langle a_1(t)\, a_2^*(t+t') \right\rangle_t = \sum_n g_n\, e^{in\omega t'} \qquad \text{with} \qquad g_n = c_{1\,-n} {c_2}^*_{-n} \tag{3.63}$$

We now have:

$$I' = \left\langle e^{i(\omega_{\rm int}-\omega)L/v}\, g(L/v) \right\rangle_v \tag{3.64}$$

We could perform the average over v, but to simplify matters, we will switch to an average over $\tau \equiv L/v$ instead. τ is the time it takes for an atom with velocity v to get from one chopper to the other. We will neglect for the time being the fact that

the coefficients g_n have some velocity dependence due to Imperfections 4 and 5.

$$I' = \left\langle e^{i(\omega_{\rm int}-\omega)\tau}\, g(\tau) \right\rangle_\tau \tag{3.65}$$

Since $P(v)$ is roughly Gaussian, then the probability distribution $P'(\tau)$ is roughly Gaussian too, with mean $\tau_0 \equiv L/v_0$ and rms width $\sigma_\tau \equiv \tau_0(\sigma_v/v_0)$. [5]

$$\begin{aligned} I' &= \int_{-\infty}^{\infty} d\tau \left(\frac{e^{-\frac{1}{2}(\tau-\tau_0)^2/\sigma_\tau^2}}{\sqrt{2\pi\sigma_\tau^2}} \right) e^{i(\omega_{\rm int}-\omega)\tau} \sum_n g_n\, e^{in\omega\tau} \\ &= e^{i(\omega_{\rm int}-\omega)\tau_0} \sum_n g_n\, e^{in\omega\tau_0}\, e^{-\frac{1}{2}(\omega_{\rm int}-\omega+n\omega)^2\sigma_\tau^2} \end{aligned} \tag{3.66}$$

With this expression we can determine Imperfections 1, 2 and 3. Nowhere, however, have we assumed the imprecisions are small, and therefore Eq. 3.66 is perfectly general. We can use it to derive the rephased fringes of *any* form of chopping whatsoever, for instance the amplitude choppers from Section 3.2.2 (with $\phi(t)$ as an imaginary square wave) or the square wave phase choppers from Section 3.2.3 (as well as their low frequency behavior measured in Fig. 3-7).

For the purpose of measuring α, we are only concerned with I' for frequencies near the chopping frequency, $\omega_{\rm int} \approx \omega$. Then the $n = 0$ term will be the largest in the series. Furthermore, the $n \neq 0$ terms will be negligible—these terms are exponentially small, by a factor $e^{-\frac{1}{2}n^2\omega^2\sigma_\tau^2}$. Let's look at how small this actually is. For a modest rephasing frequency, $f = 25$ kHz, and a beam with $v_0 = 1$ km/s and $\sigma_v/v_0 = 0.05$, this factor is $\sim 10^{-14}$.

Consider the g_0 term. As a Fourier coefficient it is $g_0 = \langle g(t')\rangle_{t'}$. It can be simplified, however:

$$g_0 = \left\langle a_1(t)\, a_2^*(t+t') \right\rangle_{t,t'} = \left\langle a_1(t) \right\rangle_t \left\langle a_2^*(t) \right\rangle_t \tag{3.67}$$

[5] Since we are concerned with very small effects in this section, it may not be precise enough to approximate $P'(\tau)$ as Gaussian, in which case we can find $P'(\tau)$ from $P(v)$ using $P'(\tau)d\tau = -\frac{L}{\tau^2}P(L/\tau)d\tau$. When doing so, however, we should use the more appropriate v^3 weighted Gaussian for $P(v)$ for the same reasons.

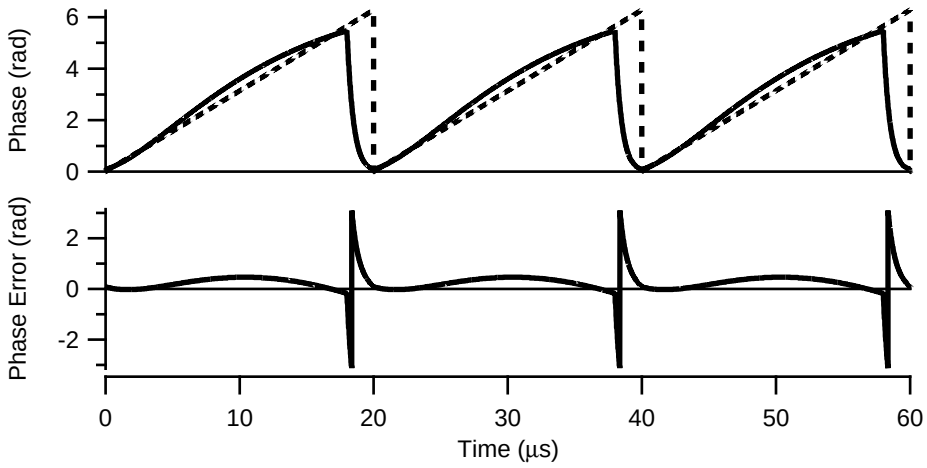

Figure 3-13: The phase function $\phi(t)$ (as defined by Eq. 3.69) used to approximate an ideal ramp, and the deviation from ideal $\delta\phi(t)$. Parameters used in the model are $f = 50$ kHz, $p = 90\%$, $RC = .43/f$, and $\gamma = 1.1$. The imperfection produces no phase error, but limits the rephased contrast to a maximum of 86%.

Finally then, the interference fringe is:

$$I' = e^{i(\omega_{\text{int}}-\omega)L/v_0}\, e^{-\frac{1}{2}(\frac{\sigma_v}{v_0})^2(\omega_{\text{int}}-\omega)^2L^2/v_0^2} \left\langle e^{-\Delta_1(t)+i\delta\phi_1(t)}\right\rangle_t \left\langle e^{-\Delta_2(t)-i\delta\phi_2(t)}\right\rangle_t \tag{3.68}$$

3.6.1 Imperfection 1: Non-ramp function

We will assume the choppers are driven with an RC-filtered square wave with the following form:

$$\phi(t) = 2\pi\,\gamma \times \begin{cases} \left[1 - e^{-t/RC}\left(\frac{1}{1+e^{-p/fRC}}\right)\right]^2 & \text{for } 0 < t < p/f \\ \left[e^{-\frac{p}{1-p}(t-p/f)/RC}\left(\frac{1}{1+e^{-p/fRC}}\right)\right]^2 & \text{for } p/f < t < 1/f \end{cases} \tag{3.69}$$

$p \approx 0.9$ is the duty cycle, $RC \approx 0.4/f$ is the RC time constant, and $\gamma \approx 1$ describes the strength of the phase. This function takes into account the fact that the phase doesn't have time to decay all the way to zero during the off cycle. This function and the corresponding $\delta\phi(t)$ are plotted in Fig. 3-13. We will consider this function as a worst-case scenario for a future polarizability measurement—it is simply a matter of

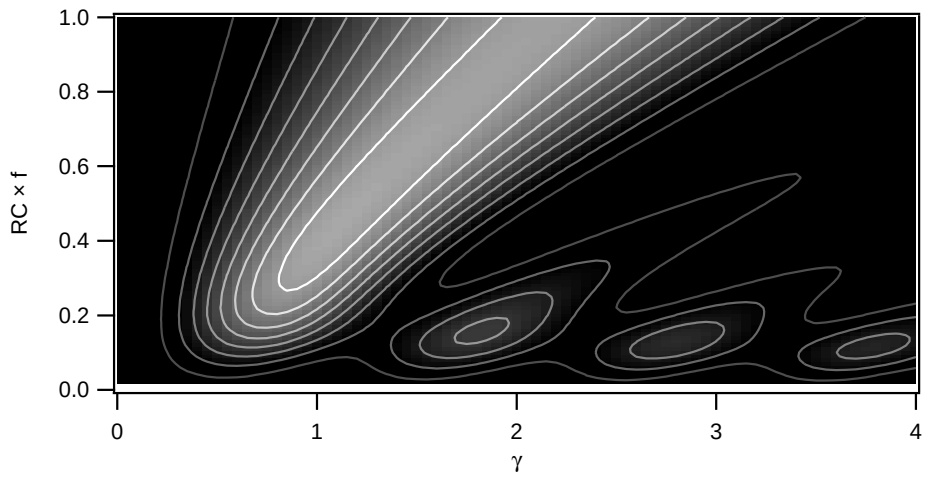

Figure 3-14: The rephased contrast as a function of the dimensionless parameters γ (the strength of the phase) and $RC \times f$ (roughly representing the slope of the phase) when using a filtered square wave function of Eq. 3.69 with a $p = 90\%$ duty-cycle. The contour lines are at 10% intervals. The highest contour (white) shows there is a wide range of parameters giving 80% or greater contrast.

resources to use an arbitrary waveform generator amplified to high voltage to attain a near perfect ramp.

Using Eq. 3.68, the interference pattern is:

$$I' = e^{i(\omega_{\rm int}-\omega)L/v_0}\, e^{-\frac{1}{2}(\frac{\sigma_v}{v_0})^2(\omega_{\rm int}-\omega)^2L^2/v_0^2} \left|\left\langle e^{i\delta\phi(t)}\right\rangle_t\right|^2 \tag{3.70}$$

We can conclude that there will be a reduction in contrast, but no change in the phase, and hence no systematic error in measuring α. For $\delta\phi(t)$ resulting from Eq. 3.69, we can attain a 86% rephasing of the contrast using a $p = 90\%$ duty cycle at values $\gamma = 1.1$ and $RC = .43/f$. Fig. 3-14 shows the dependence of the rephased contrast on γ and RC.

3.6.2 Imperfection 2: Phase variation across the beam width

The phase an atom picks up after passing a distance x from the center of the chopper wire varies as $\phi \sim 1/x^2$. The profile of the beam can be represented by a Gaussian, centered at x_0 with rms width σ_x. The wire is wide enough so that $\sigma_x \ll x_0$. If the

applied phase is large enough, the spread in phase averaged over the width of the beam will cause contrast loss in addition to a phase shift to the original interference pattern (represented by $e^{i\phi_0}$):

$$e^{i\phi_0} \rightarrow \int dx \left(\frac{e^{-\frac{1}{2}(x-x_0)^2/\sigma_x^2}}{\sqrt{2\pi\sigma_x^2}} \right) e^{i[\phi_0+\phi(x)]} = e^{-2(\sigma_x/x_0)^2\,\phi^2(x_0)}\, e^{i[\phi_0+\phi(x_0)]} \tag{3.71}$$

To find the time averaged contrast loss, we must average over the time dependence of the choppers as well. As a function of time, $\phi(x_0) \approx \omega t$. The contrast loss as a function of time is proportional to $e^{-\Delta(t)}$ where

$$\Delta(t) = 2\big(\frac{\sigma_x}{x_0}\big)^2 \omega^2 t^2 \tag{3.72}$$

Due to the expanding collimation, the beam is actually a different width at the two choppers, σ_{x1} and σ_{x2}. The rephased interference pattern is:

$$\begin{aligned} I' &= e^{i(\omega_{\rm int}-\omega)L/v_0}\, e^{-\frac{1}{2}(\frac{\sigma_v}{v_0})^2(\omega_{\rm int}-\omega)^2L^2/v_0^2} \left\langle e^{-\Delta_1(t)} \right\rangle_t \left\langle e^{-\Delta_2(t)} \right\rangle_t \\ &\approx e^{i(\omega_{\rm int}-\omega)L/v_0}\, e^{-\frac{1}{2}(\frac{\sigma_v}{v_0})^2(\omega_{\rm int}-\omega)^2L^2/v_0^2} \left[1 - \frac{8\pi^2}{3}\Big(\frac{{\sigma_{x1}}^2 + {\sigma_{x2}}^2}{x_0^2}\Big) \right] \end{aligned} \tag{3.73}$$

There is an overall loss of contrast, but no phase error, due to the phase spread across the width of the beam at both choppers. We typically use 15 μm collimating slits spaced about 1 m apart. The first chopper is about $\frac{1}{2}$ m downstream of the slits, and the second chopper about $\frac{3}{2}$ m downstream, so the rms beam widths (of the trapezoidal profile) are $\sigma_{x1} = 7$ μm and $\sigma_{x2} = 13$ μm respectively. x_0 is only slightly larger than the wire radius ($r = 0.5$ mm in the current setup). Eq. 3.73 then evaluates to a rephased contrast of $[1 - \frac{2\pi^2}{3}(\frac{{\sigma_{x1}}^2+{\sigma_{x2}}^2}{x_0^2})] = 98\%$.

The beam will also be effectively wider if it is tilted with respect to the wire. A 5° tilt in the wire relative to the 1 mm tall beam will reduce the contrast to 84%.

It may be profitable in a future experiment to reduce the radius of the wire at the expense of some loss of contrast. The benefits to be gained are a smaller voltage needed to get the same amount of phase, a relaxation of the frequency limitation imposed by Imperfection 5 (due to the chopper wire's finite size compared to the

chopper separation), and perhaps most importantly, a reduction in the phase error from Imperfection 3 (due to unequal strength of the two chopper phases).

3.6.3 Imperfection 3: Unequal strength of chopper phases

It is easy to guarantee that the choppers get the same signals electronically. Since the phase also depends on the spatial alignment, however, there is certain to be a difference in the phases due to the initial positioning error and subsequent thermal drift. The best way to align them, in fact, is to check using the interferometer that they give the same applied phase for a given voltage. We show that the remaining unknown difference in phase gives a direct uncertainty in the phase of the rephased fringe and hence a systematic error in α.

As defined in Eq. 3.68, the error in the phase of the rephased fringe will be $\phi_{\rm err}$, where:

$$Ce^{i\phi_{\rm err}} \equiv \langle e^{i\delta\phi_1(t)}\rangle_t \langle e^{-i\delta\phi_2(t)}\rangle_t \tag{3.74}$$

Since the choppers get the same voltage signal, we know ϕ_1 is proportional to ϕ_2:

$$\begin{aligned} \phi_1(t) &= \Big(1+\frac{\lambda}{2}\Big)\phi(t) \\ \phi_2(t) &= \Big(1-\frac{\lambda}{2}\Big)\phi(t) \end{aligned} \tag{3.75}$$

where λ is roughly the fractional difference between $\phi_1(t)$ and $\phi_2(t)$, and $\phi(t)$ is their average.

As it turns out, it is a very good approximation that

$$\phi_{\rm err} \approx \langle \phi_1(t) - \phi_2(t)\rangle_t = \lambda \langle \phi(t)\rangle_t \tag{3.76}$$

This approximation is good to 1% in $\phi_{\rm err}$, so long as $\lambda < 0.5$. [6] Since $\phi(t) \approx \omega t$, then $\langle\phi(t)\rangle_t \approx \pi$, and we can estimate roughly that $\phi_{\rm err} \approx \lambda\pi$, but this approximation is only good to 10% for the $\phi(t)$ in Fig. 3-13.

[6] This approximation works in spite of the fact that the equation $1 + i\langle\delta\phi(t)\rangle \approx \langle e^{i\delta\phi(t)}\rangle$ is a very *poor* approximation, which remains inaccurate even after 10 terms in the series expansion.

It quickly becomes apparent that any amount of data collection time spent trying to reduce the statistical error of the polarizability measurement will have to be matched by time spent measuring ϕ_{err}. There are two ways of dealing with this problem:

1. One method is to separately measure λ and $\langle\phi(t)\rangle$. λ can be measured with the interaction region off and with the choppers kept static at a fixed voltage, V_{fixed}. We choose V_{fixed} so that ϕ_1 and ϕ_2 are as large as possible (without introducing decoherence due to their velocity spread or reaching the breakdown voltage). Suppose we set $\phi_1 \approx -\phi_2 \approx 3\pi$, then we can measure $\lambda = (\phi_1 + \phi_2)/3\pi$. With the factor of 3 advantage, λ can be measured to the same precision as the polarizability phase in about $\frac{1}{9}$ the time. Ideally, λ would be measured beforehand to reduce it to as small a value as possible, and measured again occasionally while interspersed with the polarizability measurements to track drifts in λ due to thermal changes.

   If λ cannot be kept small enough, a measurement of $\langle\phi(t)\rangle$ would be needed in addition. This is more complicated, since it depends on two things: the precise form of the voltage waveform, $V^2(t)$, which would need to be monitored by an ADC through a voltage divider, and the proportionality constant of the phase to V^2, which could be measured the same way as λ but with only one chopper hooked up.

2. The second method is to measure ϕ_{err} directly, replacing the zero phase measurement. Instead of alternating between a fringe measurement with interaction-on/choppers-on and interaction-off/choppers-off, we can keep both of them on and alternate between a phase measurement taken at high rephasing frequency and low rephasing frequency. $\phi(t)$ needs to be independent of frequency for this to work, so we would use this method if we had an arbitrary waveform generator. This method would also work just so long as $\langle\phi(t)\rangle$ was equal at both high and low frequency.

3.6.4 Imperfection 4: Chopper phase dependence on velocity

An atom picks up a phase difference $\propto 1/v^2$ as it passes the chopper wire. To first order the effect is the same as that produced by Imperfection 2—the contrast loss as a function of time at each chopper is proportional to $e^{-\Delta(t)}$ where

$$\Delta(t) \approx 2\big(\frac{\sigma_v}{v_0}\big)^2 \omega^2 t^2, \tag{3.77}$$

which leads to a total time-averaged contrast of (see Eq. 3.73):

$$C \approx 1 - \frac{16\pi^2}{3}(\frac{{\sigma_v}^2}{v_0^2}) \tag{3.78}$$

This is about 87% for $\sigma_v/v_0 = 0.05$.

To estimate the size of the phase error, we need to return to Eq. 3.66

$$I' = \int_{-\infty}^{\infty} d\tau \left(\frac{e^{-\frac{1}{2}(\tau-\tau_0)^2/\sigma_\tau^2}}{\sqrt{2\pi\sigma_\tau^2}} \right) e^{i(\omega_{\rm int}-\omega)\tau} \sum_n g_n \, e^{in\omega\tau} \tag{3.79}$$

We know that the $n \neq 0$ terms are insignificant, but we must consider that g_0 (Eq. 3.67) has some slight velocity dependence. Recall that

$$g_0 \equiv \langle e^{i\delta\phi_1(t)} \rangle_t \langle e^{-i\delta\phi_2(t)} \rangle_t. \tag{3.80}$$

g_0 will be purely real for any velocity if $\delta\phi_1(t) = \delta\phi_2(t)$. If they are not equal, the slight velocity-dependence of the phase of g_0 will be insignificant compared to $\phi_{\rm err}$ due to Imperfection 3 (the unequal strength of the choppers). Furthermore, if we are using the second method of measuring $\phi_{\rm err}$, the velocity dependence is already included.

3.6.5 Imperfection 5: Effect of chopper transit time on the time-dependent phase

Because it takes an atom a finite time to pass through the gradient field region, the total time-dependent phase applied by the chopper will be averaged over the transit time. If the transit time is slow compared to the chopper period, the electric field will pulse many times in transit, and the phase picked up by the atom will be smeared out in time, destroying the ramped phase necessary for the rephasing technique to work. To quantify this, we need to calculate the effect this has on the interference pattern as a function of the velocity, the ramp frequency, and the physical size of the gradient field region.

We must first calculate the phase acquired as a function of the transit time while passing the chopper wire. This was done previously in Section 3.2.4. If the wire voltage is static, then the difference in potential energy $\Delta V(t)$ experienced by the two paths of the interferometer (as a function of the transit time, t) is

$$\Delta V(t) = \phi_0 \frac{2\hbar v}{\pi r} \frac{1}{(1 + t^2 v^2/r^2)^2} \tag{3.81}$$

where ϕ_0 is a constant chosen such that $\int \frac{1}{\hbar} \Delta V(t) dt = \phi_0$ is the total phase acquired, and r is the wire radius, and v is the velocity.

Now assume the intended applied phase, ϕ_0, is not static. Then the actual phase acquired by an atom is the convolution of the chopper signal, $\phi_0(t)$, with the transit time, t':

$$\phi_{\text{conv}}(t) = \int_{-\infty}^{\infty} dt' \, \phi_0(t + t') \frac{2v}{\pi r} \frac{1}{(1 + t'^2 v^2/r^2)^2} \tag{3.82}$$

Since we are adding up differential phases, it now matters whether $\phi_0(t) = \omega t$ is a continuous function versus one that returns to zero when it reaches 2π—the former gives $\phi_{\text{conv}}(t) = \omega t$ no matter how slow the velocity, the latter averages to π at very slow velocity. We are using one that returns to zero periodically—it can be

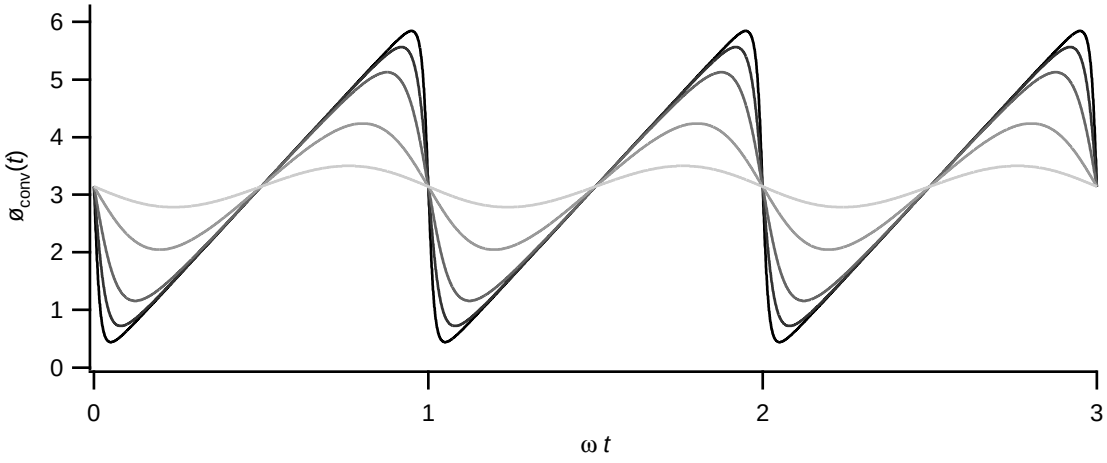

Figure 3-15: The time-dependent ramping phase applied by a chopper is damped out when the transit time past the wire grows comparable to the ramp period. $\phi_{\rm conv}(t)$ is plotted for different ramp frequencies (from darker to lighter), $f = 50$ kHz, 100 kHz, 200 kHz, 500 kHz, and 1 MHz, assuming a $\frac{1}{2}$ mm radius wire and a 1 km/s beam velocity. The rephased contrast attainable with these waveforms is 90%, 81%, 63%, 25%, and 3%, respectively.

represented by the expansion:

$$\omega t = \pi - \sum_{n=1}^{\infty} \frac{2 \sin n\omega t}{n} \qquad \text{for } 0 < t < 2\pi/\omega \tag{3.83}$$

Using this expression in Eq. 3.82, we find

$$\phi_{\rm conv}(t) = \pi - \sum_{n=1}^{\infty} e^{-n\omega r/v}(1 + n\omega r/v)\frac{2 \sin n\omega t}{n} \tag{3.84}$$

Fig. 3-15 shows how $\phi_{\rm conv}(t)$ gets smeared out as $\omega r/v$ grows large.

The damping will effect the rephased interference pattern by increasing the size of $\delta\phi(t) = \phi_{\rm conv}(t) - \omega t$ and hence lower the contrast:

$$C = \left| \langle e^{i\delta\phi(t)} \rangle \right|^2 \tag{3.85}$$

Fortunately, there is no change to the phase of the rephased fringe so long as the phase of the two choppers is the same, for the same reasons discussed for Imperfection 4.

Error Source	Systematic Error	Statistical Error
Velocity, v_0		0.12%
Grating period	0.05%	
Grating-to-detector distance	0.06%	
Velocity distribution, $P(v)$	0.15%	
Interaction phase, $\phi_{\text{int}}(v_0)$		0.15%
Septum spacer width, d	0.07%	
Septum length, ℓ	0.08%	
Septum field correction, $\ell_{\text{effective}}/\ell$	0.10%	

Table 3.2: Relative contributions of the various error sources in the old measurement of sodium polarizability [33].

3.6.6 Summary

The imperfections discussed in this section impose very few limitations on how accurately the polarizability can be measured. Most errors contribute only to loss of contrast. The only source of systematic error, due to the unequal strength of the chopper phases, can be corrected by the measurement techniques mentioned without a significant increase in measurement time.

3.7 Accuracy of the Polarizability Measurement

3.7.1 Old Limitations

We now return to a discussion of the advantages of the rephasing method. The limitations that are overcome by using the rephasing method are quite substantial. The phase measurement can now be performed at a precision of 10^{-5} (or 0.001%): using the technology demonstrated in this chapter it is possible to attain a 1.5 mrad statistical error (requiring one hour of measurement time using the estimate in Section 3.5) in a 150 rad interaction (demonstrated in Fig. 3-11). The error budget from the previous polarizability measurement is shown in Table 3.2. The beauty of the rephasing method is that it eliminates the first four errors. The remaining errors are related to the geometry of the interaction region. We will discuss how to overcome this limitation below.

3.7.2 Molecules

We need to consider another very important source of error that was not mentioned at all in the old experiment: the presence of Na_2 molecules in the beam. Since the molecules have an average polarizability about 1.5× that of the atoms, any fraction of molecules in the interference pattern will cause a fractional error in polarizability. The molecules typically compose 20% of the beam intensity, but the fraction is much smaller in the interference pattern because the molecule paths only separate by half the distance of the atom paths, and don't easily fit around both sides of the septum. The dimensions quoted in the old experiment were an atom separation of 55 μm (corresponding to 27.5 μm for the molecules) and a septum "shadow" of 20–30 μm. If they were lucky, and the shadow was 30 μm, then molecule interference would be impossible even for the slowest molecules of the distribution. A more likely scenario is that about 10% of the 40 μm wide (FWHM) molecule beam got past both sides of the septum to interfere at the detector. This would result in a 2% intensity of molecules in the fringe, causing an error of order 2% in the phase and hence the polarizability. If the polarizability is measured at many different phases the error ought to on average cancel out, since the sign of the error is different at different phases. In the old experiment however only a small number of different phases were measured, with a select few having much greater weight.

Fortunately, measuring polarizability with the new method is not susceptible to contamination by molecules. Since they have a different polarizability, they will have a different rephasing condition than the atoms and won't contribute any contrast to the atom rephasing peak. The chopping voltages won't be optimized for the different polarizability either. Molecules will be present when measuring the zero phase, but with the same phase as the atoms.

We should consider, though, that the molecules have a range of polarizabilities, and even if molecules with their average polarizability are not present in the rephasing peak, molecules with a polarizability closer to that of the atoms may be a problem. Molecules have an anisotropic polarizability, characterized by two values, $\alpha_\perp$, the

polarizability when the electric field is perpendicular to the molecular axis, and $\alpha_\parallel$, the polarizability when the field is parallel. Classically, the molecule can be at any angle θ with respect to the field, in which case

$$\alpha(\theta) = \alpha_\perp + (\alpha_\parallel - \alpha_\perp)\cos^2\theta \tag{3.86}$$

For Na_2, $\alpha_\perp = 29.2 \times 10^{-24}$ cm^3 is the minimum and $\alpha_\parallel = 55.6 \times 10^{-24}$ cm^3 is the maximum that the polarizability could be [68] (the average is $\bar{\alpha} = 38.0 \times 10^{-24}$ cm^3). $\alpha_\perp$ is fairly close to the value for atoms, $\alpha = 24.1 \times 10^{-24}$ cm^3. The rms width of a rephasing peak in terms of frequency is:

$$\sigma_f = \frac{v_0^2}{2\pi L \sigma_v} \tag{3.87}$$

which is 3 kHz assuming $v_0 = 1$ km/s, $L = 1$ m, and $\sigma_v/v_0 = 0.05$. So to be careful, we should make sure the atom rephasing peak is at least $3\sigma_f$ away from the lowest molecule rephasing peak to avoid contamination. In this example it means the rephasing frequency should be larger than 45 kHz. Alternatively, we could make sure the septum is too wide to allow molecule interference.

In addition to molecule interference, we ought to also consider the contamination from other interfering orders, for instance, two paths that both pass on the outside or inside of the septum and interfere in the detector plane. This was a big consideration in the index of refraction measurements, so we can't ignore it in a precision measurement of polarizability. The best way to combat the problem is to block out the extra orders with a knife edge before they propagate back together and interfere near the detector. This can be easily accomplished by attaching tabs to the front of the interaction region that block everything within a certain distance of the septum. Even if the problem can't be eliminated, it can be dealt with in many ways. First, it influences the zero-phase and rephased fringe measurements equally so it won't introduce any error if the rephased contrast is the same as the zero-phase contrast.

Second, the systematic error will change sign if the septum voltage is reversed[7] (to attain rephasing the chopping phase can be time-reversed)—this should be done anyways to test for contact potentials. Third, it would manifest itself as a periodic warp in the otherwise linear plot of ϕ vs V^2. Finally, it would also show up as a dependence on the detector position.

3.7.3 New Limitations

The rephasing method introduces only two significant sources of new error. One is the inter-chopper distance, measurable to 10^{-4} by conventional means, 10^{-5} if the separation was set by a precision spacer, or even greater precision if measured interferometrically. The second is the chopper phase error, $\phi_{\rm err} = \langle |\phi_1(t)| - |\phi_2(t)| \rangle_t$ (Eq. 3.76), which can be measured in a fraction of the time it takes to measure the polarizability phase or eliminated altogether by use of a waveform generator at two different frequencies.

If we were to really push the limitations of the rephasing method, we would eventually reach one of the following boundaries:

1. Maximum phase attainable with the interaction region. The vacuum breakdown voltage is 125 kV/mm, however glass can only support 3.5 kV/mm, and the best insulators only 20 kV/mm [63]. It could also be difficult to measure such large voltages with precision. For comparison, a 1 km/s beam in a 10 cm long, 1 kV/mm field picks up a phase of 1300 radians.

2. Chopper-transit-time limitation on the maximum chopping frequency. The smallest we could make the wire radius is about 200 μm—at this radius we would suffer a 20% loss in contrast due to phase spread across the beam width. The maximum frequency could then be pushed up to about 250 kHz for a 1 km/s beam, where another 20% of the contrast would be lost due to the

[7] The possibility of unwanted interfering orders was not considered in the old experiment, however, this test was performed and showed no systematic effect.

chopper-transit-time limitation. The limitation on the rephasing frequency at this velocity corresponds to a maximum interaction phase of 1600 radians.

3. Limitations of the high voltage equipment. The high voltage signal generator that we currently use to drive the choppers has a power dissipation limit of $P = V^2 f C = 100$ Watts, where V is the voltage, f is the frequency, and C is the capacitance. The capacitance, which includes capacitance in the connecting wires and internal to the driver, is about 150 pF. Operating at the limit, the high voltage supply for the signal generator would need to be able to supply 100 W as well. Use of a 200 μm radius wire, however, would lower the voltage required for the choppers and extend the maximum operating frequency well past 250 kHz. Use of an amplified arbitrary waveform generator may impose stricter limitations on the frequency.

4. Phase spread from the interaction region. Rephasing solves the problem of different velocities getting different phases, but atoms passing by at different spatial locations from the septum see different phases as well. There is a 1% variation in phase across the width of a 30 μm wide beam if guard electrodes are not used. The edges of the septum foil must be made very parallel as well. If the edges of a 4 cm interaction region are 10° off, atoms at the top of the 1 mm tall beam will see phase different by about $\frac{1}{2}$% compared to atoms at the bottom.

These effects limit the rephasing technique to a maximum interaction phase of about 1500 rad. With our current statistical phase error (estimated at 1.5 mrad in one hour of measurement time), this limits us to a precision of 10^{-6} in a polarizability measurement. To surpass this limitation, the interaction region would need to be made much longer and the gradient fields replaced with some type of smaller-sized interaction that would not cause contrast loss at high frequency.

3.7.4 Overcoming Geometry Errors

Uncertainty in the geometry of the interaction region, and hence the integral of E^2, is the single biggest obstacle to an improved absolute measurement of polarizability. There are two ways to overcome this problem. One involves constructing and characterizing the dimensions of a new interaction region to the desired precision. The other, discussed in the next section, is to perform a relative measurement by measuring the polarizabilities of two different atoms using the same interaction region. Each individual measurement of polarizability may be in error, but the ratio of polarizabilities would be exact.

The polarizability is proportional to $d^2/\ell \times (\ell/\ell_{\text{eff}})$, where d is the separation of the plates in the interaction region, and ℓ is the length of the interaction region (or the distance between guard electrodes), and ℓ/ℓ_{eff} is the ratio that the effective length differs by the actual length. An improved measurement of the absolute polarizability must improve the precision of all three of these parameters.

d will have to be measured interferometrically. This can be accomplished by replacing the aluminum walls of the septum with half-silvered mirrors. A beam of light incident perpendicular to the wall will reflect off both the septum foil and the mirror, causing interference in the reflection. The interference can be mapped as a function of wavelength to determine d. Knowing d to $\frac{1}{10}$ of a wavelength (out of 2 mm) will provide better than 10^{-4} precision in d^2.

ℓ can be improved by updating the interaction region design, too. The guard electrodes define the physical length of the interaction region, so their separation should be set with a precision spacer. 1 μm precision in a 10 cm separation would give 10^{-5} precision in ℓ.

Calculating the ratio ℓ/ℓ_{eff} is done by modeling the electric fields inside the interaction region to compensate for the fact that though the electric field is constant on the inside, it falls off gradually over a distance d at the edges. ℓ/ℓ_{eff} can be improved by better numerical modeling of these edge effects, as long as *all* the dimensions of the interaction region are well characterized. This includes the separation between

the guard electrodes and the foil, and the length of the guard electrodes and the length of the foil. Better construction would help, too. A third of the error in old model was due to characterizing fields seen by the beam passing on the zero-field side of the septum, which could be eliminated by making the foil and guard electrodes longer. The interaction region might need to be taller as well. The old model was two dimensional and did not take into account how the fields varied in the vertical direction. This should be modeled first, but it is quite probable that the fields vary by a significant amount in the vertical direction, since the height of the interaction region is only $\sim 5\times$ larger than d.

A new design for the interaction region can eliminate the dependence on ℓ/ℓ_{eff} altogether by duplicating the effect on both sides of the septum, thus cancelling the error in the phase difference (Fig. 3-16). The interaction voltage would be applied to both sides, but the length of the electric field region is made much shorter on one side. Each side has exactly the same edge effects, so the end field corrections cancel out. The total phase acquired in the interaction region is

$$\phi_{\text{int}} = \frac{\alpha V^2}{2d^2\hbar v}(\ell_1 - \ell_2) \tag{3.88}$$

where $\ell_{1,2}$ is the actual separation between the guard electrodes on either side. The only influence of the end effects would be a slight dependence of the phase on the position inside the interaction region, about 2×10^{-5} per μm of distance from the septum (see Ref. [34], Fig. 6).

There is one new systematic error that arises when we require a larger interaction phase and better geometrical precision. It is the effect of the large electrostatic forces present in the interaction region at large applied voltage. The septum is a thin foil held in place by a force $T \approx 0.1$ N/cm (within an order of magnitude) along the top and bottom edges of the foil. The electrostatic force between two metal surfaces a distance d apart with a difference in potential V causes an electrostatic pressure $P = \frac{1}{2}\epsilon_0 V^2/d^2$ where $\epsilon_0 =(8.89\ \text{N/m}^2)\text{kV}^{-2}\text{mm}^2$. Contrary to intuition, the pressure is positive (the surfaces repel) if they remain held at fixed potential. If the height of

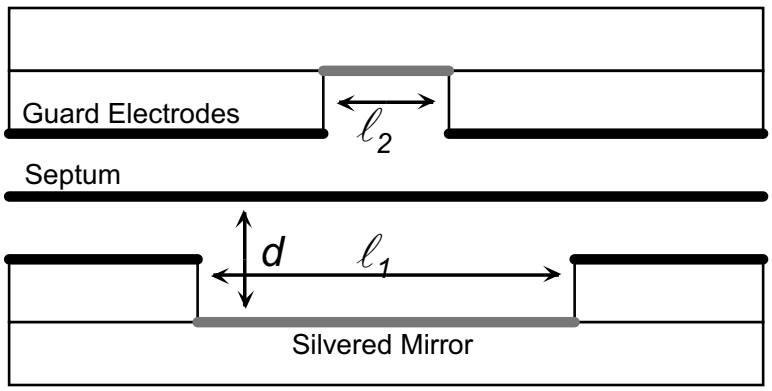

Figure 3-16: Schematic showing the new features of an improved interaction region. Black surfaces are at ground and grey surfaces are at high voltage. The septum has been made much longer than ℓ and the guard electrodes have been extended. The high voltage plane consists of a charged, partially-silvered surface that can transmit light for an interferometric measurement of d. The ground side of the interaction region has a small length that is at high voltage to cancel out the hard-to-model end effects. (The schematic exaggerates the vertical dimensions; in reality $d \ll \ell$.)

the foil from top to bottom is $h = 1$ cm, the foil will sag due to electrostatic pressure by a distance $\Delta d \approx h^2 P/T$. For $d = 2$ mm and $V = 1$ kV, this is a displacement of about 10 μm, or an error of 10^{-2} in d^2. To make matters worse, T might be overestimated. T is an estimate of the spring forces used to pull the foil tight. During assembly the foil is clamped into place and the spring tension is relaxed. It has been observed that the foil doesn't keep its full tension, since it ends up less smooth without the springs. A future design could incorporate springs that always keep the foil at maximum tension. This would help make the septum shadow thinner as well. The only other way to overcome this problem is by making ℓ much longer, so that less voltage is required for the same amount of phase.[8]

There is one other method for overcoming *all* the errors due to geometry, and this is to measure the fields inside the interaction region directly. Metcalf and collaborators at Stony Brook have made direct measurements of electric fields at the 2×10^{-6} level

[8]This error was not considered in the old experiment. α was determined with the strongest contribution from measurements taken at around 300 V. Sag at this voltage causes an estimated error of 10^{-3}, which could have been even worse if tension was lost during assembly.

[90, 91] and have mapped regions of electric field to 7×10^{-5} with a three-dimensional resolution of 250 μm [105]. It would be very fruitful to form a collaboration with a group that can perform such measurements. This would completely bypass the need for refining the construction and measurement of the interaction region geometry.

3.7.5 Relative Measurement of Polarizability

The parameter d^2/ℓ does not need to be determined with precision at all if we take a different approach to measuring α—measuring the *relative* polarizability. If the polarizability of two different atoms is measured with the same interaction region, the ratio of their polarizabilities will be known very precisely, even if the interaction region is not.

We will propose a relative measurement of the polarizabilities of sodium and cesium. We choose sodium because its absolute polarizability has been measured already, and cesium because it is the most desirable to the physics community. Cesium is the most important test bed for parity non-conservation in atomic physics, and these tests require detailed calculations of cesium's electronic wavefunction. The validity of the theoretical calculations can only be verified by testing their predictions against actual measurements of atomic properties, and polarizability, describing an atom's response to an electric field, is the most important parameter that can be used to characterize an atomic wavefunction.

The polarizabilities of Na and Cs can both be measured using the techniques in this chapter:

$$\begin{aligned} \alpha_{\mathrm{Na}} &= f_{\mathrm{Na}} \left(\frac{d^2}{\ell}\right) 2hL/V^2 \\ \alpha_{\mathrm{Cs}} &= f_{\mathrm{Cs}} \left(\frac{d^2}{\ell}\right) 2hL/V^2 \end{aligned} \tag{3.89}$$

While both of these measurements are dependent on many parameters that may be known with limited precision (primarily d^2/ℓ), the ratio of polarizabilities depends

only on the ratio of the rephasing frequencies:

$$\alpha_{\mathrm{Cs}}/\alpha_{\mathrm{Na}} = f_{\mathrm{Cs}}/f_{\mathrm{Na}} \tag{3.90}$$

For improved accuracy, we have chosen a slightly different way of measuring the rephasing condition than the method outlined earlier—we keep the interaction voltage fixed in both measurements and find the chopper *frequency* at which the revival occurs.[9]

By measuring the ratio of polarizabilities in this manner, we eliminate all the error due to uncertainties in geometry, including the strain induced by electric fields as a function of voltage. Furthermore, we also eliminate the error in the distance between choppers L, and the interaction region voltage V. (Even h, for that matter, if the measurement is ever taken past the part-per-million level.)

The only errors that contribute to the ratio measurement involve how well the rephasing conditions can be determined. This error comes from two sources, the unequal strength of the chopper phases, $\phi_{\mathrm{err}} = \langle|\phi_1(t)| - |\phi_2(t)|\rangle_t$ (Eq. 3.76), and the statistical error involved in determining the rephasing conditions, due to the number N and the statistical phase error ϕ_{stat} of the interference fringe measurements: [10]

$$\Delta f_{\mathrm{reph}} = \Big(\frac{\phi_{\mathrm{err}} + \phi_{\mathrm{stat}}/\sqrt{N}}{\phi_{\mathrm{int}}}\Big) f_{\mathrm{reph}} = \frac{v_0}{2\pi L}(\phi_{\mathrm{err}} + \phi_{\mathrm{stat}}/\sqrt{N}) \tag{3.91}$$

The only new difficulty involved in a relative measurement of two polarizabilities is making the interferometer work for two different atoms. For cesium, the difficulty is due to its large mass (5.8× that of sodium), and hence its very small de Broglie wavelength. Even in our 100 nm grating interferometer, a 1000 m/s cesium beam

[9] There is no extra effort in doing this if an arbitrary waveform generator is used. It should even be possible using the filtered square wave, by swapping the RC values to duplicate the voltage waveform at a different rephasing frequency.

[10] For very high precision measurements, there may arise an additional dependence on geometry due to the unequal path separations of the two atoms inside the septum. There is a slight difference in $\ell_{\mathrm{effective}}$ depending on how far the beam is from the septum. Surprisingly, this amounted to a relative change of only about 2×10^{-6} per μm of septum displacement as modeled in the old experiment (see Ref. [34], Fig. 8).

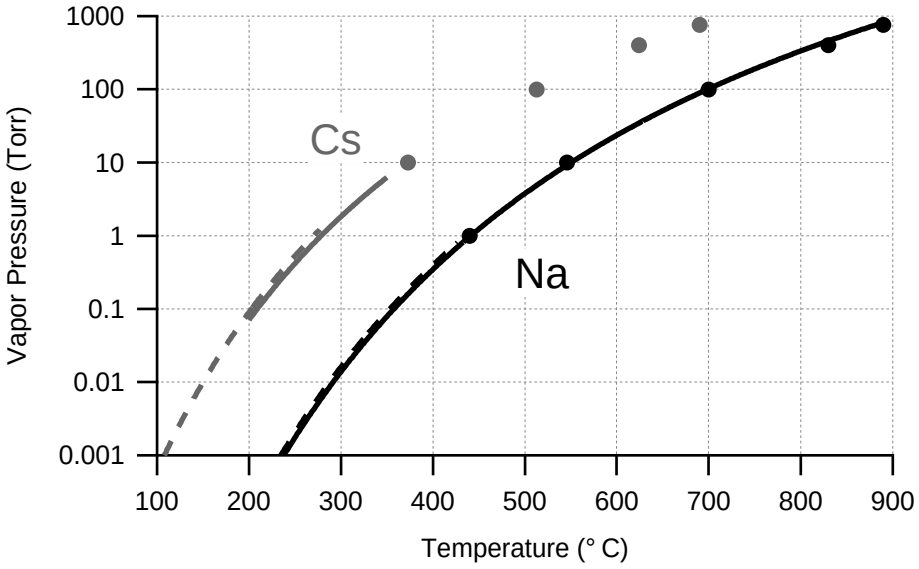

Figure 3-17: Vapor pressure of sodium and cesium as a function of temperature, from various sources in the CRC Handbook of Chemistry and Physics. Sodium melts at 97.8°C and boils at 882.9°C. Cesium melts at 28.4°C and boils at 678.4°C.

will have a path separation of only 27 μm, which is not wide enough to fit around both sides of the septum. With sufficient innovation the septum could be constructed with half its current thickness of 30–40 μm, although no matter how thin it was made intensity would still be lost, since the path separation isn't larger than the 40 μm (FWHM) beam profile.

Alternatively, the cesium interferometer can be made to work by going to a smaller beam velocity. The usual way to do this with a supersonic beam is to use a carrier gas with a larger mass. Unfortunately, the largest rare gas atom we can use is xenon, which gets us only as low as 700 m/s. This will not be low enough to get good path separation with cesium, so we will consider using a thermal, or effusive, atomic beam source. With an effusive source, the 70 μm aperture in the source could be opened up to the vertical collimation height of 1 mm for an order of magnitude increase in intensity. (We have explored this by using extremely low pressures in our sodium supersonic source—with the aperture in place, the effusive intensity is $\frac{1}{2}$ the Ar-seeded intensity and $\frac{1}{24}$ the He-seeded intensity.)

The relative intensity, I, of an effusive beam depending on the atom is:

$$I \propto P(T)\, T^{-\frac{5}{2}}\, m^{\frac{3}{2}}\, v^3\, e^{-\frac{1}{2}mv^2/k_BT} \tag{3.92}$$

where we have included all the parameters that depend on the particular atom, namely the vapor pressure $P(T)$ (see Fig. 3-17) and the mass m.[11] Using this we can compare the intensities as a function of velocity for sodium and cesium at a given temperature (Fig. 3-18). We will assume these are the intensities of the interference amplitude. Then we can ask how the velocity distribution is modified by the presence of the septum between the interfering paths. For the cesium distribution, interference is not possible at high velocity. For lower velocities there is a loss of interfering counts because the paths are not physically separated. Sodium, on the other hand, is unaffected by the septum at these velocities. Since there is more intensity in the cesium beam to start with, the signal is still better than sodium even though the velocity distribution is severely clipped by the septum.

The modifications required for measuring cesium could be as minimal as simply adding some cesium to the sodium source. The seed pressure could be lowered or eliminated to get a thermal beam—the only danger is the potential clogging of the nozzle (which could simply be enlarged a bit). This would create a beam consisting of both sodium and cesium. The ratio could be adjusted by the source temperature. One nice feature of the rephasing method is the ability to make measurements of two polarizabilities simultaneously without fear of either measurement influencing the other. With no applied interaction, the two species have the same phase interference pattern; with the interaction, only one species can rephase at a time. Operation of the choppers for cesium instead of sodium requires minor changes. The phase applied by a chopper is proportional to α/m (larger m means smaller path separation, hence smaller chopper phase). To compare, $\alpha_{\rm Cs}/m_{\rm Cs} = (0.428)\,\alpha_{\rm Na}/m_{\rm Na} = 3.01 \times 10^{-14}$ volt^{-2} s^{-2} m^4, so the chopper voltage needs to be increased by 50% for use with

[11] A useful value to use here is $k_B = 8314.47$ amu m^2 s^{-2} °K^{-1}. To find the wavelength at a given velocity ($\lambda_{dB} = h/mv$) another useful value is $h = 3990.31269$ amu m s^{-1} Å.

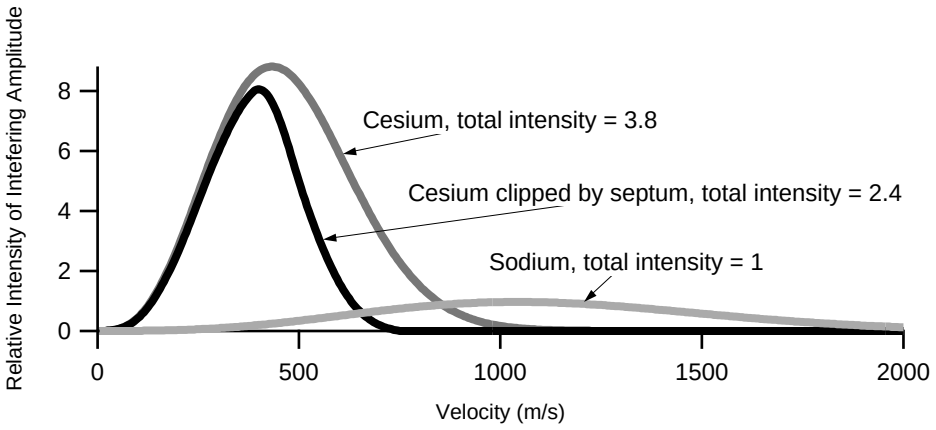

Figure 3-18: Velocity distribution of thermal beams of sodium and cesium at 1000 °K. The cesium has a total of 3.8× more intensity due to its higher vapor pressure. Also shown is the effect of inserting a septum into the cesium interferometer. This reduces the intensity that contributes to interference—at high velocity the paths can't fit around the septum. We have assumed a 40 μm wide septum and a trapezoidal beam profile made 1 m downstream by 15 μm slits spaced 1 m apart. The septum is centered 35 μm off the 0^{th} order for optimum fit between the paths.

cesium.

A prediction of simultaneous rephasing is shown in Fig 3-19. The rephasing scheme works even better with the wider velocity distribution of a thermal beam—the larger the rms velocity, the narrower the rephased frequency peak, and the smaller the contamination from unwanted neighboring rephasing peaks. Measuring α in this example is much easier for cesium than for sodium: cesium has a higher intensity, the interaction phase is larger since the polarizability is larger, and the mean velocity is much slower creating a steeper phase slope with which to measure the rephased frequency.

3.8 Other Uses of The Rephasing Method

We have demonstrated how the rephasing technique can overcome decoherence due to the velocity-dependent polarizability phase. Of course, the technique will work just as well for any type of velocity-dependent phase proportional to $1/v$. In fact, the technique can be used to rephase any velocity-dependent phase $\propto 1/v^{\gamma}$ for any

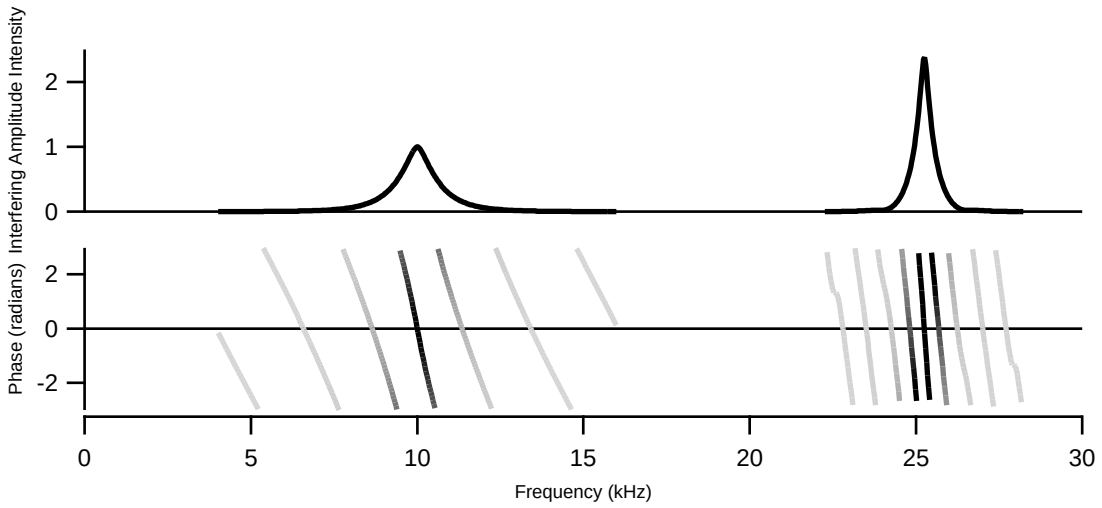

Figure 3-19: Simultaneous measurements of sodium and cesium polarizability, for an interferometer consisting of both the sodium and clipped cesium distributions in Fig. 3-18. The interaction region voltage is chosen so that sodium has a rephasing frequency of 10 kHz. At this voltage, cesium rephases at a frequency 2.5× higher. The phase is no longer a straight line due to the asymmetry of the (inverse) velocity distribution.

γ. If $\phi_{\max}(v_0)$ is the largest $1/v^\gamma$-dependent phase that can be applied without significant contrast loss, the rephasing technique can extend the maximum phase to approximately $(v_0/\sigma_v) \times \phi_{\max}(v_0)$ before seeing the same amount of decoherence. The technique doesn't even have to be limited to de Broglie wave interferometers—it could be used in a white-light optical interferometer to overcome contrast loss inside a dispersive medium.

We will briefly give two examples of new applications of the rephasing technique in an atom interferometer: the "Sagnac" phase induced by a rotation, and a "non-white-fringe" interferometer. Both involve phases proportional to the inverse-velocity.

3.8.1 Rotation Phase

Rotating an atom interferometer induces a Sagnac phase proportional to the area, A, enclosed by the paths of the interferometer. Because the diffraction angle is

proportional to the de Broglie wavelength, the Sagnac phase is linear in $1/v$:

$$\phi_{\text{rotation}} = 2mA\Omega/\hbar = 4\pi\frac{L_{\text{int}}^2\Omega}{\lambda_g v} \tag{3.93}$$

where Ω is the rotation rate (radians per unit time), L_{int} is the inter-grating distance, and λ_g is the grating period. No matter how large the rotation phase is, any contrast loss can be recovered by using the rephasing technique with frequency f and length L such that

$$fL = 2L_{\text{int}}^2\Omega/\lambda_g. \tag{3.94}$$

Typically, the operation of a Sagnac gyroscope involves feedback in which a counter-rotation is applied to keep the interferometer phase constant, and hence no dephasing occurs. However, the rephasing technique could still be useful as a method of implementing the feedback by modulating the pulse frequency in proportion to the error signal. The advantage is that no counter-rotation is necessary, and the feedback is purely electronic.

Turning things around a little, there is actually a correspondence between the Sagnac phase and the phase of the choppers that we can explore to gain some insight into how the rephasing technique works. We will show how we can describe the rephasing method as an effective rotation of the interferometer.

First, we must show how the Sagnac phase is produced in the interferometer, which can be predicted from the phase dependence on the position of the gratings. The rotation phase doesn't depend on where the axis of rotation is, so a constant rate of rotation Ω of the interferometer is equivalent to fixing the position of Grating 2 and translating Gratings 1 and 3 (each a length L_{int} from Grating 2) with equal and opposite velocities, $\pm s = \pm L_{\text{int}}\Omega$. The phase of the interferometer depends on the position of the gratings (with period λ_g) as $\phi = 2\pi(x_1 - 2x_2 + x_3)/\lambda_g$, so the rotation can be thought of as changing the phase of the interferometer with time dependence $\phi_1(t) = 2\pi st/\lambda_g$ and $\phi_3(t) = -2\pi st/\lambda_g$. For an atom with velocity v traveling through the interferometer, there is a time delay of $2L_{\text{int}}/v$ between the phases seen at Gratings 1 and 3. The rotation phase is the sum of the phases at

Gratings 1 and 3:

$$\phi_{\text{rotation}} = \phi_1(t) + \phi_3(t + 2L_{\text{int}}/v) = 4\pi \frac{L_{\text{int}}^2 \Omega}{\lambda_g v}. \tag{3.95}$$

Expressed in this manner, the rotation phase is equivalent to our ramped-phase technique, if we identify the chopper phases as applied by Gratings 1 and 3 at a length $2L_{\text{int}}$ apart. The chopper frequency is s/λ_g, the inverse of the time it takes for the phase to change by 2π, i.e. for grating to move a distance equal to the grating period.

The correspondence between the Sagnac phase and the chopper phase provides us with an alternate method of implementing the rephasing technique. Instead of using the electric field gradient regions, we could translate Gratings 1 and 3 to apply the time-dependent phase instead. We do not have to physically rotate the whole interferometer to create the grating motion; we can translate Gratings 1 and 3 individually with piezo actuators. They only need to travel a distance λ_g before returning to their original positions, and as we showed in Section 3.6, the repetition of the motion at a precise frequency makes up for any imprecision due to positioning errors of the gratings (due to hysteresis, for instance). For an interferometer with gratings made of light, the implementation would be even simpler, requiring only a modulation of the phase of the laser light to change the phase of the atoms.

3.8.2 Rephasing a "Non-White-Fringe" Interferometer

There are many pairs of paths in our interferometer that would interfere with each other if our beam was monochromatic, i.e. at a single velocity. These paths don't interfere because their path difference is more than the coherence length of the beam. The extra path length in one arm produces a phase difference between the two paths that depends on the velocity of the atom, and its interference pattern is washed out due to the spread of velocities in the beam. With the rephasing technique we can correct the velocity-dependent phase difference, creating a "white-fringe" interferometer where atoms of all velocities contribute to the interference pattern with the same phase.

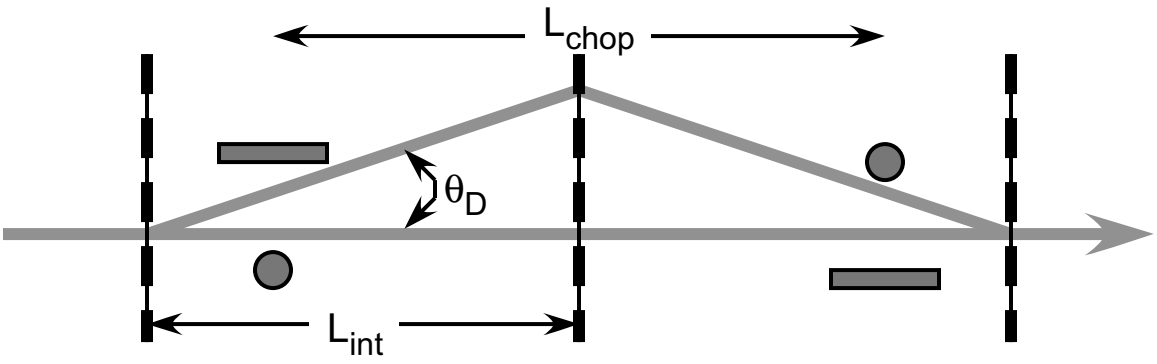

Figure 3-20: There will be no interference if the path difference of the unequal arms is longer than the coherence length in this interferometer. The rephasing technique can recover the washed out interference pattern.

Consider the interference between the two paths in Fig. 3-20. The difference in path length is $\Delta\ell = L_{\rm int}\theta_D^2$, where $\theta_D = \lambda_{dB}/\lambda_g$ is the diffraction angle (λ_{dB} is the de Broglie wavelength of the atom). The difference in phase is:

$$\Delta\phi = 2\pi\Delta\ell/\lambda_{dB} = 2\pi\frac{L_{\rm int}\lambda_{dB}}{\lambda_g^2} \tag{3.96}$$

Since the de Broglie wavelength is proportional to the inverse velocity, $\lambda_{dB} = h/mv$, so is the phase difference:

$$\Delta\phi(v) = 2\pi\frac{hL_{\rm int}}{m\lambda_g^2}\,\frac{1}{v} \tag{3.97}$$

Our rephasing technique will work perfectly to rephase the mismatched-path interferometer. The condition for rephasing is $\Delta\phi(v) = 2\pi f_{\rm chop}L_{\rm chop}/v$. For typical parameters in our interferometer, $L_{\rm int} = 1$ m and $\lambda_g = 200$ nm, the phase due to the path difference is $2\pi \times 435$ radians. The interferometer will rephase at chopping parameters of $L_{\rm chop} = 1$ m and $f_{\rm chop} = 435$ kHz. For a grating period of $\lambda_g = 100$ nm, the rephasing frequency is even higher: $f_{\rm chop} = 1.74$ MHz.

One interesting possibility for the rephasing of these interferometer paths is a precision measurement of h/m, one of the key constants necessary for a precision measurement of the fine structure constant using atomic physics. To do this, we combine the rephasing of these paths with the implementation of Gratings 1 and 3

as choppers as described above. Then $L_{\text{chop}} \equiv 2L_{\text{int}}$ and the rephasing condition becomes:

$$2\pi \frac{hL_{\text{int}}}{m\lambda_g^2 v} = 4\pi \frac{f_{\text{chop}} L_{\text{int}}}{v} \tag{3.98}$$

Now, both the velocity and the length cancels out, but the value h/m still depends on the grating period, which is far from a precision quantity in our interferometer. However, the gratings can be made using a standing wave of laser light instead, in which case the period is $\lambda_g = c/\nu$ where ν, the laser frequency, is very precise. h/m then depends only on two well-known quantities, f_{chop} and ν:

$$h/m = 2c^2 f_{\text{chop}}/\nu^2 \tag{3.99}$$

In addition to f_{chop} and ν, the precision of h/m depends on one more thing—the precision with which the phase of the rephased interferometer can be measured. With a slow beam of hydrogen ($v = 100$ m/s) we could have $\Delta\phi \approx 10^5$, which would give a part-per-billion measurement if the phase were measured to 0.1 mrad. Some of the benefits of this method of measuring h/m are that the measurement doesn't depend on the transit time between different parts of the interferometer, that the laser need not be resonant with the atom used, and that the atomic beam can be thermal and need not be collimated.

Appendix A

Glory Oscillations in the Index of Refraction for Matter-Waves

The following paper has been submitted for publication in Physical Review Letters. It can also be found in the LANL preprint archives at lanl.arXiv.org/abs/physics/0203008.

Glory Oscillations in the Index of Refraction for Matter-Waves

Tony D. Roberts, Alexander D. Cronin, David A. Kokorowski, David E. Pritchard
Massachusetts Institute of Technology, Cambridge, Massachusetts 02139
(Dated: February 26, 2002)

We have measured the index of refraction for sodium de Broglie waves in gases of Ar, Kr, Xe, and N_2 over a wide range of sodium velocities. We observe glory oscillations—a velocity-dependent oscillation in the forward scattering amplitude. An atom interferometer was used to observe glory oscillations in the *phase shift* caused by the collision, which are larger than glory oscillations observed in the cross section. The glory oscillations depend sensitively on the shape of the interatomic potential, allowing us to discriminate among various predictions for these potentials, none of which completely agrees with our measurements.

PACS numbers: 03.75.Dg, 07.60.Ly, 34.20.Cf, 34.20.Gj
Keywords:

A singularity in the classical differential scattering cross section $\frac{d\sigma}{d\Omega} = \frac{b}{\sin\theta}|\frac{d\theta}{db}|^{-1}$ arises when $\theta(b_{\rm glory}) = 0$ or π at finite non-zero impact parameter, b_{glory}. This was named glory scattering by B. Cellini who observed the resulting circle of back-scattered light around the shadow of his head on the dewy grass. An even brighter glory can be observed surrounding the shadow of one's airplane on the clouds of spherical water droplets below [1].

Glory scattering is not just an optical phenomenon. Interatomic potentials are attractive at long range but have repulsive cores. Hence there is an impact parameter just beyond the potential minimum for which $\theta(b_{\rm glory}) = 0$. Quantum mechanics demands that atom-atom scattering be treated as a wave phenomenon, but when the de Broglie wavelength is much smaller than the potential, the semiclassical approximation can be used [2] in which the incident wave is viewed as traveling along classical paths. There are then two possible paths to scatter into the forward direction—a long range diffractive component from large b, and the aforementioned path near the potential minimum. Waves from these paths contribute to the scattering amplitude in the forward direction, $f(k, \theta = 0)$, for which the partial wave treatment reads:

$$f(k,0) = \sum_{l=0}^{\infty} \frac{2l+1}{2k} \sin 2\delta_l + i \sum_{l=0}^{\infty} \frac{2l+1}{k} \sin^2 \delta_l, \quad (1)$$

where the sums are both real.

The behaviors of the real and imaginary parts of $f(k, 0)$ are different. Imf (the second sum in Eq. 1) has a large value owing to the fact that $\sin^2\delta$ averages to $\frac{1}{2}$ where the scattering is strong ($\delta \gg \pi$). The contributions from large l and l_{glory} add on top of this large value, making Imf less sensitive to the shape of the potential. On the other hand, the strong scattering region contributes zero on average to Ref, and the long range and glory contributions can either add or subtract, making it easier to discern effects from each region as well as their relative phase.

The ratio,

$$\rho(k) \equiv \frac{\mathrm{Re}f(k,0)}{\mathrm{Im}f(k,0)}, \quad (2)$$

has been shown to give information about the rate of increase of the interatomic potential $V(r)$ for large r independently of the strength of $V(r)$ [3]. Also, oscillations in ρ depend sensitively on the potential near the well bottom. This sensitivity has motivated several theoretical predictions for ρ based on possible interatomic potentials [4–7].

We have measured $\rho(k)$ in an atom interferometer using a technique that parallels out previous measurement at fixed k [3, 8]. ρ is found by measuring Ref, which is related to the phase shift caused by the collision, as well as Imf, which is related via the optical theorem to the absorption cross section [9]. An atom interferometer determines the phase shift and attenuation of the de Broglie wave in one arm of the interferometer that passes through a "target gas" by interfering with the other arm which does not. Specifically, propagation through a gas of length L modifies the wavefunction by a factor $\exp[i(n-1)k_{lab}L]$ where n is the complex index of refraction, $n = 1 + 2\pi n_d f(k,0)/k_{lab}k$, with n_d the target gas density and k and k_{lab} the Na wavevectors in the center-of-mass and lab frames.

The interferometer is composed of three nanofabricated diffraction gratings forming a Mach-Zehnder geometry [10]. A gas cell exposes one path of the interferometer to a gas while leaving the other path undisturbed (Fig. 1). A beam velocity of 0.7–3.0 km/s (with ∼5% rms spread) is chosen by changing the carrier gas mixture in the supersonic oven. The velocity is measured to ±30 m/s from the atom diffraction pattern of a grating.

Several apparatus improvements were necessary in order to study the velocity-dependent index of refraction. New 100 nm period gratings [11] double the path separation—and hence the maximum usable velocity in the interferometer—compared to the old 200 nm gratings [12]. These gratings, developed by Tim Savas and

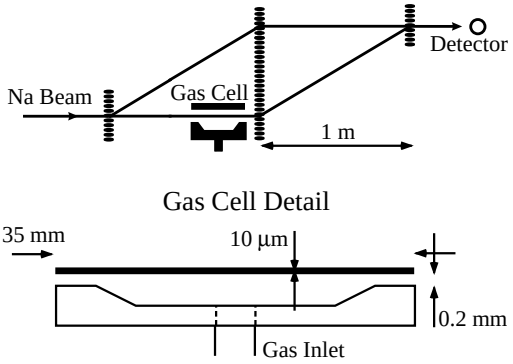

FIG. 1: Schematic of the atom interferometer and the gas cell.

Hank Smith, have already lead to a number of advances in atomic and molecular physics [13].

A thinner gas cell wall [14] also allows the atom paths to be closer together and hence allows higher velocities. The wall of the gas cell is a 10 μm thick Si wafer which is anodically bonded to a glass substrate. Channels cut into the glass create the volume of the cell and allow the beam to enter and exit (Fig. 1).

The gas cell can be filled and emptied with a time constant of 1–2 sec (∼10 times faster than before) using computer-controlled valves and wider supply lines. Faster cycle times reduce errors due to phase drift caused by thermal and mechanical motion of the gratings. This drift has been further reduced by mounting the interferometer on a rigid optical breadboard suspended by a vibration isolation system inside of the vacuum chamber.

ρ is measured by comparing the interference pattern with and without gas in the cell. In the absence of gas, we observe an interference pattern in the detected signal I_0 that depends on the position x of one of the gratings,

$$I_0(x) = N_0 + A_0 \cos(\phi_0 + k_g x), \tag{3}$$

where N_0 is the average detected flux of atoms (ranging from 5–100 kHz depending on beam velocity), A_0 is the amplitude of the interference pattern (typically 5–20% of N_0), and k_g is the grating wavevector. ϕ_0, the phase of the interference pattern in the absence of gas, is found by a fit to $I_0(x)$ which also determines N_0 and A_0. When the cell is filled with gas, the interference pattern becomes

$$I_{gas}(x) = N_{gas} + A_{gas} \cos(\phi_{gas} + k_g x) \tag{4}$$

from which ρ can be determined [8]:

$$\rho = \frac{\phi_{gas} - \phi_0}{\ln A_{gas} - \ln A_0} \tag{5}$$

A feature of this experimental method is that the measurements of attenuation and phase shift are *relative* measurements, eliminating problems due to intensity fluctuations and phase drift. Furthermore, measuring the ratio of attenuation vs phase eliminates the dependence on the target gas pressure (which may fluctuate), and obviates the need to know it absolutely. It also cancels out the $v^{-2/5}$ dependence of cross section and phase shift that can obscure the glory oscillations in f.

In Fig. 2, $\rho(v)$ is plotted as a function of Na beam velocity v for target gases of Ar, Kr, Xe, and N_2. Each data point represents an average of 1–3 hours of data taken at one to three different pressures at a single beam velocity on a single night. Our previous index of refraction measurement [8] taken at a beam velocity of 1 km/s is shown for comparison.

The improvements to the experimental apparatus mentioned above have allowed us to acquire the large range of data in Fig. 2 with smaller statistical error than our previous measurements. We have also been more careful to consider possible systematic errors, correcting for these effects where feasible.

The biggest source of systematic uncertainty is interference from unwanted paths that reach the detector—for instance, the two paths that form the mirror image of the interferometer shown in Fig. 1, or from paths of Na_2 molecules composing 25% of the intensity of the beam [22]. To avoid molecule interference, we deliberately misalign the gas cell wall at low velocities so that it appears wider than the Na_2 path separation. The 50 μm-wide detector is positioned to avoid the other orders, but because of beam alignment error and thermal drift, there is occasionally some detection of the wrong interference pattern, contributing as much as 5% to the interfering amplitude, A_0, except at higher velocities where it can be 50%. The resulting error in ρ is typically $+3/-0\%$ but as much as $+20/-0\%$ at the highest velocities of both the 100 and 200 nm data. This accounts for the asymmetrical systematic error bars in Fig 2.

Another systematic effect is the attenuation of the path outside the gas cell due to gas leaking from the ends of the cell. The integrated density of gas along the path inside the cell relative to the path outside is 120 ± 20 which results in a $+1.7(0.3)\%$ correction to the measured ρ.

Another source of error arises from measuring the interference pattern while the gas cell pressure hasn't fully equilibrated after filling or evacuating. We do this to reduce the cycle time to ∼20 sec leaving only 3 sec of dead time for filling or emptying. The resulting error in fitting to the time-averaged interference pattern, up to 0.5% uncertainty in ρ, is included in the systematic error bars.

Contaminants in the target gas must also be avoided. One such contaminant caused a 3% uncertainty in ρ for the 200 nm Ar data before it was fixed.

Error bars on the new data points in Fig. 2 include the sum of statistical and systematic errors. Because the only non-negligible systematic comes from beam alignment and drift, we have an independent check of this

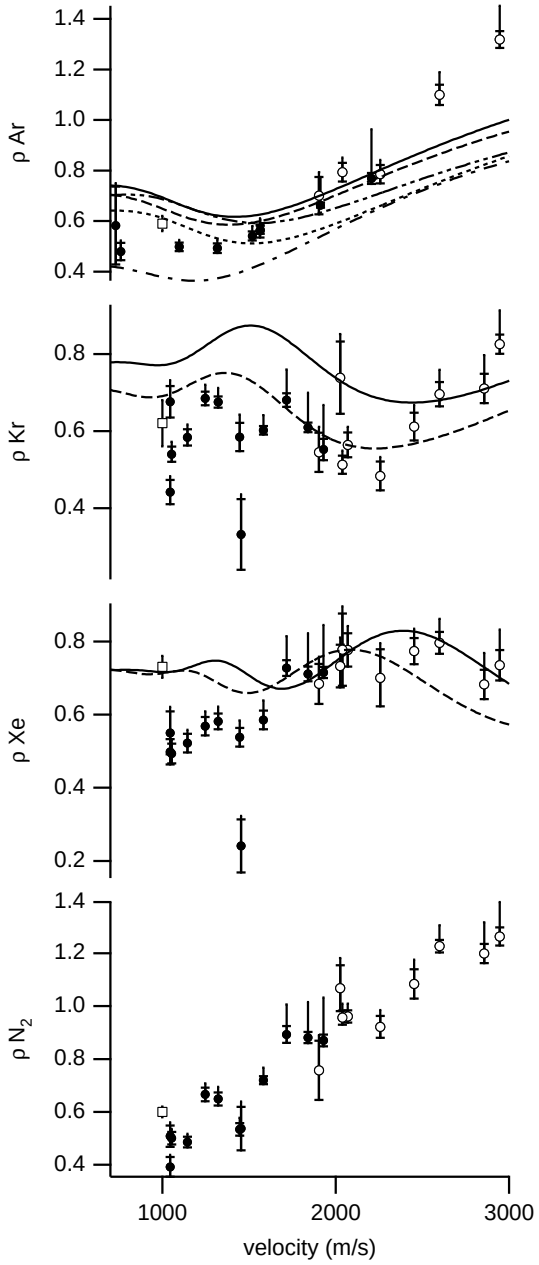

FIG. 2: ρ as measured for Na waves in Ar, Kr, Xe, and N_2 (• using 200 nm gratings, ∘ 100 nm), showing evidence of glory oscillations in comparison to ρ as derived from predicted potentials: Na-Ar [15](—), [16](− − −), [7](· · ·), [17](· − ·−), [18](· · −· · −); Na-Kr [15](—), [19](− − −); and Na-Xe [20](—), [19](− − −), [21](· · ·). Our 1995 measurement is also shown [8](□). The horizontal tick marks show the statistical error. The vertical error bar line includes systematic errors.

error by examining the repeatability of data taken on different nights. We expect that the error in alignment or drift may exceed our estimates on some nights, but this can be recognized: ρ will be artificially low compared to other nights, we will see this deviation in all the gases measured, and the measurement will have larger statistical error bars as the ratio changes due to drift. An example of these features can be seen in the severely outlying data points measured at 1450 m/s for Kr, Xe, and N_2.

Another check of systematics can be made by comparing the 100 and 200 nm data where they overlap. At this velocity, unwanted interference is seven times larger for the 200 nm data than for the 100 nm data, yet the agreement between the two is well within the error estimates.

The data are also consistent with older measurements taken at $v = 1$ km/s [8], with the exception of Xe, which disagrees dramatically. However, no care was taken in that experiment to consider systematic errors, which we estimate were $+30/-10\%$ in ρ due to the unwanted interference of Na_2 molecules and could have been worse for this particular measurement if thermal drift was excessive.

To compare our measurements with a prediction for $V(r)$, the sum in Eq. (1) must be computed. The Na wavelength is much smaller than the range of the interatomic potentials we are considering, so hundreds of partial waves contribute to the sum and we are justified in replacing it with an integral:

$$\mathrm{Re}f(k) = k\int_0^\infty b\,\sin 2\delta(b)\,db \tag{6a}$$

$$\mathrm{Im}f(k) = k\int_0^\infty 2b\,\sin^2\delta(b)\,db \tag{6b}$$

where $b \equiv (l+\frac{1}{2})/k$ is the classical impact parameter.

Because the kinetic energy is much greater than the well depth of the interatomic potential, we can find $\delta(b)$ using the Eikonal approximation—that δ is the accumulated phase shift of the atom traveling at constant speed along a straight-line path with impact parameter b:

$$\delta(b) = -\frac{\mu}{2k\hbar^2}\int_{-\infty}^{\infty} dz\,V(\sqrt{b^2+z^2}), \tag{7}$$

where μ is the reduced mass. Predictions using this approach are valid to 6% in ρ for the Na-Ar system and 3% for the Na-Kr and Na-Xe systems in comparison to an exact quantum treatment [23]. Predictions for ρ must also average over the room-temperature distribution of target gas velocities in our experiment, which damps the glory oscillations somewhat at lower beam velocities [6, 7].

Fig. 2 also shows calculations of $\rho(v)$ based on predictions of $V(r)$ for Na-Ar [7, 15–18], Na-Kr [15, 19], and Na-Xe [19–21] derived from spectroscopic measurements and beam scattering experiments. The oscillations

in these curves are glory oscillations, and are evident in the data. Even after allowing for statistical and systematic errors, our data disagree with these predictions. We believe this is because our measurements are very sensitive to the shape of the potential near the minimum (see examples in [24]), where the transition from the repulsive core to the Van der Waals potential is poorly understood, even though the well depth and location of the minimum are fairly well known. The N_2 data are remarkable as well for showing a large variation in ρ without any evidence of an oscillation, unfortunately, the potential is not understood in enough detail to explain this behavior [25, 26].

Because there is good agreement on the location and depth of the potential minima, we can use this knowledge to scale our measurements of ρ in a way that is sensitive to the *shapes* of all three Na-rare-gas potentials, independent of the well location and depth. We can write any potential as $V(r) = D_e g(r/r_e)$ where D_e and r_e are the depth and location of the minimum and $g(x)$ is a dimensionless function with a minimum $g(1) \equiv -1$. In the Eikonal approximation ρ depends only on $g(x)$ and the dimensionless parameter $\alpha \equiv D_e r_e/\hbar v$. α is approximately the phase shift in radians accumulated along the glory path. Changing the well depth or location of a potential without changing its shape $g(x)$ is equivalent to changing the velocity scaling of $\rho(v)$.

In Fig. 3 we have plotted measurements of ρ for Ar, Kr, and Xe verses the dimensionless parameter α, using values of D_e and r_e taken from [6]. Because of thermal averaging, the values of ρ we measure also depend weakly on the ratio of v to the mean speed of the scatterer, but differences in $\rho(\alpha)$ due to thermal averaging would be at most of 5%. Also included are data for Ne, with new systematic error estimates, which were taken with the older apparatus [5, 8]. Plotted in this manner, the combined data clearly show a full glory oscillation, as well as a hint of a second. For comparison we show ρ as derived from the Lennard-Jones potential, $g(x) = x^{-12} - 2x^{-6}$, and the Morse potential $g(x) = e^{-2\beta(x-1)} - 2e^{-\beta(x-1)}$ using $\beta = 4.7$ which is appropriate for the Na-Ar system [7]. The continuity of the data plotted together in this fashion demonstrates the similarity of Na-rare-gas potentials for these four systems and shows that Lennard-Jones and Morse potentials are too simplistic to accurately model the data here.

In conclusion, we have measured ρ to a typical accuracy of 9% at various Na velocities in gases of Ar, Kr, Xe, and N_2. The consistency of our scaled data for different gases suggests that the shape $g(x)$ of different Na-rare-gas potentials is similar. However, discrepancies in the comparison to predictions of ρ suggest that the shape of the potential is not well understood theoretically. Unfortunately, the difficulty of the inverse scattering problem [27, 28] prevents us from deriving the potential based on knowledge of $f(k)$. However, our explorations of modifications to suggested interatomic potentials do indicate that they would agree better with our measurements if $V(r)$ were modified such that $V(r_0) = 0$ occurs at smaller r_0 and the well were made less deep in the range $r_e < r < 2r_e$ [24]. Our measurements should be useful in evaluating future refinements of the relevant interatomic potentials.

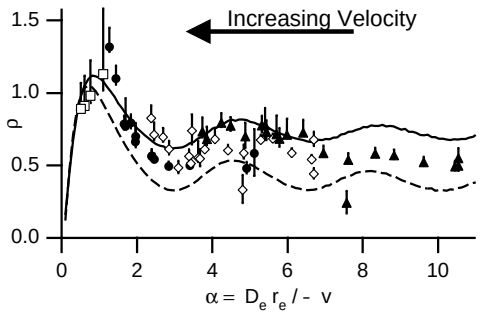

FIG. 3: ρ for the Na-rare-gas systems [Na-Ne (□), Na-Ar (•), Na-Kr (◊), and Na-Xe (▲)] plotted versus the dimensionless parameter $\alpha \equiv D_e r_e/\hbar v$. Also shown is the predicted ρ assuming a Lennard-Jones potential (—), and a Morse potential (− − −).

We would like to extend our grateful thanks to Tim Savas and Hank Smith for fabricating gratings for our use. We thank Edward Smith for the invention of the gas cell, and Peter Finin for his technical assistance. This work was supported by the Army Research Office Contracts DAAG55-97-1-0236 and DAAG55-98-1-0429, Naval Research Contract N00014-96-1-0432, and National Science Foundation Grant PHY98-77041. TR acknowledges the support of a National Defense Science and Engineering Graduate Fellowship.

[1] H. M. Nussenzveig, J. Opt. Soc. Am. **69**, 1068 (1979); R. A. Cheville, R. W. McGowen, and D. Grischkowsky, Phys. Rev. Lett. **80**, 269 (1998).
[2] K. W. Ford and J. A. Wheeler, Ann. Phys. **7**, 259 (1959).
[3] P. R. Berman ed., *Atom Interferometry* (Academic Press, 1997).
[4] E. Audouard, P. Duplaa, and J. Vigue, Europhys. Lett. **32**, 397 (1995).
[5] R. C. Forrey and *et al.*, Phys. Rev. A **54**, 2180 (1996).
[6] C. Champenois and *et al.*, J. Phys. II **7**, 523 (1997).
[7] R. C. Forrey and *et al.*, Phys. Rev. A **55**, R3311 (1997).
[8] J. Schmiedmayer and *et al.*, Phys. Rev. Lett. **74**, 1043 (1995).
[9] Glory oscillations in the absorption cross section were first measured by E. W. Rothe *et al.*, Phys. Rev. **128**, 659 (1962) for Li and K beams.
[10] D. W. Keith and *et al.*, Phys. Rev. Lett. **66**, 2693 (1991).
[11] T. A. Savas and *et al.*, J. Vac. Sci. Technol. B **14**, 4167

(1996).
[12] M. J. Rooks and *et al.*, J. Vac. Sci. Technol. B **13**, 2745 (1995).
[13] M. Arndt *et al.*, Nature **401**, 680 (1999); R. E. Grisenti *et al.*, Phys. Rev. Lett. **83**, 1755 (1999); R. E. Grisenti *et al.*, Phys. Rev. Lett. **85**, 2284 (2000); G. C. Hegerfeldt and T. Kohler, Phys. Rev. A **6102**, 3606 (2000).
[14] T. D. Hammond, PhD thesis, MIT (1997).
[15] Potential proposed by Zimmermann *et al.* in [6].
[16] R. Duren and W. Groger, Chem. Phys. Lett. **56**, 67 (1978).
[17] J. Tellinghuisen and *et al.*, J. Chem. Phys. **71**, 1283 (1979).
[18] K. T. Tang and J. P. Toennies, J. Chem. Phys. **66**, 1496 (1977).
[19] R. Duren, G. P. Raabe, and C. Schlier, Z. Phys. **214**, 410 (1968).
[20] P. Baumann, D. Zimmermann, and R. Bruhl, J. Mol. Spectrosc. **155**, 277 (1992).
[21] U. Buck and H. Pauly, Z. Phys. **208**, 390 (1968).
[22] M. S. Chapman and *et al.*, Phys. Rev. Lett. **74**, 4783 (1995).
[23] R. C. Forrey (2001), personal communication.
[24] T. D. Roberts, PhD thesis, MIT (2002), to be written.
[25] P. Habitz, Chem. Phys. **54**, 131 (1980).
[26] A. P. Nefedov, V. A. Sinel'shchikov, and A. D. Usachev, Phys. Scr. **59**, 432 (1999).
[27] R. G. Newton, *Scattering Theory of Waves and Particles* (McGraw-Hill, 1966).
[28] K. Chadan and P. C. Sabatier, *Inverse Problems in Quantum Scattering Theory* (Springer, New York, 1989).

Appendix B

Interference Lost to Momentum Transfer in an Atom Interferometer

Abstract

By inserting a diffraction grating into both paths of an atom interferometer, we observe a reduction in interference fringe contrast due to momentum transferred to each path by diffraction. The loss of contrast is quite similar to decoherence caused by scattering photons from the interfering paths, which transfers momentum to the paths by photon recoil. We compare the two mechanisms of contrast loss and consider whether they are examples of decoherence.

B.1 Introduction

We present here the results of two experiments in which different types of interactions cause a loss of fringe contrast in an atom interferometer. The first experiment modifies our "white-fringe" interferometer, which forms the same interference pattern for atoms of all velocities, into a chromatic interferometer, in which the interference pattern will wash out due to a sufficient spread in velocity. In a white-fringe interferometer, each atom in the interferometer contributes to an interference pattern with exactly the same phase regardless of its velocity. A chromatic interferometer is

made by applying a fixed momentum kick to each atom. The phase becomes velocity dependent, destroying the interference pattern.

The second experiment is a classic example of decoherence in which scattered photons destroy coherence because they could in principle be measured to determine which path an atom took. We present these experiments side-by-side because the loss of contrast in each case can be explained by the same mechanism—momentum transfer to the atoms within the interferometer—however, it is not obvious whether both are examples of quantum decoherence.

B.2 Phase Shift Due To Momentum Transfer

In both experiments we apply a transverse momentum kick to the atom whose wavefunction in both paths of a three-grating Mach-Zehnder atom interferometer. In the first example the momentum transfer is accomplished by inserting a diffraction grating into the two paths of the interferometer (Fig. B-1). If only the +1 diffractive order of the grating is detected, the two paths effectively receive a fixed momentum kick of $+h/\lambda_g$ where λ_g is the period of the diffraction grating. We will call this a "fixed-kick" interferometer.

Consider the effect of the diffraction grating on the phase of the fixed-kick interferometer relative to the unkicked interferometer. A plane atom wave $\psi(\vec{r}) = \exp[i\vec{k_{\rm dB}} \cdot \vec{r}]$ at near-normal incidence to the diffraction grating acquires a momentum kick $\hbar k_g \equiv h/\lambda_g$ after diffraction into the +1 order. The outgoing plane wave then takes the form $\psi(\vec{r}) = \exp[i(\vec{k_{\rm dB}} + k_g\hat{x}) \cdot \vec{r}]$. This is equivalent to acquiring a position dependent phase shift $\phi(x) = k_g x$. Since the two paths of the interferometer are a distance d apart at the location of the momentum transfer, the resulting phase shift of the interference pattern is

$$\phi = k_g d \tag{B.1}$$

where $\hbar k_g$ is the momentum recoil of the atom.

An alternative picture can also explain this phase shift. The two paths of the interferometer form an interference pattern when they converge. The momentum

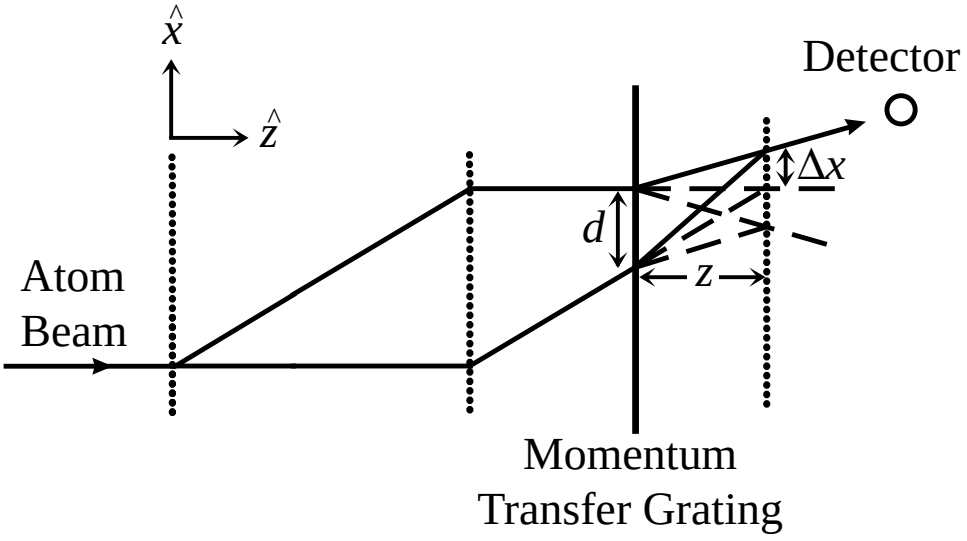

Figure B-1: Momentum transfer by the decohering grating destroys the interference pattern.

kick at a distance z upstream of where they converge deflects the interference pattern, with period λ_f, by an amount $\Delta x = z(k_g/k_{dB}) = d(\lambda_f/\lambda_g)$, which is equivalent to a phase shift $\phi = 2\pi\Delta x/\lambda_f = k_g d$. [1]

Now consider the "photon-kicked" interferometer, in which a resonant laser beam takes the place of the diffraction grating and momentum is transferred to the atoms by scattering photons out of the laser beam (Fig. B-2). The key difference is that the momentum kick is variable, depending on the scattering angle of the photon. We have examined this behavior in detail in two previous experiments [19, 57]. To facilitate a comparison with the fixed-kick interferometer, suppose that the photon kick is known: atoms with incident momentum $\hbar\vec{k_i}$ scatter with well-defined (i.e. measured) final momentum $\hbar\vec{k_f}$. From each photon that scatters, the atomic wavefunction acquires a relative difference in phase between the two paths of $\phi = \Delta k_x d$ where $\Delta k_x = (\vec{k_f} - \vec{k_i}) \cdot \hat{x}$ is the total change in the wavevector of the scattered photon in the

[1] This simple picture fails to predict the correct phase when the kick is located in the first half of the interferometer where the paths are diverging. In such an arrangement the phase can still be predicted by Eq. B.1, whereas the deflection of the interference fringes would suggest a much larger phase shift.

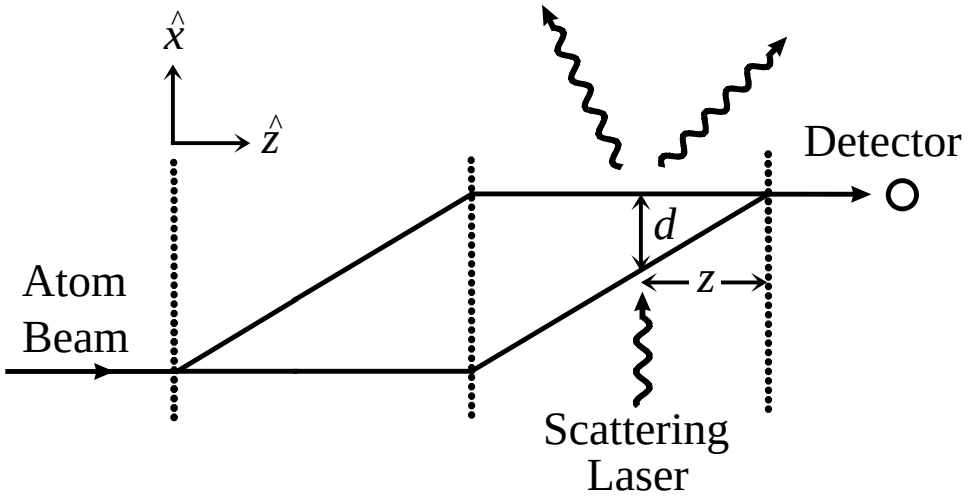

Figure B-2: Momentum transfer by the scattered photons destroys the interference pattern.

transverse ($\hat{x}$) direction and d is the separation between the two paths. In this experiment, multiple photons are scattered and the total phase shift is the sum of the phase shifts for individual scattering events. The total relative change in phase between the two paths is therefore related to the total momentum recoil of the atomic wavefunction due to the scattered photons. The total phase is

$$\phi = \Delta k d \tag{B.2}$$

where $\hbar\Delta k$ is the total transverse momentum recoil (the sum of $\hbar\Delta k_x$ for each scattered photon) and d is the path separation at the location of scattering. We find that the phase shift is identical to the case of a fixed-kick phase shift when the momentum recoil of the atom is $\Delta k = k_g$.

B.3 Momentum Transfer Causing Loss Of Interference Contrast

We have explained how momentum recoil shifts the phase of interference fringes, but we are concerned here with possible decoherence due to averaging over a range of possible phase shifts, $\phi = \Delta k d$. In the fixed-kick interferometer, Δk is fixed but d is uncertain because it depends on the wavevector k_{dB} of the atom. d is determined from the diffraction angle in the interferometer which is a function of the wavevector of the atom: $d(k_{\mathrm{dB}}) = 2\pi z/k_{\mathrm{dB}}\lambda_f$ (the gratings that compose the interferometer have period λ_f). Atoms with different longitudinal momentum will therefore form interference fringes with different phases. The total interference pattern measured will be an incoherent sum of interference patterns for different de Broglie wavelengths in the beam. The intensity of the interference signal detected is

$$C' \cos\phi' = \int C_0 \cos\left[\phi_0 + \Delta k\ d(k_{\mathrm{dB}})\right]\ P(k_{\mathrm{dB}})\ dk_{\mathrm{dB}}, \tag{B.3}$$

where $C_0 \cos\phi_0$ is the original interference signal with contrast C_0 and phase ϕ_0, and $P(k_{\mathrm{dB}})$ is the probability distribution of de Broglie wavevectors k_{dB} in the atomic beam.

Contrast is lost because the phase of the interaction must be averaged over the Gaussian distribution of wavevectors in our supersonic beam of atomic sodium, which has a typical mean velocity of 3000 m/s and a 5% rms velocity. The corresponding distribution of de Broglie wavevectors is:

$$P(k_{\mathrm{dB}}) = \frac{1}{\sqrt{2\pi k_{\mathrm{dBrms}}^2}} \exp\Big[-\frac{1}{2}\big(\frac{k_{\mathrm{dB}} - k_{\mathrm{dBavg}}}{k_{\mathrm{dBrms}}}\big)^2\Big] \tag{B.4}$$

where k_{dBavg} is the mean de Broglie wavevector of the longitudinal wavefunction and k_{dBrms} is the rms spread in wavevectors.

For this distribution the contrast and phase of the measured interference pattern

predicted from Eq. B.3 is

$$C' = C_0 \exp\Big[-\frac{1}{2}\big(\frac{k_{\mathrm{dBrms}}}{k_{\mathrm{dBavg}}}\big)^2 k_g^2 d_{\mathrm{avg}}^2 \Big] \tag{B.5}$$

$$\phi' = \phi_0 + k_g d_{\mathrm{avg}} \tag{B.6}$$

where $d_{\mathrm{avg}} \equiv d(k_{\mathrm{dBavg}})$.

We now turn to the photon-kicked interferometer. The phase of the interference pattern of a given atom is uncertain because different atoms receive different momentum recoils due to the angle of the photons they scatter. The detected interference signal is the incoherent sum of interference patterns for every possible recoil of the atom in the photon field:

$$C' \cos\phi' = \int C_0 \cos\big[\phi_0 + \Delta k d_{\mathrm{avg}}\big] P(\Delta k) d\Delta k, \tag{B.7}$$

where $P(\Delta k)$ is the probability of acquiring a momentum kick $\hbar\Delta k$. (The variation in d, important above, is negligible for the photon-kicked interferometer.)

If $P(\Delta k)$ is a Gaussian distribution, as is the case in our experiment when multiple photons are scattered for each atom, with mean and rms momentum transfer $\hbar k_{\mathrm{avg}}$ and $\hbar k_{\mathrm{rms}}$, the resulting contrast is [57]:

$$C' = C_0 \exp\big[-\frac{1}{2} k_{\mathrm{rms}}^2 d_{\mathrm{avg}}^2 \big] \tag{B.8}$$

The exponential dependence on the path separation squared is a common feature of many general models of decoherence [39, 4, 20].

B.4 Measuring Fixed-Kick Contrast Loss

We measured the contrast loss in the fixed-kick interferometer due to a momentum transfer grating with period $\lambda_g = 100$ nm; the gratings that compose the interferometer have a period $\lambda_f = 200$ nm. We investigated the loss of interfering contrast while varying z, the location of the momentum transfer grating. The narrow atom

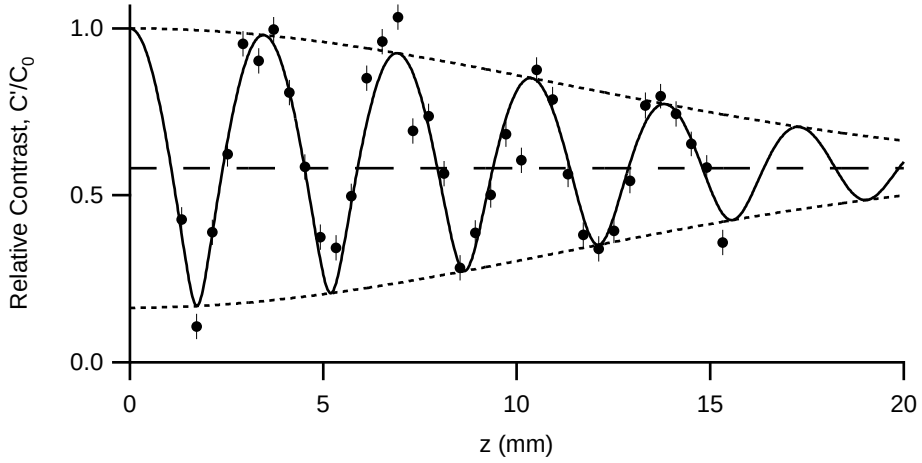

Figure B-3: Decay of interference fringe contrast due to a fixed momentum kick interaction as a function of z, the distance of the kick from the third grating. Interference fringes with no kick, with contrast shown by (– – –), are unavoidably measured along with the fringes that have been kicked, with contrast shown by (- - -)—the envelope of the beat pattern). From a fit using Eq. B.5 and B.6 we can determine a beam velocity of 3006(12) m/s and a velocity width of 5.0(3)% rms.

detector was located downstream at a fixed transverse position to selectively detect the +1 diffractive order of the momentum transfer grating (Fig. B-1). Because we could not position the detector far enough downstream the selectivity was imperfect and the detector also measured some of the interference pattern from the 0th order. The contrast and phase of the 0th order fringes are unaffected by the momentum transfer grating (they have no dependence on z) but they beat with the +1 order as the phase of its fringes increase with increasing z (Fig. B-3).

We fit the combined contrast (solid line in Fig. B-3) using the contrast and phase of the interference pattern from the +1 order as predicted by Eq. B.5 and B.6. From the fit we determine the velocity and velocity spread of the beam, $v_{\rm avg} = (\hbar/m)k_{\rm dBavg} =$ 3006(12) m/s and $k_{\rm dBrms}/k_{\rm dBavg} = 5.0(3)\%$. This agrees with our knowledge of the velocity as determined by a fit to the diffraction pattern of a single grating. The difference of the envelope of the fit from the average (with is due to the $0^{\rm th}$ order) in Fig. B-3 is the contrast of the interference pattern from the +1 order as predicted by Eq. B.5 using the value of $k_{\rm dBrms}$ as determined from the fit. This demonstrates the

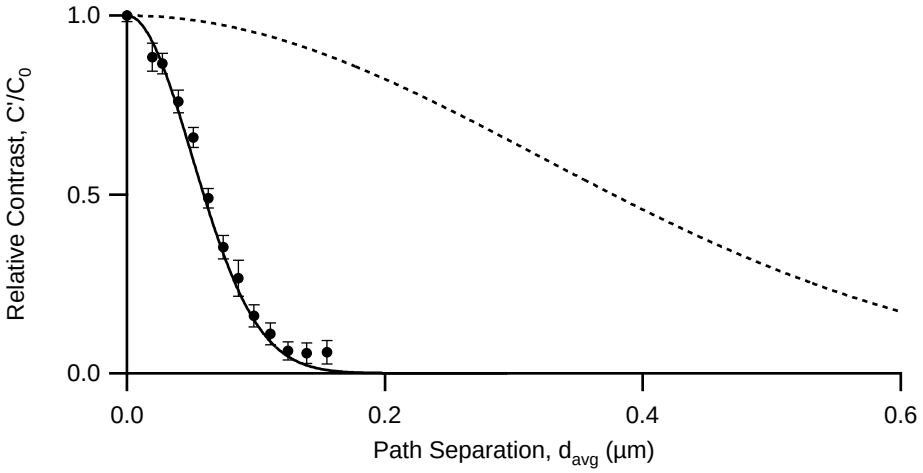

Figure B-4: A comparison of the length scales for decoherence by photon scatter and a fixed momentum kick. The data show the contrast dependence when scattering multiple photons. The dashed line shows contrast for the first order of the diffraction grating from the fit of the data in Fig. B-3.

exponential decay of the contrast as z^2, and correspondingly as $d_{\rm avg}^2$, increases.

B.5 Measuring Photon-Kick Contrast Loss

We measured the contrast loss in the photon-kicked interferometer in a similar manner. Ref. [57] describes a recent experiment in which several photons where scattered from the paths of our atom interferometer in a study of the evolution of decoherence in the many scatterer limit. We summarize some of the results of that experiment here.

For a sufficiently large number of photons scattered ($n > 3$), the distribution of momentum transfer to a single atom approaches a Gaussian distribution with mean momentum transfer $\hbar k_{\rm avg} = \bar{n}\hbar\bar{k}_x$ and rms momentum transfer $\hbar k_{\rm rms} = \hbar\sqrt{\bar{n}\sigma_k^2 + \sigma_n^2\bar{k}_x^2}$ where $\bar{n}$ and σ_n are the mean and rms number of photons scattered and $\hbar\bar{k}_x$ and $\hbar\sigma_k$ are the mean and rms momentum transfer for a single photon scattering event. The contrast remaining after interaction with the photon field can be predicted by Eq. B.7.

Fig. B-4 shows the measured dependence of the relative contrast C'/C_0 on the path separation $d_{\rm avg}$. The solid line in Fig. B-4 is not a fit, but is the predicted contrast (Eq. B.8) using the independently measured parameters $\bar{n} = 4.8(2)$ and $\sigma_n = 1.8(1)$, and using $\sigma_k = \frac{2}{5}\bar{k}_x$ for the dipole radiation pattern of the circularly polarized incident photons with $\bar{k}_x = 2\pi/(590\text{ nm})$. For comparison, the fit of the contrast loss in the fixed-kick experiment (dotted line) is also shown.

B.6 Are These Experiments Examples Of Quantum Decoherence?

We consider now whether both forms of contrast loss presented here are examples of quantum decoherence. In Ref. [4], Anglin *et al.* have expressed the "unfortunate ambiguity in the term 'decoherence'," and they present a restrictive definition of decoherence that is similar to definitions suggested by others, by defining it as "the evolution of the density matrix towards diagonality in a preferred basis, on a much shorter time scale than that of evolution towards a unique equilibrium state."

Both forms of contrast loss in our experiment satisfy this definition of decoherence, as long as we suitably define what we mean by the "environment." We will explain what constitutes the decohering environment in each experiment.

In the photon-kicked interferometer, we identify the scattered photon field as the environmental degree of freedom. Decoherence is caused by the entanglement of system and environment, in which the transverse degree of freedom of the atom is entangled with the corresponding degree of freedom of the scattered photon. The subsequent evolution of the density matrix of the atom is calculated by taking a weighted average, or trace, over the environmental degrees of freedom (the final momentum of the photon) resulting in a loss of spatial coherences for the atom.

Contrast loss in the fixed-kick interferometer can be similarly described as decoherence if we identify the atom's longitudinal degree of freedom as the environmental degree of freedom. In this case, the coupling of the system and environment is caused

by the momentum transfer grating as it entangles the transverse and longitudinal degrees of freedom of the atom. Evolution of the system is computed by averaging over the longitudinal degrees of freedom, destroying spatial coherences in the transverse degree of freedom.

Although this satisfies the definition of decoherence as expressed above, it is in some respects objectionable that it should qualify. Though we have framed the results of the experiment in the language of decoherence, the experiment itself appears more closely related to inhomogeneous broadening. Like the fixed-kick interferometer, inhomogeneous broadening is an example of a process in which coherences that exist for a single velocity class of atoms are destroyed when a wider distribution of velocities is involved.

Ultimately, it is a matter of semantics, not physics, as to whether this experiment should be excluded from a definition of quantum decoherence. However, refining a definition of decoherence or distinguishing between different forms of decoherence will facilitate better understanding of this subject. We propose therefore that such a distinction should be made to address some of the "unfortunate ambiguity" in the term.

It may be useful to formulate a definition of decoherence based on one or more of the following criteria:

1. Whether the decoherence is among "internal" or "external" degrees of freedom.
2. Whether the decoherence is suitably "irreversible."
3. Whether the environment must be measured before and after its entanglement with the system in order to retrieve coherence.
4. Whether a "which-way" quantity is measured by the environment.
5. Whether a quantum, not classical, coincidence measurement is required to retrieve coherence (with a suitable definition of "quantum measurement").
6. Whether correlations that violate Bell's inequalities exist between the environment and the system.

Consider, for instance, the first suggested distinction. Decoherence is often just the case of coupling to a degree of freedom whose evolution is unknown or ignored. This is what happens in fixed-kick interferometer as well. The momentum transfer grating couples the transverse wavefunction of the atom with the atom's longitudinal degree of freedom. The longitudinal degree of freedom is unmeasured in our experiment and must be averaged over to determine the density matrix for the transverse evolution. We could, then, stretch the definition of decoherence to include the fixed-kick interferometer by describing the atom's longitudinal degree of freedom as an environmental degree of freedom.

Note however that the terms "internal" and "external" degree of freedom are not necessarily well defined. There is not always a clear distinction between "environments" that couple to a quantum system as internal degrees of freedom, like the atom's own longitudinal momentum, and those that couple to the system externally, like the photon field. Consider, for instance, the many degrees of freedom in a large molecule NMR quantum computer that span this entire range.

The importance of considering "internal decoherence" may be illustrated by a final example. It is possible to account for the influence of the *external* environment in the photon-kicked interferometer by an average over the *internal* degrees of freedom of the atom. We demonstrated this earlier—that averaging over the momentum of the scattered photon is equivalent to averaging over the transverse momentum recoil of the atom. Since, however, the uncertainty is in an internal degree of freedom, the information is not necessarily lost irreversibly to the environment. If only atoms with a specific recoil are measured by using a narrow detector as we did in Ref. [19], the phase of the interference pattern becomes well determined again and coherence is regained.[2] By this account, even in an example of "true" decoherence, where an atom becomes entangled with a photon environment, information is still stored

[2]It is not possible however to both measure which path the atom took by resolving the scattered photon and see an interference pattern by measuring the atom's recoil. We could measure an interference pattern for particular recoils only because the beam was wider than the path separation, preventing a which-way measurement. If the beam had been narrow enough to measure the path an atom had taken, the Heisenberg uncertainty due to this narrowness would have disturbed any attempt to measure recoil.

internally, and internal manipulations can restore the atom's coherence. Based on this example, there is no reason to exclude "internal decoherence" from a definition of "true" decoherence.

Appendix C

Effects of Casimir and Van der Waals Forces on Atom Diffraction

C.1 Theory

It is an intriguing prediction of quantum electrodynamic theory that the vacuum has infinite energy in its ground state: $\hbar\omega/2$ for each electromagnetic (EM) mode, of which there are an infinite number. Perhaps more intriguing is that this zero-point energy is not simply a constant energy that can be subtracted from any Hamiltonian under consideration. At small distance scales, some physical systems may be sensitive to the spatial dependence of the EM modes, and in some instances the vacuum energy can be extracted from the system. An example of this is the Casimir attraction between two parallel conducting walls. A displacement of the walls towards each other decreases the density of modes between the plates more than it increases the mode density outside the plates, producing a net decrease in vacuum energy. The energy difference is converted to an increased kinetic energy of the plates [22].

Atoms may be affected by the vacuum mode structure as well, and the interaction of atoms with the boundaries of EM modes (i.e. conducting and dielectric walls) will be the focus of this paper. In 1948, Casimir and Polder showed that neutral atoms near a conducting wall experience a $1/z^3$ potential at short distances and a $1/z^4$ potential at larger distances where z is the atom's distance from the wall [15].

The calculation is made by considering the perturbation of the atom-vacuum mode interaction on the energy of the atom's ground state and the ground state of the EM modes.

The operator for this interaction (assuming a single electron atom) is

$$G = -\frac{e}{mc}\,\vec{p}\cdot\vec{A} + \frac{e^2}{2mc^2}\,A^2 \tag{C.1}$$

which comes from the expansion of the electron's energy in the electromagnetic field, $(\vec{p} - \frac{e}{c}\vec{A})^2/2m$. Since A has no diagonal terms, the first order perturbation energy vanishes for the first term in G, leaving a perturbation energy of order e^2:

$$\Delta E = \sum_e \frac{e^2}{m^2c^2}\;\frac{\left|\langle e|\vec{p}\cdot\vec{A}|g\rangle\right|^2}{E_e - E_g} + \frac{e^2}{m^2c^2}\;\left\langle e\middle|A^2\middle|g\right\rangle \tag{C.2}$$

where g includes the ground state of all EM modes and the sum is over all excited states of both the atom and the field.

Both terms in Eq. C.2 are divergent due to an infinite number of modes, but any changes to this energy due to changes in the atom's position are finite. Far from the boundaries of the EM field, the mode structure changes very little with the atom's position and no forces will be experienced. At a conducting boundary, however, the transverse component of an EM wave must vanish, resulting in a spatial variation of the vacuum field which contributes to a spatial variation in potential energy for the atom. Casimir and Polder calculated the spatial variation in ΔE near a flat, conducting wall and showed that for distances large compared to c/ω_0 (ω_0 refers to the lowest resonant frequency of the atom) the potential is

$$V_{\text{far}} = -\frac{\hbar c\alpha}{8\pi}\;\frac{1}{z^4} \tag{C.3}$$

where α is the ground state polarizability of the atom, and for small distances $z \ll c/\omega_0$

$$V_{\text{near}} = -\frac{d^2}{12}\;\frac{1}{z^3} \tag{C.4}$$

where d^2 is defined as the expectation value of the dipole operator squared, $d^2 \equiv \langle g|e^2r^2|g\rangle = 20\ e^2a_0^2$ for sodium. Eq. C.3 and C.4 are approximately equal at a distance of c/ω_0, since $\alpha \approx 2d^2/\hbar\omega_0$.

At small distances, a simpler interpretation can explain the spatial dependence of the potential and the role of the resonant frequency of the atom. The potential at small distances had been explained prior to Casimir and Polder's paper by London, who considered the Van der Waals attraction between an atom and its image in a conducting wall [62]. Although the ground state atom has a vanishing electric dipole moment ($\langle g|e\vec{r}|g\rangle = 0$), the square of the dipole operator is non-vanishing due to quantum fluctuations ($\langle g|e^2r^2|g\rangle \neq 0$). The interaction energy between two classical dipoles $\vec{d}$ and $\vec{d}'$ is

$$W = \frac{\vec{d}\cdot\vec{d}' - 3d_z d_z'}{R^3} \tag{C.5}$$

where R is the separation of the two dipoles and the z-axis is assumed to lie along the line connecting them. If d' is the image dipole of d, then $dx' = -dx$, $dy' = -dy$, and $dz' = dz$. The interaction energy between a dipole and its image is half that between two real dipoles:

$$W = -\frac{d_x^2 + d_y^2 + 2d_z^2}{16z^3} \tag{C.6}$$

where R has been replaced with twice the atom-wall distance, z. Assuming that fluctuations in the dipole moment have no preferential direction, $dx^2 = dy^2 = dz^2 = d^2/3$, reproducing the potential in Eq. C.4.

Intuitively, the dipole fluctuations can be assumed to take place within a time scale of $1/\omega_0$, the inverse of the dipole transition frequency. If the atom is farther than a distance of c/ω_0 from the wall, the fluctuations take place too quickly for their effects to travel to the wall and back, and the image dipole is no longer correlated with the dipole itself. It is for this reason that the Casimir-Polder force at long distances is also referred to as the retarded Van der Waals interaction. An understanding of the retarded interaction requires the analysis of the vacuum modes and their affect on the atom.

It is also interesting to consider the potential of an atom between two conducting

walls [94, 81, 49]. At small wall separations L the potential is due to the attraction between the atom and its multiple images. The atom sees not only its own image in each wall, but images of images as well. Summing over all interactions:

$$V_{\text{small}} = -\frac{2d^2}{3L^3} \sum_{\text{odd } n} \left[\frac{1}{(n - 2z/L)^3} + \frac{1}{(n + 2z/L)^3} \right]. \tag{C.7}$$

z is now defined as the distance of the atom from the midpoint of the two walls. Images with even n do not move with respect to the atom and contribute a constant energy that can be neglected.

At large distances, the presence of two walls changes the mode structure and consequently the potential energy of the atom. In the large L limit it can be approximated by:

$$V_{\text{large}} = -\frac{\pi^3 \hbar c \alpha}{L^4} \left(\frac{2 - 3\cos^2(\pi z/L)}{8\cos^4(\pi z/L)} \right) \tag{C.8}$$

with z again the distance from the midpoint.

For L both large and small, the potential still grows by the cube of the distance in the limit of $z \to \pm L/2$. It is also worth noting that both potentials differ very little from the sum of two single wall potentials. The difference is a maximum of 5% for small L and 1% for large L and is greatest at the midpoint ($z = 0$).

Casimir forces can also be calculated for the interaction of an atom and a dielectric wall. The more complicated boundary conditions and the frequency dependence of the dielectric, $\epsilon(\omega)$, makes the calculations more difficult, however. If the ω dependence of the dielectric is neglected (assuming $\epsilon(\omega) \approx \epsilon(0) \equiv \epsilon$), an estimate of the potential can be made by scaling the potential for a conducting wall (the limit of $\epsilon \to \infty$) by a scale factor of $(\epsilon + 1)/(\epsilon - 1)$. This estimate is valid to within 10% [49].

C.2 Experimental Feasibility

The success of atom interferometry in measuring extremely weak potentials [84, 34] raises the question of whether it could in principle be used to make precision measurements of Casimir-Polder forces. The best measurements to date are by Hinds

et al. and have a precision of about 13% [94]. The group measured the flux of a sodium beam passing between conducting walls. The attenuation of the beam due to deflections of atoms into the walls is an indication of the Casimir-Polder force.

Consider a standard atom interferometer experiment consisting of a separated-beam, Mach-Zehnder interferometer and a 1 cm interaction region for one of the beams. The interaction region could consist of parallel metal plates of variable separation. Variation in the separation could be accomplished by means of making a wedge out of the two plates and translating the wedge vertically, as was carried out in the Hinds measurement. An alternative interaction region could consist of a single conducting wall that could be translated horizontally to increase the potential for the close beam relative to the far one. This configuration would have some practical advantages in its construction but would be more sensitive to the finite width of the beam. It will be sufficient for a study of feasibility to examine only the double wall interaction region experiment.

Using the ground state polarizability of sodium, $\alpha = 162.7\ a_0^3$, the potential energy at the midpoint between two conducting walls is

$$V = -\frac{\pi^3(137)(162.7)}{8}\ \frac{e^2 a_0^3}{L^4} = -(4.62\ \text{kHz} \times \mu\text{m}^4)\frac{1}{L^4} \tag{C.9}$$

so long as $L \gg \sim 2\ \mu$m.

For a typical beam velocity of 1 km/s and a 1 cm interaction region, the transit time is $t_{\text{transit}} = 10\ \mu$s and the phase accumulated (relative to the other beam) is $V\, t_{\text{transit}}/\hbar = (0.29\ \text{radians} \times \mu\text{m}^4)/L^4$. Current interferometer sensitivity is limited to about 10 mrad/$\sqrt{\text{min}}$ and is achieved using beam widths on the order of 20 μm to maintain a sufficient flux of atoms at the detector. For a practical cavity width of $L = 20\ \mu$m, the phase shift is 1.8×10^{-6} radians for atoms at the midpoint. The phase shift increases for positions nearer one of the walls, but a plot of phase shift verses distance in Fig. C-1 shows that only a small fraction of the beam receives a useful shift in phase (between 0.01 and π radians). Also, atoms near the wall experience a force causing them to collide with the wall.

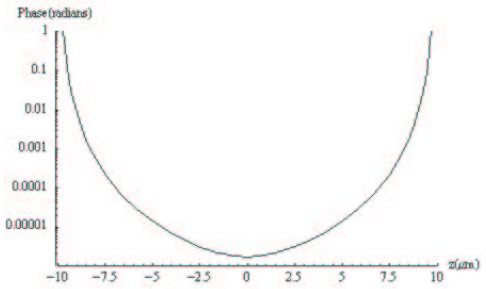

Figure C-1: Phase accumulated for atoms passing between two conducting walls as a function of the atom's distance from the midpoint. The wall separation is 20 μm and the interaction time is 10 μs.

Increasing the interaction time by using a longer interaction region or a slower beam velocity would improve sensitivity but could never alone bring the interferometer within range of a Casimir-Polder measurement. Only a significant increase in beam flux or other improvement to the minimum detectable phase (of at least an order of magnitude) would begin to exhibit the effects of Casimir-Polder forces, and even then the effects could only be tested for atom-wall distances of one to a few microns.

Though the Casimir-Polder forces diminish rapidly for large distances, at small distances the equivalent Van der Waals interactions grow quite substantially as the distance approaches zero. The magnitude of the attraction at sub-micron distances leads to a consideration of the interaction of atoms with the interferometer's atom diffraction gratings. Ultimately it may be important to consider how the Van der Waals forces affect the grating in unexpected ways, but perhaps more interesting is the possibility of observing a significant change in the grating's diffraction pattern to detect and verify the presence of Van der Waals interactions.

The smallest of the interferometer's gratings have a 100 nm period and ∼100 nm thickness. Neglecting edge effects, the passage of an atom through a slit in the grating can be modeled as before using a double wall interaction region with a 50 nm separation. One difficulty that arises is that the grating is composed of silicon nitride which is not conducting, but a good estimate of the potential near the dielectric can

be made by using the potential for a conductor and scaling the result by the factor $(\epsilon+1)/(\epsilon-1)$. For silicon nitride, $\epsilon \approx 8$, giving a scale factor of 78%. Metal gratings will be assumed in subsequent calculations with the understanding that for silicon nitride the interactions are $\sim 20\%$ weaker.

The period of our gratings is in the mid-distance regime, $L \approx c/\omega_0$ ($c/\omega_0 = 94$ nm for sodium), where retardation effects start to play a role. To account for this, the exact solution for the Casimir-Polder potential is required, which can be expressed as [94]:

$$V_{\text{exact}} = \sum_e \frac{2\pi^2 \left|\langle e|d|g\rangle\right|^2}{3L^3} \int_0^\infty d\rho \, \frac{\rho^2 \cosh(2\pi\rho z/L)}{\sinh(\pi\rho)} \arctan\left(\frac{\rho\lambda_{eg}}{2L}\right) \tag{C.10}$$

where the sum is over all excited states, and $\langle e|d|g\rangle$ is the matrix element for the electric dipole transition and λ_{eg} its wavelength. For sodium the sum is dominated by the 3p excited state and the others can be neglected. Figure C-2 shows a comparison of the small L, large L, and the exact potentials for a 50 nm slit (in a 100 nm period grating) and a 100 nm slit (in a 200 nm grating). The Van der Waals approximation is valid to within 20% for the 50 nm slit but only 40% for the 100 nm slit and is worst at the midpoint.

As can be seen in Fig. C-2, the potentials are very deep. The interaction time is much smaller though ($t_{\text{transit}} = 0.1$ ns for a 1 km/s beam velocity) and the phase accumulated for a classical trajectory passing through the midpoint of the slit is 0.11 radians. The phase is plotted in Fig. C-3. Intuitively, the far field diffraction pattern can be expected to change if the atom's phase is disturbed by $\sim \pi$, so this result suggests the effects will be observable.

The strength of the potential grows rapidly enough near the walls that it is important to consider trajectories of atoms that travel into the grating and are deflected into the walls. To find the time t_0 necessary for an atom to collide with the wall, consider an atom initially at distance z_0 from the wall with zero initial velocity normal to the wall. Conservation of energy requires that $\frac{1}{2}mv^2 - \frac{1}{12}d^2/z^3 = -\frac{1}{12}d^2/z_0^3$. Expressing v as dz/dt, solving for dt and integrating dt over the appropriate times

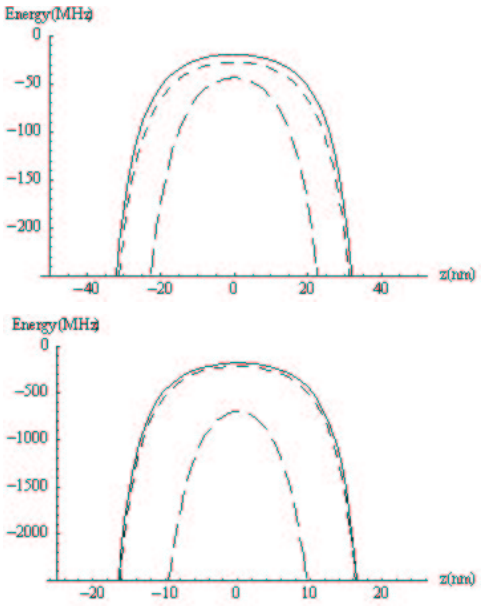

Figure C-2: Potential energy of a sodium atom as a function of position between parallel conducting walls of 100 nm separation and 50 nm separation, respectively. The exact solution is shown (—) as well as the van der Waals approximation (- - - -). The large distance approximation (− − −) is poor in this regime.

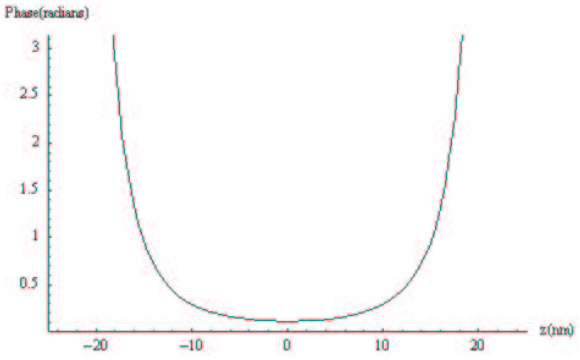

Figure C-3: Phase accumulated for atoms passing through a grating slit of width 50 nm. Classical trajectories are assumed, and the deflection of these paths is neglected. The interaction time is 0.1 ns.

$(z(0) = z_0,\ z(t_0) = 0)$ leads to:

$$t_0 = \sqrt{\frac{6m}{d^2}} \int_0^{z_0} \frac{dz}{\sqrt{z^{-3} - z_0^{-3}}} = \sqrt{\frac{6\pi m}{d^2}} \frac{\Gamma(\frac{5}{6})}{\Gamma(\frac{1}{3})} z_0^{5/2} \tag{C.11}$$

Once an atom enters the grating, it will collide with the walls if $t_0 < t_{\text{transit}} =$ 0.1 ns. The critical distance z_0 within which $t_0 < 0.1$ ns is 4.0 nm. All atoms within 4.0 nm of either wall will hit the wall before exiting the grating. Consequently, 16% of the atoms that enter the grating do not make it through. A grating constructed with a 50% open fraction (the ratio of the actual open area of the slits to the total area) will appear to have a 42% open fraction.

The next step in understanding the atom-grating interactions is to consider a slit in the grating as a waveguide with a plane wave incident upon it. The phase-front of the outgoing matter waves can then be determined. Evolution of this phase-front determines the far field diffraction pattern observable at the detector and the predictions could then be compared with experimental measurements.

To see how the wavefront evolves through the slit, consider the phase evolved along straight-line trajectories:

$$\phi(z) = t_{\text{transit}} V(z)/\hbar \tag{C.12}$$

This is the Eikonal approximation. The far field diffraction from the single slit as a function of angle θ is:

$$\psi(\theta) = \int_{-L/2}^{L/2} dz\ \exp[i2\pi\theta z/\lambda_{\text{dB}} + i\phi(z)] \tag{C.13}$$

In the absence of a potential inside the slit, $\psi(\theta)$ is the familiar single slit diffraction:

$$\psi(\theta)\Big|_{\phi=0} = L\text{sinc}(L\pi\theta/\lambda) \tag{C.14}$$

A diffraction grating is just a linear array of slits, so $\psi(\theta)$ describes the envelope of the diffraction pattern, which consists of delta function peaks spaced by units of the

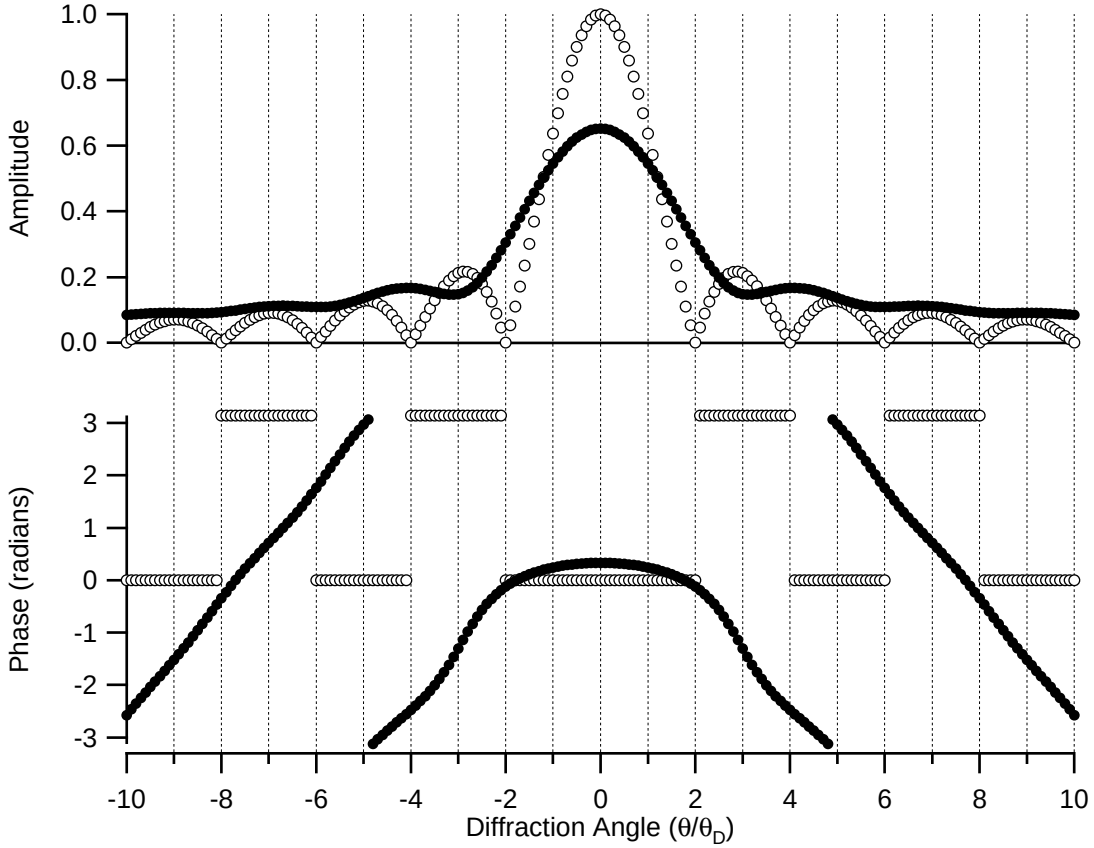

Figure C-4: Diffraction of sodium atoms from a 50 nm wide slit, in the presence of the Van der Waals potential (•) and without (○). The single slit diffraction is the envelope of the grating diffraction pattern, consisting of peaks spaced θ_D apart. A transit time in the slit of 10 ns and a grating period of 100 nm is assumed.

diffraction angle $\theta_D = \lambda_{dB}/(\text{grating period})$.

For simplicity, a simplified Van der Waals potential will be assumed:

$$V(z) = -\frac{2d^2}{3L^3}\left[(1-2z/L)^{-3} + (1+2z/L)^{-3}\right]. \tag{C.15}$$

Fig. C-4 depicts the resulting $\psi(\theta)$. The θ axis is in units of θ_D, the grating diffraction angle, assuming the grating has a 50% open fraction (the slit width is 50% of the period). For grating diffraction, the delta function peaks of the diffraction pattern will lie on the unit marks of the axis.

The single slit diffraction in the absence of a potential is shown for comparison.

The difference is quite noticeable—the diffraction pattern cannot be accurately predicted without considering Van der Waals forces. Both the amplitude and phase are dramatically affected. As discussed above, the most important effect produced is a that of a smaller open fraction. The smaller effective slit width attenuates the amplitude in the forward direction and spreads out the diffraction peaks. Not only are the diffraction peaks spaced farther apart, but they also are somewhat washed out and the zeros in the diffraction are notably missing. This would explain why we have never seen a grating that doesn't have a second order diffraction peak, even though a 50% open fraction has been the target in fabrication.

An experiment using diffraction gratings to measure Van der Waals forces has in fact been performed by Toennies *et al.* [44]. They have confirmed the diffraction features predicted here such as a smaller effective slit width, equal intensity among the higher diffractive orders, and the non-vanishing of even order diffractive peaks for a 50% open fraction grating.

C.3 Conclusion

It is unfortunate that a traditional interferometric measurement of Casimir-Polder interactions seems unfeasible. The possibility of observing the same interactions in the diffraction pattern of a grating remains an interesting possibility. The measurements of Van der Waals forces by Toennies *et al.* used helium [44, 45]. If sodium were used, however, the forces would be in the mid-distance regime where an accurate description of the Casimir-Polder interactions requires an understanding of the vacuum EM mode structure.

As a practical consideration, Casimir-Polder interactions may end up interfering with the desired operation of a diffraction grating. The transmission of atoms drops dramatically in going to smaller period grating, and this will ultimately limit how small the period of an atom grating can be made and sill be useful. But it is also conceivable that interactions in the grating could be tailored to produce practical applications. Asymmetries created in the slits during the production of the gratings

could be used to make blazed gratings for instance.

Appendix D

Transverse Laser Cooling for Improved Atomic Beam Flux

Because the two paths in our interferometer cannot be diffracted apart by a large amount, we must collimate the beam to a very small width, typically using 10 μm wide slits, in order to spatially resolve the beams. This greatly reduces the detected flux of the atomic beam. To recover the lost flux, laser cooling can be used to focus more atoms into the narrow forward direction.

With a single laser beam, aimed perpendicular to the atomic beam, each atom is deflected with a kick equal to $\Delta v = \hbar k/m = 2.89$ cm/s per photon. As photons are continually scattered, the acceleration of an atom is Δv times the scattering rate, equal to (natural linewidth)×(excited state population):

$$\dot{v} = \frac{\hbar k}{m}\,\Gamma\,\frac{S}{4D^2 + 2S + 1} \tag{D.1}$$

where $D \equiv \delta/\Gamma$ and $S \equiv \frac{\omega_R^2}{\Gamma^2}$ with linewidth Γ and detuning δ. The saturation parameter S is equal to one for a sodium-resonant laser intensity of 12.7 mW/cm^2. The maximum excited state population is $\frac{1}{2}$, so the maximum acceleration is $\frac{1}{2}\hbar k\Gamma/m = \frac{1}{2}(2.89\text{ cm/s})/16\text{ ns} = 9 \times 10^5$ m/s^2.

With two opposing laser beams, red detuned, the sodium beam is cooled. Atoms

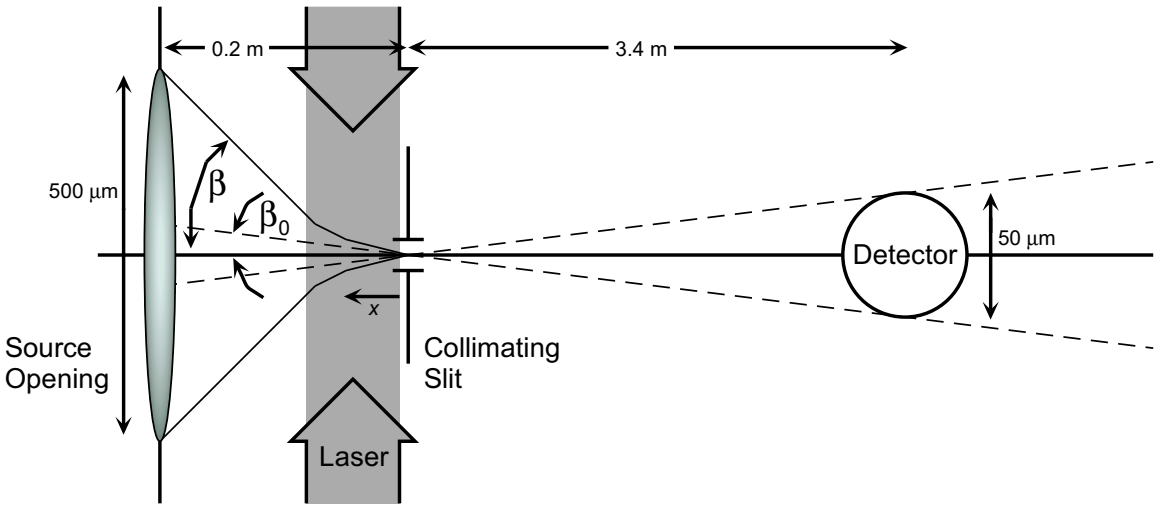

Figure D-1: A pair of laser beams forms a standing wave, which cools atoms within angle β down to the angle β_0, greatly increasing the flux of the atomic beam reaching the detector.

with non-zero transverse velocity see a Doppler-shifted laser, $\delta \to \delta \pm \vec{k} \cdot \vec{v}$.

$$\dot{v} = \frac{\hbar k \Gamma}{m} \left[\frac{S}{4(D - kv/\Gamma)^2 + 2S + 1} - \frac{S}{4(D + kv/\Gamma)^2 + 2S + 1} \right] \tag{D.2}$$

For $kv/\Gamma \ll 1$ (or $v \ll 5.89$ m/s) this approximates to

$$\dot{v} = -\alpha v \qquad \text{where} \qquad \alpha \equiv \frac{\hbar k^2}{m} \frac{-DS}{(D^2 + (2S+1)/4)^2}. \tag{D.3}$$

Define $\tau \equiv m/\hbar k^2 = 3.25$ μs, the time it takes to go λ with one recoil velocity. The maximum α is $\alpha = 1/2\tau$ for $D = -\frac{1}{2}$, $S = 1$. Under these conditions, the transverse velocity v drops by $\times 1/e$ in a time $2\tau = 6.5$ μs. For a 1000 m/s beam, this happens in a downstream distance $v_0 \tau = 6.5$ mm.

The geometry of the technique is depicted in Fig. D-1. We want to cool atoms into the angle β_0 subtended by the detector. Without laser cooling, the detector sees a width $2\beta_0 \times (20 \text{ cm}) \approx 3$ μm of the atoms in the source. With laser cooling, atoms with a larger angle β are cooled into angle β_0 and the counts go up by a factor

$\kappa \equiv \beta/\beta_0$. β is the transverse velocity v divided by the longitudinal velocity v_0.

$$\dot{v} = -\alpha v \quad \rightarrow \quad \frac{dt}{dx}\frac{\dot{v}}{v_0} = -\frac{\alpha}{v_0}\beta \quad \rightarrow \quad \frac{d\beta}{dx} = -\Big[\frac{-DS}{(D^2+(2S+1)/4)^2}\Big]\frac{\beta}{v_0\tau} \tag{D.4}$$

$$\beta = \beta_0 \exp\Big[\frac{x}{3.25\text{ mm}}\ \frac{-DS}{(D^2+(2S+1)/4)^2}\Big] \tag{D.5}$$

For optimum laser parameters $D = -\frac{1}{2}$, $S = 1$, the counts go up by a factor

$$\kappa = \beta/\beta_0 = \exp\Big[\frac{x}{6.5\text{ mm}}\Big] \tag{D.6}$$

$\kappa = 5$ for a 1 cm region. $\kappa = 22$ for a 2 cm region.

However, heating effects of the lasers have so far been neglected. The minimum laser cooled velocity is given by the condition $\frac{1}{2}mv^2_{\text{thermal}} = \frac{1}{12}\hbar\Gamma'(\frac{2|\delta|}{\Gamma'} + \frac{\Gamma'}{2|\delta|})$ with $\Gamma' \equiv \Gamma\sqrt{1+2S}$ or approximately $\frac{1}{2}mv^2_{\text{thermal}} \approx \frac{1}{6}\hbar\Gamma$. The minimum cooled velocity is then $v_{\text{thermal}} = \sqrt{\frac{\hbar\Gamma}{3m}} = 24$ cm/s corresponding to a minimum angle $\beta_{\text{thermal}} = 0.24$ mrad, equivalent to a displacement of 0.8 mm at the detector. This means atoms originally within angle β_0 will be heated out to more than 10× the angle!

But, we start with a distribution of transverse velocities much bigger than v_{thermal}, so heating won't loose any counts. Consider atoms with $v > v_{\text{thermal}}$ cooled into angle β_{thermal}. κ is the same as before, provided that the opening in the source is large enough to provide atoms with initial velocities $\kappa v_{\text{thermal}}$. The size of the opening sets a limit on κ. The best we can achieve for our source, with a 250 μm radius (the size of the skimmer), is $\kappa = v_{\max}/v_{\text{thermal}} = \frac{250\ \mu\text{m}}{20\text{ cm}}\ \frac{v_0}{v_{\text{thermal}}} = 5$. This would require a 1 cm wide laser region and a laser power of about 1.3 mW for a 1 mm tall beam.

Appendix E

Calculation of the Signal-to-Noise of an Interference Fringe Measurement

The number of atoms I measured by the detector within a given time interval is $\langle I \rangle \pm \Delta I$, where $\langle I \rangle = FT \equiv N$, where F is the beam flux (number of atoms per unit time) and T the length of the time interval. Detection of the atomic beam has normal Poisson counting statistics ($\Delta I = \sqrt{N}$), so N can be measured with a signal-to-noise ratio, S, of

$$S_N = \frac{\langle I \rangle}{\Delta I} = \sqrt{N}. \tag{E.1}$$

With the interferometer in place, the number of atoms detected depends on the phase of the interferometer (assuming the phase is fixed): [1]

$$\big\langle I(\phi) \big\rangle = N + A \cos \phi \tag{E.2}$$

To measure A, let's assume we spend half the time measuring the number of

[1]The question may arise as to how the background count rate affects measurement errors, but the background signal is either spiky in nature, in which case the extra counts can be removed from the measured $I(\phi_s)$ before doing the fit, or, the background is itself Poissonian just like the average count rate, in which case these counts can just be considered as part of N.

counts I_1 collected at a phase $\phi = \phi'$ and half the time measuring I_2 at $\phi = \phi' + \pi$. Then we expect averages and standard deviations of

$$\begin{aligned} \langle I_{1,2} \rangle =& \frac{N}{2} \pm \frac{A}{2} \cos \phi' \\ \Delta I_{1,2} =& \sqrt{\langle I_{1,2} \rangle} \end{aligned} \tag{E.3}$$

From this we can estimate either N or A with signal-to-noise

$$\begin{aligned} S_N =& \frac{\langle I_1 + I_2 \rangle}{\Delta (I_1 + I_2)} = \sqrt{N} \\ S_A(\phi') =& \frac{\langle I_1 - I_2 \rangle}{\Delta (I_1 - I_2)} = \frac{A \cos \phi'}{\sqrt{N}} \end{aligned} \tag{E.4}$$

where we have taken care to add the deviations in quadrature: $\Delta(I_1 \pm I_2) = \sqrt{\Delta I_1^2 + \Delta I_2^2}$.

Normally, we measure the interference pattern at all phases. To find the standard deviation of the *average* of many measurements A_i taken at different phases ϕ_i', we would use:

$$\frac{\Delta A}{A} = \left[\sum \left(\frac{\Delta A_i}{A_i} \right)^{-2} \right]^{-1/2}. \tag{E.5}$$

Therefore, for an interference pattern averaged over all ϕ' we have

$$S_A = \sqrt{\frac{1}{2\pi} \int_0^{2\pi} d\phi' \, {S_\mathrm{A}}^2(\phi')} = \frac{A}{\sqrt{2N}}. \tag{E.6}$$

If we want to measure the contrast, $C = A/N$, the statistical error is a little more complex. Keep in mind that although we generally report the amplitude of the interference pattern in terms of C rather than A, in an experiment we almost always want to compare amplitudes, not contrasts, so Eq. E.6 is the more important one. The relative deviation in C is

$$\frac{\Delta C}{C} = \sqrt{\left(\frac{\Delta A}{A} \right)^2 + \left(\frac{\Delta N}{N} \right)^2} = \frac{1}{\sqrt{N}} \sqrt{\frac{1}{C^2 \cos^2 \phi'} + 1} = \frac{1}{S_C(\phi')}. \tag{E.7}$$

We can add the deviations of A and N in quadrature because they are linearly independent measurements, even though they depend on the same parameters I_1 and I_2.

Averaged over all ϕ' we have

$$S_C = \sqrt{N}\sqrt{1 - \frac{1}{\sqrt{1+C^2}}} \tag{E.8}$$

or in the limit of small C:

$$S_C \approx C\sqrt{N/2} \tag{E.9}$$

Now consider the signal-to-noise in measuring the phase in Eq. E.2. ϕ actually consists of two phases, $\phi = \phi_s + \phi_0$. The phase ϕ_s is scanned during the measurement, and the detected function $I(\phi_s)$ is fit to determine ϕ_0. Sitting at a fixed phase, the precision in ϕ_0 is determined by the slope of the signal with respect to the phase:

$$\Delta\phi_0 = \Delta I(\phi)\Big[\frac{dI(\phi)}{d\phi}\Big]^{-1} = \frac{\sqrt{N + A\cos\phi}}{-A\sin\phi} \equiv \frac{1}{S_{\phi_0}(\phi)} \tag{E.10}$$

Note that the signal-to-noise ratio needs to be defined differently for phase. Averaged over all ϕ, the signal-to-noise is:

$$S_{\phi_0} = \sqrt{N - \sqrt{N^2 - A^2}} = \sqrt{N}\sqrt{1 - \sqrt{1 - C^2}} \tag{E.11}$$

In the limit of small C it is

$$S_{\phi_0} \approx C\sqrt{N/2}, \tag{E.12}$$

exactly the same as for S_C.

For a typical measurement, we have a beam flux of 10 kHz and a contrast of 10%. In a 1 sec interval, the signal-to-noise ratio is $S \approx C\sqrt{N/2} = 7.1$. The phase will be measured to 140 mrad and the contrast will be measured to within 14% of its actual value. In one minute, this improves to 18 mrad and 1.8% respectively.

Bibliography

[1] Potential proposed by D. Zimmermann *et al.* in Ref. [17].

[2] G. Aepfelbach, A. Nunnemann, and D. Zimmermann. Laser spectroscopic investigation of the X2-Sigma1-2 state of the Van der Waals molecule NaAr. *Chem. Phys. Lett.*, 96(3):311, 1983.

[3] R. Ahmadbitar, W. P. Lapatovich, D. E. Pritchard, and I. Renhorn. Laser spectroscopy of bound NaNe molecules. *Phys. Rev. Lett.*, 39(26):1657, 1977.

[4] J. R. Anglin, J. P. Paz, and W. H. Zurek. Deconstructing decoherence. *Phys. Rev. A*, 55(6):4041, 1997.

[5] J. F. Babb, 2001. Personal communication.

[6] P. Baumann, D. Zimmermann, and R. Bruhl. Laser spectroscopic investigation of the Van der Waals molecule NaXe. *J. Mol. Spectrosc.*, 155(2):277, 1992.

[7] W. E. Baylis. Semiemperical pseudopotential calculation of alkalai-noble-gas interaction potentials. *J. Chem. Phys.*, 51(6):2665, 1969.

[8] P. R. Berman ed. *Atom Interferometry.* Academic Press, 1997.

[9] C. Bottcher and A. Dalgarno. Constructive model potential method for atomic interactions. *Proc. R. Soc. London Ser. A-Math. Phys. Eng. Sci.*, 340(1621):187, 1974.

[10] R. Bruhl, J. Kapetanakis, and D. Zimmermann. Determination of the Na-Kr interaction potential in the X-Sigma and A-Pi state by laser spectroscopy. *J. Chem. Phys.*, 94(9):5865, 1991.

[11] H. C. Bryant and A. J. Cox. Mie theory and the glory. *Journal of the Optical Society of America*, 56(11), 1966.

[12] H. C. Bryant and N. Jarmie. The glory. *Sci.Am.*, 231(1):60, 1974.

[13] U. Buck and H. Pauly. Interferences in atomic collision processes and their interpretation using a modified Lennard-Jones-potential. *Z. Phys.*, 208:390, 1968.

[14] G. M. Carter, D. E. Pritchard, M. Kaplan, and T. W. Ducas. Differential scattering of Na 3S1-2 and 3P3-2 from Ne: Determination of ground-state and excited-state potentials for NaNe. *Phys. Rev. Lett.*, 35(17):1144, 1975.

[15] H. G. B. Casimir and D. Polder. Phys. Rev. 73, 360 (1947).

[16] K. Chadan and P. C. Sabatier. *Inverse Problems in Quantum Scattering Theory.* Springer, New York, 1989.

[17] C. Champenois, E. Audouard, P. Duplaa, and J. Vigue. Refractive index for atomic waves: Theory and detailed calculations. *J. Phys. II*, 7(4):523, 1997.

[18] M. S. Chapman. *Photon Induced Coherence Loss in Atom Interferometry.* PhD Thesis, MIT, 1995.

[19] M. S. Chapman, T. D. Hammond, A. Lenef, J. Schmiedmayer, R. A. Rubenstein, E. Smith, and D. E. Pritchard. Photon scattering from atoms in an atom interferometer: Coherence lost and regained. *Phys. Rev. Lett.*, 75(21):3783, 1995.

[20] C. C. Cheng and M. G. Raymer. Long-range saturation of spatial decoherence in wave-field transport in random multiple-scattering media. *Phys. Rev. Lett.*, 82(24):4807, 1999.

[21] R. A. Cheville, R. W. McGowan, and D. Grischkowsky. Time resolved measurements which isolate the mechanisms responsible for terahertz glory scattering from dielectric spheres. *Phys. Rev. Lett.*, 80(2):269, 1998.

[22] D. C. Cole and H. E. Putoff. Phys. Rev. E 48, 1562 (1993).

[23] R. Colella, A. W. Overhauser, and S. A. Werner. Observation of gravitationally induced quantum interference. *Phys. Rev. Lett.*, 34(23):1472, 1975.

[24] E. Czuchaj and J. Sienkiewicz. Adiabatic potentials of the alkali rare gas atom pairs. *Z. Naturfors. Sect. A-J. Phys. Sci.*, 34(6):694, 1979.

[25] T. Delbar, G. Gregoire, G. Paic, R. Ceuleneer, F. Michel, R. Vanderpoorten, A. Budzanowski, H. Dabrowski, L. Freindl, K. Grotowski, S. Micek, R. Planeta, A. Strzalkowski, and K. A. Eberhard. Elastic and inelastic-scattering of alpha-particles from Ca-40, Ca-44 over a broad range of energies and angles. *Phys. Rev. C*, 18(3):1237, 1978.

[26] A. C. Donea, C. Lindsey, and D. C. Braun. Stochastic seismic emission from acoustic glories and the quiet sun. *Sol. Phys.*, 192(1-2):321, 2000.

[27] R. Duren, A. Frick, and C. Schlier. Glory undulations of some alkali-molecule systems. *Journal of Physics B*, 5:1744, 1972.

[28] R. Duren and W. Groger. Determination of Na-Ar ground-state potential from differential cross-section measurements. *Chem. Phys. Lett.*, 56(1):67, 1978.

[29] R. Duren, W. Groger, E. Hasselbrink, and R. Liedtke. Differential scattering cross-sections and the a 2-Pi potentials for the systems NaAr, NaKr, and NaXe. *J. Chem. Phys.*, 74(12):6806, 1981.

[30] R. Duren and G. Moritz. Improved model calculations for the alkali rare gas interaction. *J. Chem. Phys.*, 73(10):5155, 1980.

[31] R. Duren, G. P. Raabe, and C. Schlier. Accurate fitting of interatomic potential from scattering: Alkali-rare gas systems. *Z. Phys.*, 214:410, 1968.

[32] R. Duren and C. Schlier. Accurate fitting of realistic interatomic potentials. *J. Chem. Phys.*, 46:4535, 1967.

[33] C. R. Ekstrom. *Experiments with a Separated Beam Atom Interferometer*. PhD Thesis, MIT, 1993.

[34] C. R. Ekstrom, J. Schmiedmayer, M. S. Chapman, T. D. Hammond, and D. E. Pritchard. Measurement of the electric polarizability of sodium with an atom interferometer. *Phys. Rev. A*, 51(5):3883, 1995.

[35] V. R. Eshleman. Mode decoupling during retrorefraction as an explanation for bizarre radar echoes from icy moons. *Nature*, 319(6056):755, 1986.

[36] R. C. Forrey, 2001. Personal communication.

[37] R. C. Forrey, L. You, V. Kharchenko, and A. Dalgarno. Index of refraction of noble gases for sodium matter waves. *Phys. Rev. A*, 54(3):2180, 1996.

[38] R. C. Forrey, L. You, V. Kharchenko, and A. Dalgarno. Refining molecular potentials using atom interferometry. *Phys. Rev. A*, 55(5):R3311, 1997.

[39] M. R. Gallis and G. N. Fleming. Environmental and spontaneous localization. *Phys. Rev. A*, 42(1):38, 1990.

[40] K. Glampedakis and N. Andersson. Scattering of scalar waves by rotating black holes. *Class. Quantum Gravity*, 18(10):1939, 2001.

[41] J. H. Goble and J. S. Winn. Analytic potential functions for weakly bound molecules: X-state and A-state of NaAr and the A-state of NaNe. *J. Chem. Phys.*, 70(5):2051, 1979.

[42] R. Goldstein, J. Grosser, O. Hoffmann, V. Schumann, D. Wossner, M. Jungen, and M. Lehner. Electronic structure of the NaN2 and NaC2H2 collision complexes: Experiment and theory. *J. Chem. Phys.*, 114(5):2144, 2001.

[43] R. A. Gottscho, R. Ahmadbitar, W. P. Lapatovich, I. Renhorn, and D. E. Pritchard. Global analysis of the NaNe excimer band systems: A molecule between Hunds cases. *J. Chem. Phys.*, 75(6):2546, 1981.

[44] R. E. Grisenti, W. Schollkopf, J. P. Toennies, C. C. Hegerfeldt, and T. Kohler. Determination of atom-surface Van der Waals potentials from transmission-grating diffraction intensities. *Phys. Rev. Lett.*, 83(9):1755, 1999.

[45] R. E. Grisenti, W. Schollkopf, J. P. Toennies, J. R. Manson, T. A. Savas, and H. I. Smith. He-atom diffraction from nanostructure transmission gratings: The role of imperfections. *Phys. Rev. A*, 6103(3):3608, 2000.

[46] P. Habitz. Potential curves for the ground and excited-states of the NaN2 system. *Chem. Phys.*, 54(1):131, 1980.

[47] T. D. Hammond. *Atom Interferometry: Dispersive Index of Refraction and Rotation Induced Phase Shifts for Matter-Waves.* PhD Thesis, MIT, 1997.

[48] T. D. Hammond, D. E. Pritchard, M. S. Chapman, A. Lenef, and J. Schmiedmayer. Multiplex velocity selection for precision matter-wave interferometry. *Appl. Phys. B-Lasers Opt.*, 60(2-3):193, 1995.

[49] E. A. Hinds. *et al.*, in Atomic Physics, edited by J. Zorn and R. Lewis (AIP, New York, 1991), Vol. 12, p. 283.

[50] M. J. Jongerius. Collisional broadening of the Na-D lines by xenon in high-pressure sodium arcs. *J. Phys. B-At. Mol. Opt. Phys.*, 20(14):3345, 1987.

[51] M. J. Jongerius, T. Hollander, and C. T. J. Alkemade. An experimental study of the collisional broadening of the Na-D lines by Ar and N2 perturbers in flames and vapor cells. *J. Quant. Spectrosc. Radiat. Transf.*, 26(4):285, 1981.

[52] W. Kamke, B. Kamke, I. Hertel, and A. Gallagher. Fluorescence of the Na*-N2 collision complex. *J. Chem. Phys.*, 80(10):4879, 1984.

[53] D. W. Keith. *An Interferometer for Atoms.* PhD Thesis, MIT, 1991.

[54] D. W. Keith, C. R. Ekstrom, Q. A. Turchette, and D. E. Pritchard. An interferometer for atoms. *Phys. Rev. Lett.*, 66(21):2693, 1991.

[55] V. Khare and H. M. Nussenzveig. Theory of glory. *Phys. Rev. Lett.*, 38(22):1279, 1977.

[56] D. A. Kokorowski. *Measuring Decoherence and the Matter-Wave Index of Refraction with an Improved Atom Interferometer*. PhD Thesis, MIT, 2001.

[57] D. A. Kokorowski, A. D. Cronin, T. D. Roberts, and D. E. Pritchard. From single- to multiple-photon decoherence in an atom interferometer. *Phys. Rev. Lett.*, 86(11):2191, 2001.

[58] L. D. Landau. *Quantum Mechanics*. Pergamon, 1977.

[59] W. P. Lapatovich, R. Ahmadbitar, P. E. Moskowitz, I. Renhorn, R. A. Gottscho, and D. E. Pritchard. Laser spectroscopy of the diatomic Van der Waals molecule NaNe. *J. Chem. Phys.*, 73(11):5419, 1980.

[60] B. C. Laskowski, S. R. Langhoff, and J. R. Stallcop. Theoretical calculation of low-lying states of NaAr and NaXe. *J. Chem. Phys.*, 75(2):815, 1981.

[61] M. Lax. Multiple scattering of waves. *Reviews of Modern Physics*, 23(4):287, 1951.

[62] F. London. Trans. Faraday Soc. 33, 8 (1937).

[63] Nanotechnology Magazine. www.nanozine.com/q-2.htm.

[64] P. L. Marston. Optics: A time-resolved glimpse of the terahertz glory. *Nature*, 391(6670):841, 1998.

[65] E. A. Mason, R. M. Hermans, and C. J. N. Vandenmeijdenberg. On the direct inversion of total scattering cross-sections beyond the glory region. *Physica A*, 117(1):160, 1983.

[66] E. A. Mason and C. J. N. Vandenmeijdenberg. On the direct inversion of total scattering cross-sections in the glory region. *Physica A*, 117(1):139, 1983.

[67] R. A. Matzner, C. Dewittemorette, B. Nelson, and T. R. Zhang. Glory scattering by black-holes. *Phys. Rev. D*, 31(8):1869, 1985.

[68] W. Muller and W. Meyer. Static dipole polarizabilities of Li-2, Na-2, and K-2. *J. Chem. Phys.*, 85(2):953, 1986.

[69] A. P. Nefedov, V. A. Sinel'shchikov, and A. D. Usachev. Collisional broadening of the Na-D lines by molecular gases. *Phys. Scr.*, 59(6):432, 1999.

[70] A. P. Nefedov, V. A. Sinel'shchikov, and A. D. Usachev. Reduced absorption coefficient in wings of the Na-D doublet broadened by O-2, N-2, CO2 and H2O molecules. *J. Quant. Spectrosc. Radiat. Transf.*, 61(1):73, 1999.

[71] R. G. Newton. *Scattering Theory of Waves and Particles*. McGraw-Hill, 1966.

[72] H. M. Nussenzveig. Complex angular-momentum theory of the rainbow and the glory. *Journal of the Optical Society of America*, 69(8):1068, 1979.

[73] H. M. Nussenzveig and W. J. Wiscombe. Forward optical glory. *Opt. Lett.*, 5(10):455, 1980.

[74] A. N. Ostrowski, A. C. Shotter, W. Galster, S. Cherubini, T. Davinson, A. M. Laird, and A. Ninane. Nuclear forward glory: Sigma(R) and f(N) (0 degrees) in the scattering of He-6 by carbon. *Phys. Rev. C*, 6006(6):4603, 1999.

[75] A. N. Ostrowski, W. Tiereth, and H. Voit. Forward nuclear glory in C-12+C-12 scattering. *Phys. Rev. C*, 44(5):2082, 1991.

[76] J. Pascale and Vandepla.J. Excited molecular terms of alkali-rare-gas atom pairs. *J. Chem. Phys.*, 60(6):2278, 1974.

[77] M. Philippe, F. Masnouseeuws, and P. Valiron. Model-potential method for the calculation of atom-rare-gas interactions: Application to the Na-Ne system. *J. Phys. B-At. Mol. Opt. Phys.*, 12(15):2493, 1979.

[78] W. D. Phillips, J. A. Serri, D. J. Ely, D. E. Pritchard, K. R. Way, and J. L. Kinsey. Angular scattering distribution by doppler spectroscopy: Na(3p1-2)+Ar → Na(3p3-2)+Ar. *Phys. Rev. Lett.*, 41(14):937, 1978.

[79] E. W. Rothe, P. K. Rol, S. M. Trujillo, and R. H. Neynaber. Velocity dependence of the total cross section for the scattering of Li and K by Xe. *Physical Review*, 128(2):659, 1962.

[80] R. A. Rubenstein. *Longitudinal Atom Optics: Measuring the Density Matrix of a Matter Wave Beam.* PhD Thesis, MIT, 1999.

[81] V. Sandoghar. *et al.*, Phys. Rev. Lett. 68, 3432 (1992).

[82] R. P. Saxon, R. E. Olson, and B. Liu. Ab initio calculations for X2-Sigma, A2-Pi, and B2-Sigma states of NaAr: Emission-spectra and cross-sections for fine-structure transitions in NaAr collisions. *J. Chem. Phys.*, 67(6):2692, 1977.

[83] J. Schmiedmayer, M. S. Chapman, C. R. Ekstrom, T. D. Hammond, S. Wehinger, and D. E. Pritchard. Index of refraction of various gases for sodium matter waves. *Phys. Rev. Lett.*, 74(7):1043, 1995.

[84] J. Schmiedmayer, C. R. Ekstrom, M. S. Chapman, T. D. Hammond, and D. E. Pritchard. Magnetic coherences in atom interferometry. *J. Phys. II*, 4(11):2029, 1994.

[85] V. F. Sears. Fundamental aspects of neutron optics. *Phys. Rep.-Rev. Sec. Phys. Lett.*, 82(1):1, 1982.

[86] R. Shuker, A. Gallagher, and A. V. Phelps. Models of high-power discharges for metal-Xe excimer lasers. *J. Appl. Phys.*, 51(3):1306, 1980.

[87] R. E. Smalley, D. A. Auerbach, P. S. H. Fitch, D. H. Levy, and L. Wharton. Laser spectroscopic measurement of weakly attractive interatomic potentials: Na+Ar interaction. *J. Chem. Phys.*, 66(8):3778, 1977.

[88] E. T. Smith. *Velocity Rephased Coherences in a Longitudinal Atom Interferometer*. PhD Thesis, Harvard, 1998.

[89] J. M. Standard and P. R. Certain. Bounds to 2-body and 3-body long-range interaction coefficients for S-state atoms. *J. Chem. Phys.*, 83(6):3002, 1985.

[90] G. D. Stevens, C. H. Iu, T. Bergeman, H. J. Metcalf, I. Seipp, K. T. Taylor, and D. Delande. Absolute calibration of electric-fields using Stark spectroscopy. *Phys. Rev. Lett.*, 75(19):3402, 1995.

[91] G. D. Stevens, C. H. Iu, T. Bergeman, H. J. Metcalf, I. Seipp, K. T. Taylor, and D. Delande. Precision measurements on lithium atoms in an electric field compared with R-matrix and other Stark theories. *Phys. Rev. A*, 53(3):1349, 1996.

[92] N. Sugimoto. Feasibility of a lidar utilizing the glory for measuring particle size of water clouds. *Opt. Rev.*, 6(6):539, 1999.

[93] N. Sugimoto. Two-color dual-polarization pulsed bistatic lidar for measuring water cloud droplet size. *Opt. Rev.*, 7(3):235, 2000.

[94] C. I. Sukenik. *et al.*, Phys. Rev. Lett. 70, 560 (1993).

[95] J. Summhammer, H. Rauch, and D. Tuppinger. Stochastic and deterministic absorption in neutron-interference experiments. *Phys. Rev. A*, 36(9):4447, 1987.

[96] J. Summhammer, H. Rauch, and D. Tuppinger. Stochastic and deterministic attenuation of one beam in the neutron interferometer. *Physica B and C*, 151(1-2):103, 1988.

[97] N. Takigawa and S. Y. Lee. Nuclear glory effect and alpha-Ca-40 scattering. *Nucl. Phys. A*, 292(1-2):173, 1977.

[98] K. T. Tang and J. P. Toennies. Simple theoretical model for Van der Waals potential at intermediate distances. *J. Chem. Phys.*, 66(4):1496, 1977.

[99] K. T. Tang and J. P. Toennies. An improved simple model for the Van der Waals potential based on universal damping functions for the dispersion coefficients. *J. Chem. Phys.*, 80(8):3726, 1984.

[100] J. Tellinghuisen, A. Ragone, M. S. Kim, D. J. Auerbach, R. E. Smalley, L. Wharton, and D. H. Levy. Dispersed fluorescence spectrum of NaAr: Ground and excited state potential curves. *J. Chem. Phys.*, 71(3):1283, 1979.

[101] Q. A. Turchette. *Numerical Model of a Three Grating Interferometer for Atoms*. BS Thesis, MIT, 1991.

[102] M. Ueda, M. P. Pato, M. S. Hussein, and N. Takigawa. Glory "in the shadow of the rainbow". *Nucl. Phys. A*, 648(3-4):229, 1999.

[103] F. von Busch, H. J. Strunck, and C. Schlier. Die geschwindigkeitsabhangigkeit totaler streuquerschnitte von alkalien an edelgasen. *Zeitschrift fur Physik*, 199:518, 1967.

[104] J. P. Woerdman and J. J. Degroot. Identification of NaAr and NaXe satellite bands: A test for calculations of the B2Sigma-+ potential. *J. Chem. Phys.*, 76(11):5653, 1982.

[105] D. H. Yang, D. Lieberman, P. Vanderstraten, T. Bergeman, and H. Metcalf. Precision mapping of electrostatic fields using interference-narrowed Stark resonances. *Phys. Rev. A*, 40(9):5026, 1989.

[106] G. York, R. Scheps, and A. Gallagher. Continuum radiation and potentials of Na noble gas molecules. *J. Chem. Phys.*, 63(3):1052, 1975.

[107] E. Zanger, V. Schmatloch, and D. Zimmermann. Laser spectroscopic investigation of the Van der Waals molecule NaKr84. *J. Chem. Phys.*, 88(9):5396, 1988.

[108] D. Zimmermann. High resolution spectroscopy of the Van der Waals molecules NaAr and NaKr. *Acta Physica Hungarica*, 67(3-4):351, 1990.

Acknowledgments

I would like to express my deepest thanks to my wife Karen for her wonderful encouragement and support while pursuing my degree. She has shared in the hard parts but not the pleasures of working at MIT, as our time together was replaced by late hours studying and many all-nighters in the lab. I especially appreciate the many pursuits of her own that she has given up to allow me the opportunity to do research in physics these many years. I also enjoy her continued curiosity in my work, and her desire and patience to learn about quantum mechanics and the details of my experiment. She will be glad that I have now finished my degree, though I think she will miss all the colorful plots and graphs that she found so pretty.

My parents Dave and Joyce have been a great source of encouragement and inspiration for me, as they have been all my life. They have always been willing to make the biggest sacrifices just to save me a little trouble, and then tell me it was no bother at all. They have urged me on in all my endeavors, yet have never pushed too hard. My brothers, Joe, Andy, Tom, and David, have been a huge inspiration to me, too. I learn more from them than they might ever realize. Karen's family, Bob, Marylis, and Jennifer, have been an example to me too, and I admire them. I just hope they are not too disappointed that I did not discover how to "shrink the atom" during my research at MIT.

In the laboratory, I have been truly fortunate to have worked with the people I did. Dave Pritchard, especially, has the best qualities one could ask for in an advisor. He is a pleasure to work with, he has taught me physics with a great insight that cannot be found in any textbook, and he has helped me bring out some of the best work I am capable of. My fellow coworkers in the lab have been fun to work with as well. David Kokorowski has been a true friend, and I have missed his good nature as well as his scientific expertise ever since he left the lab. Alex Cronin has been a never-ending source of energy and ideas for the experiment. His enthusiasm has been quite contagious, and I hope to carry some of his inquisitive spirit with me when I leave. Working with Ed Smith and Rich Rubenstein has been a privilege, and from

them I learned about the resourcefulness and patience it takes to be a good scientist. I am also grateful to Al-Amin Dhirani who was like a mentor to me, teaching me about the academic world of atomic physics during my first years at MIT. It was great to work with Deep Gupta and Jana Lehner, and I wish their time in our lab had not been so short. I was also fortunate to work with some very talented undergraduates: Celeste Yang, Jay Mitchell, Peter Finin, and Martin Tiberg. I hope they learned as much from me as I did from them.

I will never forget the great community of people that I have been a part of in atomic physics at MIT. Being able to share in the excitement of the achievements in the Ketterle, Kleppner, and Pritchard labs has felt like being a part of history. I've been glad to have taken classes and had discussions with Wolfgang Ketterle and Dan Kleppner. It's been a great pleasure to have had Carol Costa's assistance in the department. I will miss the camaraderie and intellectual discussions with everyone in the atomic physics department, not to mention the softball and soccer games. Two people in particular I must mention are Stephen Moss and Simon Rainville. It has been great to have such good friends to help tackle the challenges of grad school, from class assignments to oral exams to trouble in the laboratory.

Finally, I must thank John Carlsten and John Stover, who helped me gain the invaluable experience in physics that was a factor in coming to MIT. They helped provide me with both the excitement and the confidence to pursue a physics degree.